# Study and spectroscopic monitoring of molten pool emission during laser-metal additive manufacturing

Dissertation

Zur Erlangung des akademischen Grades

Doktoringenieur

(Dr. – Ing.)

von M.Sc. Giuseppe Pignatelli
geb. am 06.04.1987 in Monopoli, Italien
genehmigt durch die Fakultät Maschinenbau der Otto-von-Guericke-Universität Magdeburg

Gutachter/innen:

| | |
|---|---|
| Vorsitzender: | Prof. Dr.-Ing. habil. Matthias Hackert-Oschätzchen |
| Gutachter: | Prof. Dr.-Ing. habil. Thomas Kannengießer |
| | Prof. Dr.-Ing. Jonas Hensel (TU Chemnitz) |

Promotionskolloquiums am 01.06.2026

# Table of content

ABSTRACT IV

ZUSAMMENFASSUNG VI

INTRODUCTION IX

1 LASER-MATTER INTERACTION 1

1.1 SOLID STATE LASERS 1

1.2 CHARACTERISTICS OF THE LASER BEAM 5

1.3 LASER-METAL INTERACTION: ABSORPTION AND REFLECTION 9

2 LASER-METAL ADDITIVE MANUFACTURING 14

2.1 DEFINITION AND SCOPE 15

2.2 ADDITIVE MANUFACTURING MECHANISM 16

2.2.1 PRINTING PARAMETERS 18

2.2.2 METAL PROPERTIES 21

2.3 DEFECT FORMATION 22

2.3.1 MICROSTRUCTURE DEFECTS 24

2.3.1.1 Porosity 26

2.3.1.2 Anisotropy and crystalline structure 28

2.3.2 INCLUSIONS 29

2.3.3 Dimensional anomalies 29

2.4 Online optical monitoring 30

2.4.1 Types of detectors 31

2.4.1.1 Point detectors 31

2.4.1.2 Cameras 32

2.4.1.3 Spectrally resolved detectors 35

2.5 Monitoring with external sources of light 38

2.6 Simulation 40

3 DED SPECTROSCOPY 42

3.1 Printing, monitoring set-up and acquisition 42

3.2 Molten pool emission 47

3.2.1 Plasma and continuous emission 47

3.2.2 Set-up characterization 48

3.2.3 Temperature calculation 51

3.3 Process characterization 57

4 FAULT MONITORING 61

4.1 Metrics 62

4.2 Modified steel plate 65

4.1.1 Results and discussion 67

4.1.2 POST-BUILDING ANALYSIS 72

4.2 THERMAL DIFFUSION SIMULATION 74

4.2.1 THEORETICAL BACKGROUND 74

4.2.2 SURFACE SIMULATION 77

4.2.3 LIGHT COLLECTION GEOMETRY 78

4.2.4 BOUNDARY CONDITIONS 80

4.2.5 EXPERIMENTAL 81

4.2.6 RESULTS AND DISCUSSION 82

4.2.6.1 Simulation 82

4.2.6.1 Experiment 92

5 CONCLUSIONS 95

6 STATEMENT OF INDEPENDENT WORK 97

7 SCIENTIFIC OUTPUT 97

8 ABBREVIATIONS 98

9 LIST OF FIGURES 100

10 LIST OF TABLES 102

11 ACKNOWLEDGMENT 103

12 REFERENCES 104

## Abstract

Additive Manufacturing (AM) has transformed production by enabling the creation of new items starting from a software blueprint, greatly simplifying prototyping. Among the various AM techniques, Direct Energy Deposition (DED) prints metal parts from powder using a focused laser, allowing the fabrication of pieces with geometries otherwise unattainable. However, commercially ready printed components must meet the same quality and reliability standards as those made with traditional methods, which is not yet guaranteed and limits wider AM adoption. In DED, a high-power laser interacts with a base plate to form a molten pool, where a constant powder flow is then directed. This complex interaction can generate surface and bulk defects in the printed items, such as pores and inclusions.

Improving DED reliability requires a deeper understanding of molten pool dynamics and effective online monitoring to optimize process parameters and detect defects as they form. This work presents an optical setup based on compact UV-Vis and NIR spectrometers mounted on the laser head and capable of recording molten pool emission during deposition. The spectra show no plasma features, indicating purely thermal emission, from which the molten pool temperature is computed. Additional metrics, like integrated emitted intensity and a correlation coefficient linking online signals to a reference library, are also calculated from the emission spectra. The molten pool is then studied under different processing conditions, both individually and grouped through combined parameters such as laser energy density, looking for a link between emission and deposition settings.

Defect studies in AM are hindered by the lack of standardization. To address this, a modified steel plate with machined grooves and holes of known size and position is used as a printing substrate, providing a standardised source of defects. The recorded optical emission demonstrates that the setup can detect void-like defects down to 1 mm in diameter and track their evolution within the printed material.

Finally, a simplified thermal model simulates a laser scanning a metal substrate with an uneven surface. Various defect types and a thermally emitting molten pool are included, along with a realistic light-collection geometry. The simulated emission is processed using the same metrics applied experimentally, and the two sets of results show good agreement for comparable artificial defects. This confirms that simplified numerical simulations can complement, and partly replace, experimental studies in analysing metal AM processes.

# Zusammenfassung

Die additive Fertigung (AM) hat die Produktion revolutioniert, indem sie die Herstellung neuer Produkte auf Basis eines Software-Entwurfs ermöglicht und damit die Prototypenentwicklung erheblich vereinfacht. Direct Energy Deposition (DED) ist eine der AM-Techniken, bei der, unter Verwendung eines fokussierten Lasers, Metallteile aus Pulver gedruckt werden. Dies ermöglicht die Herstellung von Komponenten mit ansonsten unerreichbaren Geometrien.

Kommerziell einsetzbare gedruckte Komponenten müssen jedoch dieselben Qualitäts- und Zuverlässigkeitsstandards erfüllen wie solche, die mit traditionellen Methoden hergestellt wurden, was noch nicht garantiert ist und eine breitere Einführung von AM einschränkt. Bei der DED-Methode interagiert ein Hochleistungslaser mit einer Grundplatte, um ein Schmelzbad zu bilden, in welches ein konstanter Pulverfluss geleitet wird. Diese komplexe Interaktion kann zu Oberflächen- und Volumenfehlern in den gedruckten Gegenständen führen, wie z. B. Poren und Einschlüssen.

Um die Zuverlässigkeit der DED zu verbessern, ist ein tieferes Verständnis der Dynamik des Schmelzbads und eine effektive Online-Überwachung erforderlich, um die Prozessparameter zu optimieren und Fehler zu erkennen, sobald sie entstehen.

Diese Arbeit stellt ein optisches Setup vor, welches auf kompakten UV-Vis- und NIR-Spektrometern basiert, die auf dem Laserkopf montiert sind und die Emission des Schmelzbades während der Abscheidung aufzeichnen können. Die Spektren zeigen keine Plasmaeigenschaften, was auf eine rein thermische Emission hindeutet, aus der die Temperatur des Schmelzbades berechnet wird. Zusätzliche Messgrößen, wie die integrierte Emissionsintensität und ein

Korrelationskoeffizient, der Online-Signale mit einer Referenzbibliothek verknüpft, werden ebenfalls aus den Emissionsspektren berechnet. Das Schmelzbad wird dann unter verschiedenen Prozessbedingungen untersucht, sowohl einzeln als auch gruppiert durch kombinierte Parameter wie die Laserenergiedichte, um einen Zusammenhang zwischen Emission und Abscheidungseinstellungen zu finden.

Durch die mangelnde Standardisierung in der additiven Fertigung wurden bisher kaum Studien zu prozessualen Defekten durchgeführt. Um diesem Problem zu begegnen, wird eine modifizierte Stahlplatte mit maschinell gefertigten Rillen und Löchern bekannter Größe und Position als Drucksubstrat verwendet, das eine standardisierte Quelle für Defekte darstellt. Die aufgezeichnete optische Emission zeigt, dass durch den experimentellen Aufbau hohlraumartige Defekte mit einem Durchmesser von bis zu 1 mm erkennen und deren Entwicklung innerhalb des gedruckten Materials verfolgen kann.

Schließlich simuliert ein vereinfachtes thermisches Modell einen Laser, der ein Metallsubstrat mit unebener Oberfläche abtastet. Dabei werden verschiedene Fehlertypen und ein thermisch emittierendes Schmelzbad sowie eine realistische Lichtabfanggeometrie berücksichtigt. Die simulierte Emission wird unter Verwendung derselben Metriken verarbeitet, die auch experimentell angewendet wurden. Beide Ergebnissätze zeigen eine gute Übereinstimmung für vergleichbare künstliche Fehler. Dies bestätigt, dass vereinfachte numerische Simulationen experimentelle Studien bei der Analyse von Metall-AM-Prozessen ergänzen und teilweise ersetzen können.

# Introduction

Additive Manufacturing (AM) is a production technique applicable to a wide set of materials, like polymers, ceramics, and metals. It was first introduced in 1984 with a stereolithography device forming plastic components [4]. It allows production of prototypes or fully functional products with arbitrarily complex geometries, e.g., hollow volumes and honeycomb structures [5]. Its application to metals parts was developed in the late 1980s, thanks to technological advancements such as the increase in computer power and storage capacity that allowed for the processing and storage of three-dimensional models (Computer Aided Design, CAD). Also, powerful directional energy sources were developed, like electron beams and lasers, that allowed the localized heating of metals.

This new technique allows production of metal items with complex geometry, starting from the design and ending with a ready prototype in a fraction of time needed previously for this cycle. It also greatly reduces the cost and lowers necessary skills of a worker who makes a workpiece. According to estimations, this technology saves producers 80% in time and cost needed from design to finalization [6]. More than 70% of metal Rapid Prototyping (RP) methods are laser based [7], meaning that an improvement in laser based AM would have the most beneficial impact on the market.

Metal AM is widely studied and applied in several industrial and research fields. While in some fields it is still at a prototype level, in others it is already used to manufacture commercial products. Examples are medical equipment or mechanical parts for machinery. The ability to produce patient-oriented parts made of bio-compatible metals makes dental and other prosthesis production an immediate application field for AM products. Typical products here are dental

devices; also, production of plates for a skull bone replacement has been reported. Another relevant field of application is the aerospace sector, which constantly requires lightweight components with high mechanical properties for improving the fuel efficiency and reducing emissions [8]. Such components are nowadays successfully printed. In 2015, for instance, engineers at NASA managed to print a rocket component out of copper, which had an intricate internal geometry and limited size; it took only a fraction of the time that would otherwise be required using traditional manufacturing techniques [9]. Similarly, AM is employed in the automotive sector. It allows for a higher variability in designing and manufacturing, and production of construction elements that are both lighter and safer [10]. While its widespread application is somewhat compromised by a low volume production and the need for a post-print refining of components by conventional processing tools, several pieces are already being produced by the AM and embedded in commercial vehicles, e.g., some internal parts of engines or parts embedded in lighting systems [11]. Apart from technically demanding applications, metal AM is also used for artistic purposes [12]. With printers and software becoming cheaper, artists and designers get access to new shapes and geometries that were impossible to obtain before. 3D printers focused on precious metals feature a more efficient powder management, ensuring an improved ratio of captured powder into the final item and quick metal changeover through a cartridge-based system. Also, artwork and jewelry do not require the same levels of certification and mechanical product quality as in other fields, thus proving an attractive and immediate market for AM products.

The two most common metal AM techniques are Powder Bed Fusion (PBF) and Direct Energy Deposition (DED). While they are complementary techniques with different pros and cons, the present work focuses on DED. This is an AM technique

that uses a high energy density source like a laser, electron beam or electric arc focused on a substrate, where it creates a pool of melted material to which the feeding stock is then delivered in the form of wire or powder. Then the heating source continues moving leaving the deposited metal behind to cool down and form a new metal track. The advantages of this technique are a high-throughput, multi-material processing, processing of large volumes, the possibility to deposit new item or repair old ones [13].

Despite the many advantages, there are several technical difficulties that prevent the wider adoption of AM as a reliable production technique. These are the low repeatability, erratic printing flaws, problematic and expensive post-processing work and inspections, and accumulative character of printing defects [14]. Several industries like automotive or aerospace have very tight requirements to the manufacturing process and mechanical properties of parts produced. The AM products can be flawed in different ways, and these flaws hamper their application in these industries.

During the deposition, the substrate and feeding material both undergo several cycles of melting, cooling, and remelting. As in all thermomechanical manufacturing process, this results in formation of residual stresses [15]. This defect can lead to distortion [16], cracking and delamination [17], that can be a cause of premature failure of the component. One of the most critical defects in DED is porosity, the inclusion of small cavities and lacunas within the deposited material. This may arise due to keyholing, gas feedstock carrier, or lack of fusion [18, 19]. The formation of pores depends on the processing parameters, like powder feed rate, hatch spacing, and laser power density [20, 21]. The porosity directly affects the mechanical properties, like fatigue and corrosion resistance. Other common defects are the delamination [22] that leads to the detachment

of consecutive layers, and high surface roughness [23], that makes the post processing of printed parts mandatory.

Metal printed items can be used in real life applications only after a thorough quality monitoring process. Monitoring can be made with both destructive and non-destructive techniques [24]. The first type implies the destruction of the specimen and includes metallographic techniques to assess the presence of internal volumetric defects like crack or pores, chemical techniques to check the presence of contamination and loss of alloy elements, and mechanical testing to ensure the mechanical performance of the specimen. These analyses are performed on test samples prepared on purpose, so their results may differ from the product prepared for the real-world scenario. Non-destructive techniques include a wide array of analyses that can be applied without further modification of the product; they range from the simplest visual inspection used only for gross superficial imperfection to more complex techniques like Computed Tomography (CT) that reconstructs the piece internal structure by merging a series of images taken at different angles. Such techniques can be extremely effective in detecting inconsistencies, internal defects like pores, and generic deviations between the printed piece and the initial CAD design. As a downside, they can be extremely expensive and their operation time consuming, making them not an option for mass manufacturing.

The most effective way to perform quality monitoring on every step of the deposition process is to rely on sensors working on-line and *in-situ*. This allows monitoring the process as it proceeds, introducing corrections in the processing parameters through a feedback loop as soon as they are needed [14]. This allows detecting and correcting flaws immediately or eventually stopping the deposition thus avoiding the further waste of material. There exist different sensors for

monitoring different physical quantities linked to the ongoing process; for example, the light emitted by the hot printed surface, molten pool temperature and geometry, etc. Each type of sensor has its pros and cons. In this context, the Federal Institute for Materials Research and Testing (BAM) of Berlin started a project called Process Monitoring of Additive Manufacturing (ProMoAM), with the goal of studying and developing several monitoring techniques and merging their results to achieve a superior performance in the AM quality assurance and detection of printing defects. Within this project, several analytical methods have been employed, for instance, thermography to detect temperature distribution in and around the molten pool [25] and the Eddy current method to detect artificial defects [26].

The work presented in this thesis has been done in the context of the BAM ProMoAM project. Here, a portable spectroscopic set-up has been attached to a DED printer to on-line monitor the deposition process, investigate how a change in processing parameters effects the molten pool emission intensity, and detect possible defects created during the printing. An optical set-up made of portable spectrometers has a potential to become a useful on-line sensor because it can record light in different spectral ranges, it is sensibly cheaper and easier to handle than thermal cameras, and because it can deliver results in real time without requiring high computational power. In the thesis, the potential of such a system is explored not only empirically but also through a simulation. A simplified thermal model is used to simulate the emission from an AM experiment, and the simulated emission is studied using the same statistical methods as that employed in the real-life experiments.

This thesis is organized as follows. In Chapters 1 and 2, the basic physical and technological aspects of AM are reported starting from the laser-matter

interaction and ending by a description of how printing defects are formed and detected. In Chapter 3, the optical sensor attached to the DED printer is explained in detail. Results of several metal deposition experiments are reported, and it is explained of how to calculate one of the most important processing signatures, the molten pool temperature. In Chapter 4, a detailed description is given of how this sensor can be used for the on-line detection of printing defects with the help of different types of data processing techniques. This ability is certified using artificial defects with known size and position on a printing substrate, which act as the “defect standards”. The same experiment has been simulated, and the simulation results are compared to that obtained in experiment. Finally, in Chapter 5, the short summary is presented, and conclusions are drawn.

# 1 Laser-matter interaction

In this chapter the working principles and main characteristics of solid-state laser are introduced, along with a brief historical context. The peculiarities of a laser beam are revised in order to introduce what makes it a crucial tool in the field of metal machining. The optical properties of metal are briefly explained, their response to light of different wavelength and intensities, in order to address why the use of different laser according to the modification performed. Finally, the topic of laser-metal additive manufacturing is introduced as resulting from the evolution of former techniques, together with the laser characteristics needed to perform it.

## 1.1 Solid state lasers

Laser is the acronym for Light Amplification by Stimulated Emission of Radiation, its theory is dating back to 1917, when Einstein[27] theorized about the stimulated emission of radiation. Stimulated emission happens when a photon interacts with an excited atom, forcing it to emit a second photon in phase with the first one. If an atomic system has more electrons on the upper energy level involved in the transition than electrons on the lower energy level, then the system is at an inversion of population state and acts as a light amplifier. For this to happen the system needs to have more than two energy levels available to the electrons involved in the transition, otherwise the inversion of population is not possible[28]. In Figure 1 are reported the three and four laser level schemes:

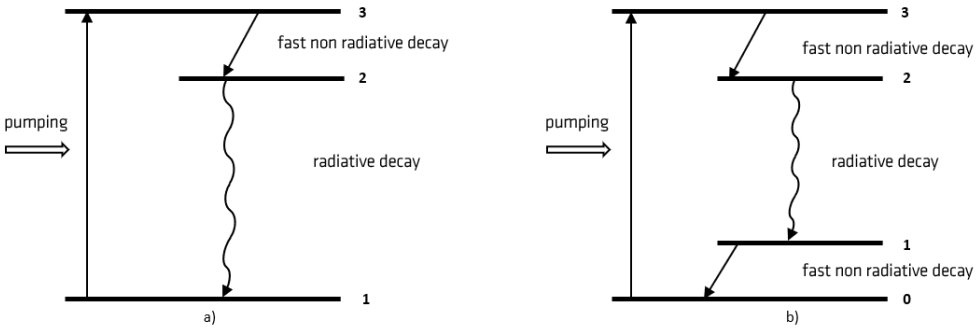


***Figure 1*** *- Schematic of a three-level (a) and four-level (b) laser.*

For a laser to be efficient, the active medium must have most of the electrons on the upper lasing level available to decay radiatively. Calling τ the lifetime of an electron at an excited energy level, lasing can be achieved only when $\tau_2>(\tau_1,\tau_3)$ and the pumping mechanism efficiently depletes the lower lasing level.

Many Additive Manufacturing (AM) techniques require a source of heat to manipulate matter, and for different materials, especially metals, a laser is the optimal choice, since it provides a focused beam with high energy that can be modified and guided through different optical systems. In this field, the most important parameter for a laser is the highest power available in the output, along with the wavelength, shape of the beam, and an operational mode: pulsed or Continuum Wave (CW). The most common light source was a $CO_2$ laser, with a gaseous active medium electrically pumped and emitting around 10μm. In recent years, solid-state lasers gained popularity thanks to a wide set of characteristics that increase their appeal for working with metals[29].

An active medium in a solid-state laser is a crystal doped with ions. Generally, these ions are those of rare earth or transition metals, while the crystalline host is a complex oxide, like $Y_3Al_5O_{12}$ (YAG), or a fluoride, like $YLiF_4$. A suitable host must accommodate the active ion, it should have an intrinsic cation with a size like the one of the ions, and its mechanical properties should not be worsened by doping. The oxides are usually harder and have better thermo-mechanical properties,

while the fluorides show better thermo-optical properties. Among the oxides are also some types of glass, which by nature have worst thermal conductivity leading to worst properties. The interaction between ions and host crystal is such that they result in a very low radiative transition probabilities, leading to long radiative lifetimes. Considering σ as the stimulated emission cross-section and τ the overall lifetime of the electron on the upper state level, this results in a high value for the product στ. This implies a low value for the threshold pump power, which is inversely proportional to $1 / \sigma\tau$.

***Table 1*** *- Optical and spectroscopical parameters in comparison between Nd and Yb as active medium in a YAG host. $N_t$ is the dopant concentration, τ the fluorescence lifetime, Δ the transition linewidth, $\sigma_e$ and $\sigma_a$ the effective stimulated emission and absorption.*

| | Yb:YAG | Nd:YAG |
|---|---|---|
| | $\lambda_{em}$ = 1.03 μm | $\lambda_{em}$ = 946 nm |
| doping [at. %] | 6.5 | 1.1 |
| $N_t$ [$10^{20}$ ions/cm$^3$] | 8.97 | 1.5 |
| τ [ms] | 1.16 | 0.23 |
| $\Delta\nu_0$ [cm$^{-1}$] | 86 | 9.5 |
| $\sigma_e$ [$10^{-20}$ cm$^2$] | 1.8 | 2.4 |
| $\sigma_a$ [$10^{-20}$ cm$^2$] | 0.12 | 0.296 |
| Refractive index | 1.82 | 1.82 |

Lasers with Nd as an active ion can be constructed with different hosts, the most common of which is YAG, where some of the $Y^{3+}$ ions are replaced by $Nd^{3+}$, with

doping normally between 1% and 4%. Nd:YAG lasers can be pumped by a lamp or a semiconductor laser, and the output may be CW or pulsed[30]. As aforementioned, a common field of application for this instrument is in material processing, like welding or drilling; for the former, a typical average power of 2 kW is deployed, whereas for the latter, a lower beam power, up to 100 W, is used, both operating in a pulsed mode. Other applications are found in medical field and environmental measurements.

Another common solid-state laser used in metal machining is Yb:YAG. It uses the same crystalline host YAG, but Ytterbium ions instead of Nd, it emits approximately at 1.03 µm with a quasi-three-level laser scheme, as depicted in Figure 2, despite other lasing schemes are available. This level scheme allows for efficient pumping by semiconductor laser diodes, which can provide the required pumping power. The intrinsic differences between Nd: and Yb: YAG lasers are reported in Table 1.

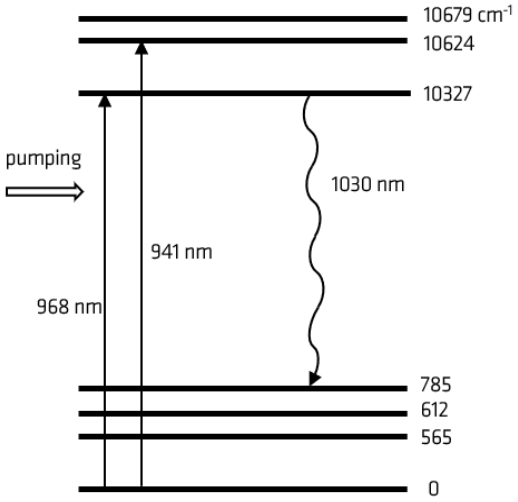


*Figure 2 - Yb:YAG energy levels available for pumping and lasing.*

For this laser, a good optical-to-optical pumping efficiency of approximately 60% is recorded[31], and an output power in the range of kW is available at a room temperature operation[32], while more than two hundreds Watts are achieved

with cryogenic cooling[33]. When compared to the similar quasi-three-level Nd:YAG solid state laser, the Yb:YAG laser presents several advantages: a low amount of quantum defects, long radiative lifetime that favors Q-switching, low fluorescence quenching, and high gain due to the low stimulated emission cross-section. This last characteristic, however, implies a high energy lasing threshold, which is considered a limitation.

In recent years, the Yb:YAG laser started to disclose its potential in several metal machining fields. It is used in welding experiments with different output powers or lasing wavelengths, to study the processing parameters that grants the best output[34, 35]. In [36] the laser is used for precision milling of Yttria-stabilized zirconia and is preferred over the Nd or $CO_2$ lasers since it is more suitable for diode pumping and delivers high power beams at a larger number of wavelengths. Finally, in the form of a disk or fiber laser, it is being extensively used also in additive manufacturing, both with powder bed fusion[37, 38] and with laser metal deposition[39].

## 1.2 Characteristics of the laser beam

The laser main and most interesting properties follow from the physics behind it, and they are *monochromaticity*, *directionality*, and *temporal and spatial coherence.*

The active medium amplifies only radiation with a frequency matching the energy of the transition involved. It is placed in a resonant cavity, which further narrows the laser linewidth with respect to spontaneous emission at the same wavelength. The produced beam is then monochromatic, it means it contains a limited number of wavelengths, called a laser bandwidth. The photons emitted due to stimulated

emission have the same wavelength and phase, resulting in a coherent beam of light. Another consequence of the cavity geometry is that the beam produced is highly directional, meaning it travels in space with a very narrow degree of divergence, as opposed to thermal sources whose emission is usually isotropic. From the property of directionality follows the most important property for a laser in the field of heavy material processing, the brightness. This is defined as the power emitted per unit surface area and unit solid angle. While the light intensity is a quantity that can be manipulated by an optical system, the brightness is invariant of a device.

The laser cavity is an optical resonator, its longitudinal modes define the allowed output wavelength, while its transverse modes define the shape of the intensity distribution of the emitted beam. The most common spatial profile for a laser light is Gaussian, depicted in Figure 3.

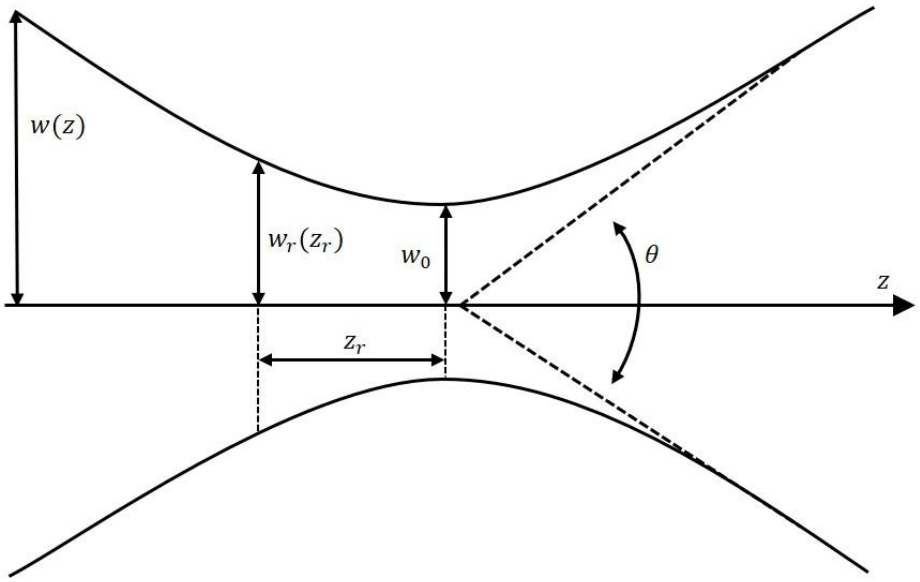


*Figure 3 - Gaussian profile, where: $w_0$ beam waist, $z_r$ Rayleigh range, $\theta$ divergence angle.*

The intensity profile is described by the equation:

$$I_{(r)} = I_0\, exp\left(\frac{-2r^2}{w(z)^2}\right) = \frac{2P}{\pi w(z)^2}\, exp\left(\frac{-2r^2}{w(z)^2}\right) \tag{1.7}$$

where $I_0$ is the peak intensity at the beam center, r is the radial distance from the beam axis, w(z) is the beam radius where the intensity is $1/e^2$the intensity of $I_0$, P is the beam total power, and z is the distance from a plane with the flat wavefront.

The beam profile is not constant as it travels through space, because diffraction changes its shape. The beam profile can be described by first defining the beam waist $w_0$, that is the narrowest beam cross section, on both sides of which the beam diverges with the divergence angle $\theta$. The beam waist radius and the divergence angle are linked to one another through the wavelength:

$$w_0 = \frac{\lambda}{\pi\theta} \tag{1.8}$$

The beam diameter around the beam waist region along the direction of propagation z is:

$$w(z) = w_0\sqrt{1 + \left(\frac{\lambda z}{\pi w_0^2}\right)^2} = w_0\sqrt{1 + \left(\frac{z}{z_r}\right)^2};\ z_r = \frac{\pi w_0^2}{\lambda} \tag{1.9}$$

Where $z_r$ is called Rayleigh range, a distance from the beam waist where the beam diameter $w_r(z_r)$ is $\sqrt{2}*w_0$. This quantity is also called a depth of focusing, since within the Rayleigh range on both sides of the beam waist, the beam is considered in focus.

It is possible to focus or defocus such a beam with thin lenses and still get a Gaussian profile in output. The beam waist and divergence angle before and after a focusing lens are related through the magnification of the optical system:

$$w_0' = w_0 \frac{f}{\sqrt{(|s| - f)^2 + z_r^2}} = \alpha w_0 \tag{1.10}$$

$$\alpha = \frac{f}{\sqrt{(|s| - f)^2 + z_r^2}} \tag{1.11}$$

Where s is the object distance, f is the lens focal distance, $w_0'$ is the focused beam waist, and α is the magnification factor. This implies that it is possible to reduce a beam size by reducing the lens focal length, thus increasing the fluence, that is useful for most material processing techniques. The divergence angle is also negligible at distances both very close and very far from the beam waist, since in those points the beam is almost collimated. Considering a collimated beam at the input of an imaging system, the output beam waist will be in its focal plane.

It is possible to evaluate the beam quality and to compare different sources using a parameter called the M squared:

$$w_0 \theta = \frac{M^2 \lambda}{\pi} \tag{1.12}$$

The product of the beam waist radius and divergence angle is invariant of every beam transformation and is called the beam parameter product, BPP. For a diffraction limited Gaussian beam, $M^2$ is equal to 1, while for real beams it is greater than unity, so this index measures a beam deviation from the ideal Gaussian profile. When a collimated beam with divergence $\theta$ is focused by a lens of a diameter D and a focal length f, the focal beam radius $w_f$ is:

$$w_f = \frac{M^2 \lambda}{\pi} \frac{2f}{D} = w_0 \theta \frac{2f}{D} = BPP \frac{2f}{D} \tag{1.13}$$

In order to reduce the beam waist, a focusing lens must have a large diameter and a small focal length, even if the smallest value achievable is still limited by $M^2$.

While different light sources may be useful in different application fields, in material processing, a source with a low $M^2$ and BPP is desirable for various reasons[29]: i) a lower $M^2$ value allows for smaller beam waist, leading to a higher radiation power density, that is useful to reach or exceed the energy threshold needed for several machining procedures; ii) at a low $M^2$, the resulting beam waist length also increases, making the set-up less sensitive to positioning error; iii) a laser with a native small beam waist allows for more flexibility in the optical set-up, since it is possible to use lenses with a greater focal distance or smaller diameter, without increasing sensibly the beam dimension.

## 1.3 Laser-metal interaction: absorption and reflection

Metals are characterized by the presence of quasi-free electrons moving in the bulk material, which are responsible for most of their optical properties. When an electromagnetic wave interacts with an electron it exerts on it a force equals to:

$$\boldsymbol{f} = -e\left[\boldsymbol{E} + \left(\frac{n_1}{c}\right)(\boldsymbol{v} \times \boldsymbol{H})\right] \tag{1.14}$$

Where e is the electron charge, $\mathbf{E}$ and $\mathbf{H}$ are the incoming electric and magnetic waves, $n_1$ is the material refractive index, c is the speed of light and $\mathbf{v}$ is the electron velocity. The contribution from the magnetic field is small enough so that the force is approximated to -e$\mathbf{E}$.

For an absorbing medium, the refractive index should be expressed as a complex number $\mathbf{n} \equiv \boldsymbol{n_1} + \boldsymbol{i n_2}$, where $n_2$ is also called the extinction coefficient. It is possible to derive the link between a refractive index and medium optical properties through the Maxwell´s equations. Considering a plane wave of frequency ω propagating into a nonmagnetic isotropic material with dielectric constant **ε** and electric conductivity **σ**, it can be proved that:

$$n^2 = \varepsilon + i\,{}^{\sigma}/_{\varepsilon_0 \omega} \equiv \boldsymbol{\varepsilon} = \varepsilon_1 + i\varepsilon_2 \tag{1.15}$$

The function $\boldsymbol{\varepsilon}$ is called the complex dielectric function and it is specific to a material. It depends on frequency, magnitude, and direction of the incident field, and dictates how the material responds to an electromagnetic stimulus. Its components are connected to real and imaginary part of the refractive index:

$$\varepsilon_1 = n_1^2 - n_2^2 \tag{1.16a}$$

$$\varepsilon_2 = 2 n_1 n_2; \tag{1.16b}$$

$$n_1^2 = \frac{|\varepsilon| + \varepsilon_1}{2} \tag{1.17a}$$

$$n_2^2 = \frac{|\varepsilon| - \varepsilon_1}{2} \tag{1.17b}$$

The metal free electrons are not bound to specific energy levels but interact with the solid lattice through collisions, with an average collision time $\tau_e$, also expressed as the reverse of the electron-ion collision frequency $\gamma$. Classically, an electron bound to an atom is described as a harmonic oscillator, with a resonance frequency and an oscillator strength. For electrons in the metal conduction band there is no resonance frequency and the oscillator strength equals to one, so the dielectric function is:

$$\boldsymbol{\varepsilon} = 1 + \omega_{\boldsymbol{p}}^{\boldsymbol{2}} \frac{-\tau_{\boldsymbol{e}}^{\boldsymbol{2}} + \boldsymbol{i}\,\tau_{\boldsymbol{e}}/\omega}{1 + \omega^{\boldsymbol{2}}\tau_{\boldsymbol{e}}^{\boldsymbol{2}}} \tag{1.18}$$

Where:

$$\omega_p = \sqrt{\frac{N_e \mathrm{e}^2}{m_e \varepsilon_0}} \tag{1.19}$$

is the electron plasma frequency[40] that describes the frequency of oscillation of electron density inside the conductive medium. This frequency lies in the vacuum ultraviolet for most metals. While $\omega_p$ does not depend on the light frequency, it dictates different behaviour when the interacting photons have frequencies higher or lower than $\omega_p$.

It is possible to draw an example using the data for copper [1]. In this material the electron number density is $N_e \sim 8.5x10^{28}\ m^{-3}$and the effective electron mass $m_e = 9.1x10^{-31}\ kg$. The values for the electron charge and vacuum dielectric constant are respectively $1.6x10^{-19}\ C$ and $8.85x10^{-12}\ F/m$. It results from eq. 1.19 that copper at room temperature has a plasma frequency of $\omega_p = 1.6x10^{16}\ s^{-1}$, or 20 nm that is in the X -ray region.

The response of a copper sample to an optical stimulus with the increasing frequency is plotted in Figure 4, where three main regions are seen. For incoming photons with low frequency, the electrons fluctuate with the frequency of the radiation field, thus absorbing it. As the radiation frequency increases, the metal

first becomes reflective and then transparent when the photon frequency matches the metal plasma frequency.

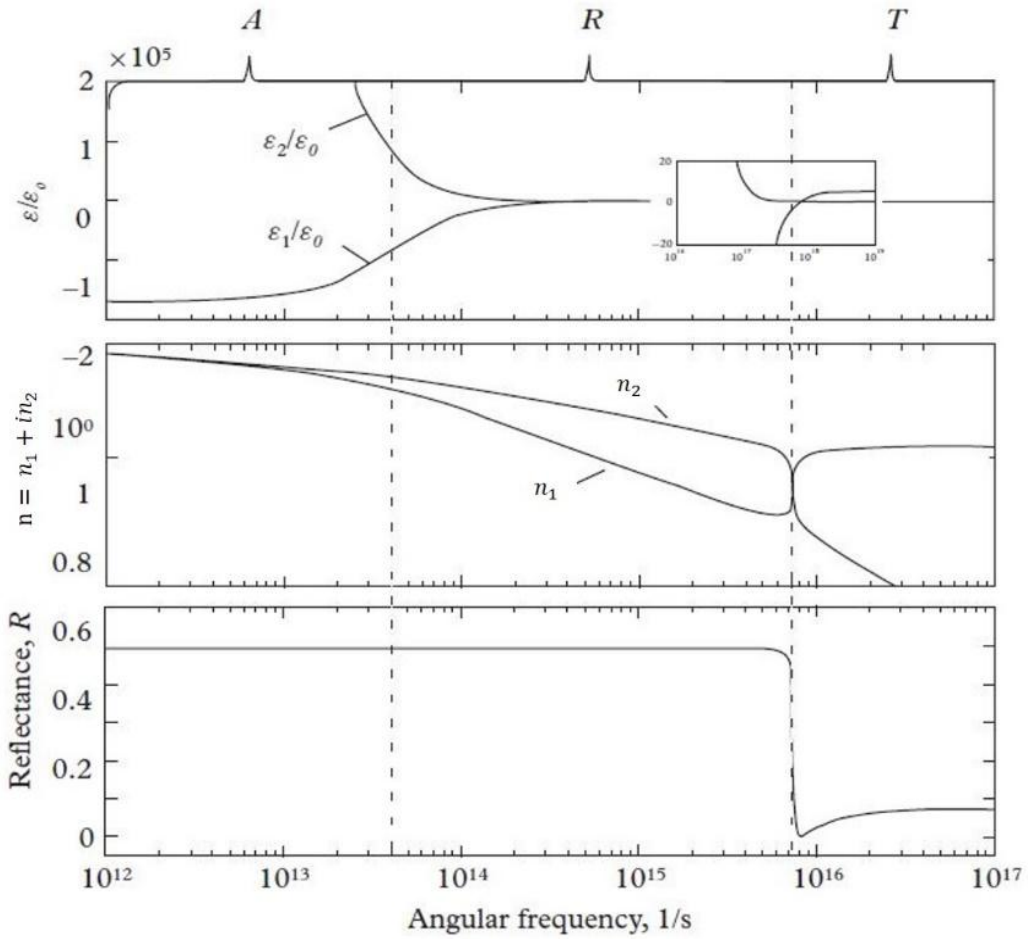


*Figure 4 - Reflectance (R), refractive index (n) and dielectric function (ε) for copper are plotted against incoming light frequency ω. The plot is divided in three regions according to which behaviour predominates, absorptive (A), reflective (R) and transmissive (T). [1]*

What matters the most on a practical level is the absorption coefficient of a material at the wavelength of interest, because only if a laser is efficiently absorbed by the metal, it will transfer its radiant energy to the free electrons and to the crystalline lattice, resulting in the metal heating up. In Table 2, the absorption coefficients are reported for a variety of materials in powder form, for two common wavelengths. This comparison is especially interesting since it shows that some metals have the higher absorbance at lower wavelength, making Nd or Yb lasers more suitable than the $CO_2$ lasers.

*Table 2 - Absorptivity of various materials in a loose powder state at the operating wavelength of Nd:YAG and CO2 lasers.[2]*

| Material | Nd:YAG laser (1.06 μm) | $CO_2$ laser (10.6 μm) |
|---|---|---|
| | Metals (%) | |
| Cu | 59 | 26 |
| Fe | 64 | 45 |
| Sn | 66 | 23 |
| Ti | 77 | 59 |
| Pb | 79 | - |

It is now clear the advantage of using a laser as a source of energy for various metal machining techniques. Lasers with different powers and scanning speeds allow for different machining options for various elements, as summarized in Figure 5. For instance, it is possible to perform material modification in one, two or three dimension, like drilling, cutting, scribing or threading[41]. Two metals can be locally heated and melted in order to fuse them together in a weld; the two pieces can have different shapes, like plates, tubes or wires[42]. If different metals are completely fused together and not only in a limited volume, then the technique is called Additive Manufacturing (AM), even though the definition of welding and AM somehow overlaps.

In this work the optical emission from a steel additive manufacturing process is exploited as monitoring tool to assess the process itself. It is carried with a laser power of approximately 1 kW and scanning speed of 10~20 mm/s, as summarized in Table 5. These are the typical processing characteristics for welding and cladding (Figure 5), that is expected due to the resemblance between these techniques and additive manufacturing.

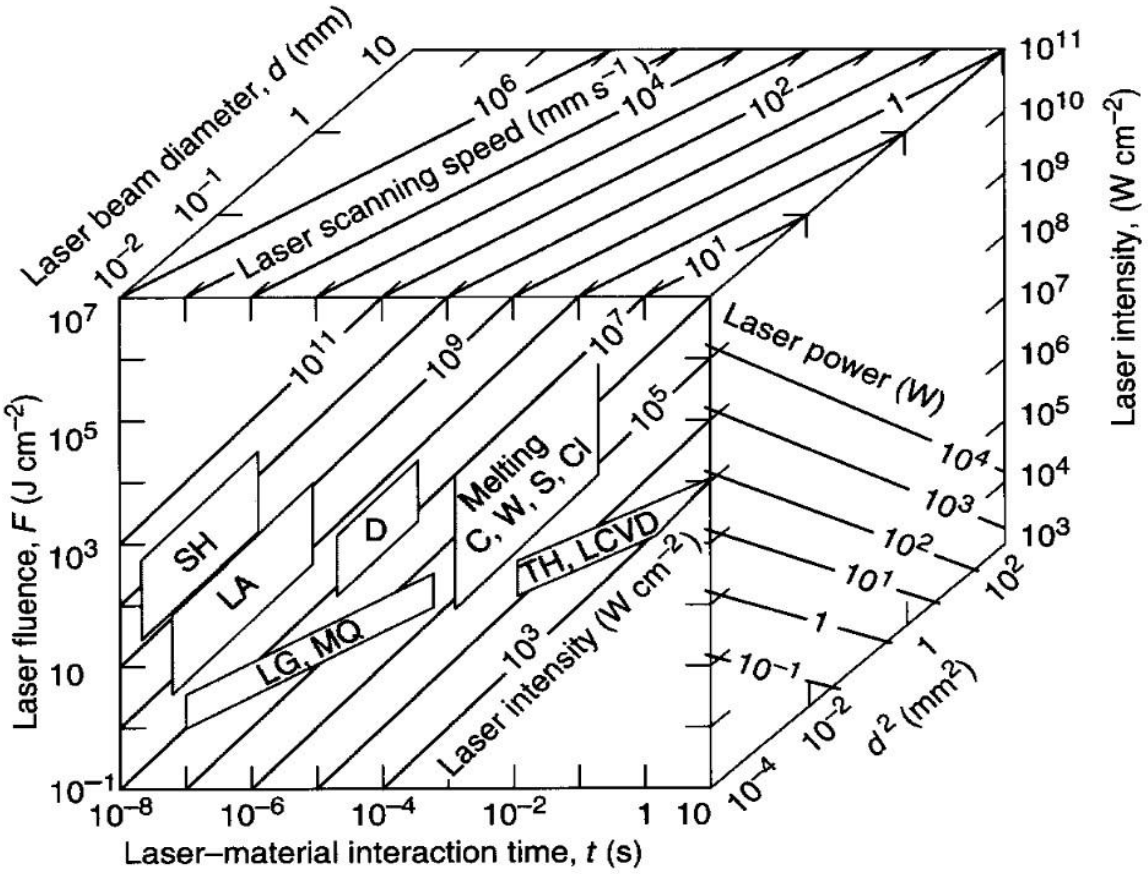


*Figure 5 – Laser parameters regimes for various types of materials processing. TH, transformation hardening; LCVD, laser chemical vapor deposition; C, cutting; W, welding; S, surface alloying; Cl, cladding; D, drilling; LG, laser glazing; MQ, melt quenching, LA, laser ablation, thin-film deposition, micro-machining; SH, shock hardening[3].*

# 2 Laser-metal additive manufacturing

This chapter describes the topic of this work, metal additive manufacturing, an important tool for rapid prototyping. It reports its basic mechanism and the processing parameters involved, followed with an extensive review around one of the key points tackled in this work, the creation of defects while depositing a metal piece. These defects are described and organized in categories. Finally, this work aims to exploit optical monitoring in order to monitor the printing process

and detect defects formation online, so a comprehensive review of the most common techniques and devices used in this field is presented.

## 2.1 Definition and scope

There are historically several techniques used to form metal products, like casting and molding, often accompanied by post-processing machining operations necessary to finalize the part. Most of these techniques allow the production of pieces with high precision and throughput, especially when integrated into a production pipeline, but with limited geometric complexity. With the advent of Additive Manufacturing (AM), though, it is now possible to produce parts, starting from computer-generated models and base material in form of powder or wire, with complex geometry and little-to-no need for postprocessing.

AM is a production technique defined by the International Organization for Standardization (ISO) as a "process of joining materials to make parts from 3D model data, usually layer upon layer, as opposed to subtractive manufacturing and formative manufacturing methodologies" [43]. Several AM techniques exist, divided according to process and materials used. The first apparatus for stereolithography was patented in 1986 [44], and together with others patented shortly after, allowed production of pieces made of polymers, wax and other malleable materials [45]. Few years after, another device was patented [46], using Selective Laser Melting (SLM) to produce metal parts.

The most common techniques to produce complex metal parts are nowadays Powder Bed Fusion (PBF) and Directed Energy Deposition (DED), both deploying powder as building starting point. Powder-baser additive methods proved to be versatile and able to produce parts with a topology and structure not achievable

with traditional techniques [47], they can deploy powder made of different materials and are therefore used in various fields of application [22, 48-51].

AM techniques are gaining popularity in production industries, but are also burdened by severe drawbacks, like lack of reliability and repeatability, high starting costs, loose standard international guidelines [52-55].

These problems must be tackled from several angles to allow AM to be broader accepted in the industry:

- Deep understanding of defects nature and formation mechanisms are needed, to assess their influence on the final piece and aid in their detection;
- Quality control should be brought online, with monitoring devices able to recognize a flawed piece while is printed;
- The printed piece must have reliable and certified mechanical properties, especially when printing with valuable feedstock materials or with complex geometries.

In this work, a set-up for non-destructive online monitoring is applied to a DED system printing with steel powder, with the aim to characterize the deposition process and to timely detect potential unwanted features happening while printing.

## 2.2 Additive manufacturing mechanism

DED, also known as Laser DED or Laser Engineered Net Shaping (LENS), is a powder-based metal AM technique where a laser is mounted on a moving arm with up to six degrees of freedom. Together with the laser head one or more

nozzles are mounted through which feedstock material and shielding gas are ejected. The nozzles are placed around the laser head in circle so that the laser and the powder stream are focused on the same spot. The deposition takes place on a metal substrate, to which the laser delivers enough energy to create a pool of molten material, on which the powder is directed and melts.

The metal substrate melts at the leading edge of the molten pool and resolidify together with the powder at the trailing edge. The complete melting of both substrate and powder grants their intimate connection after solidification. Every point on the substrate goes through a complex thermal cycle, where there is abrupt heating due to interaction with the laser, followed by a cooling when the laser moves away, and a number of re-heatings and re-coolings due to the scanning of the laser on the plate, depositing following hatches and layers. It follows that the final part can have meta-stable phases and non-equilibrium composition, possibly also in different points of the same printed body [56].

The relative movement between substrate and laser allows for addition of material on a layer-to-layer basis, following a schematic drawn by software, e.g. Computer Aided Design (CAD). The first appearance of such a technique traces back to the early 1990 [57], when printing was done on aluminum. Since the substrate can be included into the final piece, it follows that the deposition can also repair a broken piece or add features to an existing item, i.e. not only create a new body on a flat surface. In this sense DED can be seen as a combination of laser cladding and laser welding.

The technique is applied in very different settings, using diverse lasers, feedstock materials, and geometries. The typical figures of merit are: deposited layer thickness 200-500 µm, minimum layer width 380-1000 µm, a deposition rate up

to 8.3 g/min, with a ratio of feedstock powder effectively deposited up to 90% while working under shielding gas [58].

### 2.2.1 Printing parameters

| Process parameters | Powder parameters |
|---|---|
| Heat source energy | Particle size and distribution |
| Scanning speed | Internal porosity |
| Scanning spot size | Particle shape and topography |
| Scanning pattern | Surface tension |
| Melting environmental condition | Viscosity |
| Shielding gas type and flow rate | Specific heat |
| Laser beam characteristics | Melting temperature |
| Powder mass flow | Thermal conductivity |
| | Absorption and reflectivity |
| | Emissivity |
| | Chemical composition |

*Table 3 - Parameters involved in the DED deposition process that can affect the parts characteristics.*

There are numerous important settings necessary for a successful print, like laser power, laser speed, powder flux etc., reported in Table 3.

In the field of laser material processing, a quick and straightforward relation that links the processing result with the parameters of choice is required. One of these relations regards the energy density [59], expressed as:

$$E = \frac{P}{v_l * d} \tag{2.1}$$

where P is the laser power, $v_l$ is the laser speed and d is the beam diameter. This parameter is used to compare different set-ups with variable laser parameters, since having a comparable energy density delivered is crucial to achieve similar results. Due to the variety of techniques, heat sources and materials involved, it is impossible to define a fixed set of parameters suitable for every situation. There is a range of parameters considered able to provide items with optimal metallurgical and mechanical properties, called processing maps [60, 61].

In other studies, a parameter called normalized enthalpy, which includes the material thermodynamical properties, is used in order to predict the geometry of the deposited track [62-64]:

$$\frac{\Delta H}{h_s} = \frac{\eta P}{\rho h_s \sqrt{\pi \alpha v \sigma^3}} \tag{2.2}$$

Where ΔH is the molten pool specific energy [J/Kg], $h_s$ is the enthalpy of the phase transition [J/Kg], η is the surface absorptivity, P is the laser power [W], ρ is the density of the melted metal [kg/m$^3$], α is the thermal diffusivity [m$^2$/sec], σ is the half width of the beam spot [m], v is the laser speed [msec]. While in many studies the molten pool geometry is linked to only one parameter, like laser power or speed, the normalized enthalpy includes several thermodynamic properties and

processing parameters. If it is plotted against the normalized depth $\delta^*$, that is the weld depth δ normalized with the beam spot σ, the resulting dependence is shown in Figure 6 for different materials.

This behavior suggests that the depth of the deposited layer is linked to the material´s enthalpy, meaning that the laser needs to deliver enough energy to push the substrate through phase transition. Furthermore, the experimental data shows a bilinear trend, highlighting the transition between a conduction welding, a welding mode where the bulk material undergo a phase transition uniformly, for low input energy, and a keyhole welding, where a deep and narrow vapor cavity is formed inside the molten pool, for high input energy [64]. The plotted data do not overlap for all the experimental data, meaning that more work is needed to comprehend the phenomenon and find a more general relation between the processing parameters and molten pool geometry.

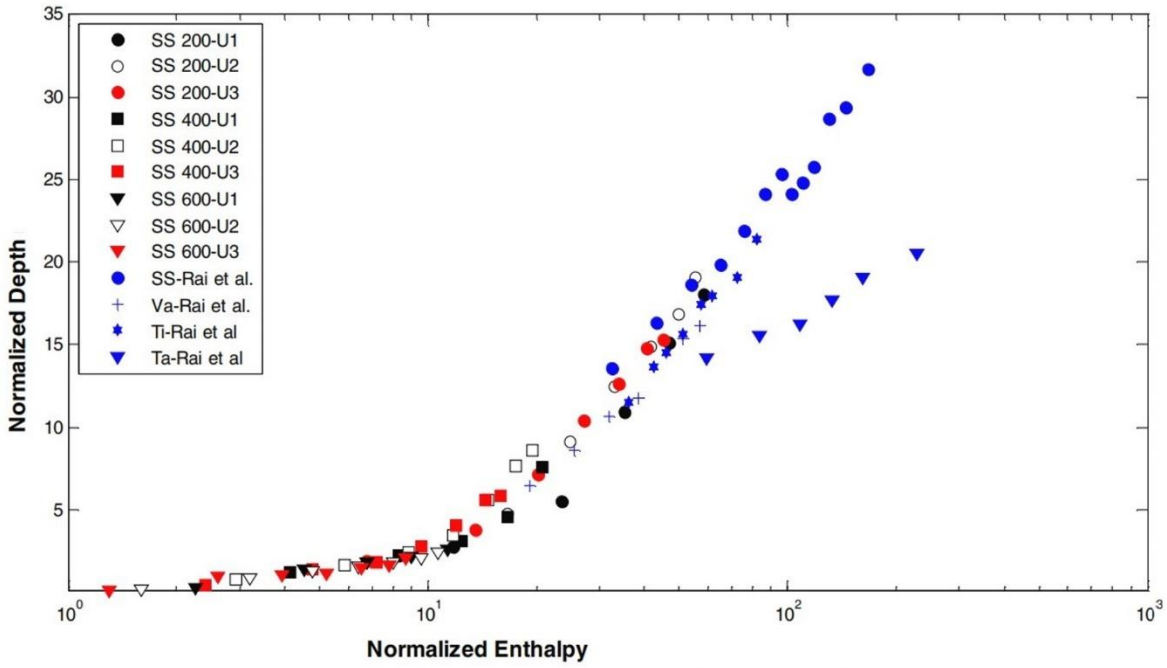


*Figure 6– Normalized depth plotted against normalized enthalpy for different printing experiment. [63, 65].*

The deposition rate of choice should be a compromise between the desired printing speed and the cooling rate of the material, which is in turn related to the

properties of the deposited clad, like the clad texture, homogeneity, and internal structure [66]. Another relevant parameter is the scanning route, the trajectory the laser follows while melting the substrate, consisting in a series of scanning directions. The goal is to optimize the scan route in order to have a uniform heat flow onto the surface of the piece or at least reduce the thermal gradient as much as possible. This optimization should consider material geometry and properties, like thermal conductivity and heat capacity. Common scanning routes are parallel or orthogonal hatches or zigzag patterns [67].

### 2.2.2 Metal properties

The metal involved in DED printing comes in two forms, as plates for the substrate and in powder for the feedstock.

The substrate not only mechanically supports the print but also acts as heat sink, since it faces great thermal gradients. For this reason, there are not only different scanning strategies but also other countermeasures to prevent thermal accumulation, like specific program or preheating [68, 69]. As mentioned, the base plate can be a part of the final workpiece or not. When it is not included, it must be removed after the fabrication with some subtractive technique like cutting or machining. In contrast, it is generally more convenient, both economically and practically, to incorporate it into the final workpiece, if possible.

Powder used as feedstock in metal printing can be pure metal or alloys. As of today thorough investigation has been made for titanium [70, 71] and aluminum [72-75] pure metal printing, while alloys are mostly titanium, nickel and iron based [76]. Titanium is known for being tough, temperature resistant, with high tensile strength and biocompatible, hence it is used in aerospace application and

medicine [75, 77-83]. In contrast, Ni is employed in in the automotive sector and in the production and repairing of components thanks to its oxidation and corrosion resistance and high temperature strength [84].

Chemical composition and metallographic properties of feeding powder, like size distribution, surface chemistry, morphology and internal porosity, affect the quality of the deposited body, its properties and possible defects. Therefore, it is crucial to control and monitor the feedstock accurately, especially if it is recycled from previous prints [20, 85, 86].

The molten pool fluid dynamic is dictated by the interaction of several variables. Surface temperature gradients result in surface currents and mass flow by means of Marangoni effects [87].

A significant advantage of DED with respect to PBF, though, is the possibility to work on feedstock composed of different batch of powders, meaning it is possible to print items with a graded composition, called Functionally Graded Materials (FGMs) [88, 89].

## 2.3 Defect formation

Every item is produced via AM following a blueprint dictated by software, with the intention to achieve a very specific geometry, composition, and properties. Every deviation from this ideal picture is undesirable since it may undermine the workpiece properties. On a practical level, every piece produced has imperfection in it, the nature of which may vary from undetectable and irrelevant to the piece life cycle to the ones that undermine its usability. The former are called *flaws*

while the latter are called *defects*, even though there is still no widely accepted nomenclature in this regard [90].

These defects may arise also from an incorrect printer setting with respect to the material processed or the intended geometry, as reported in Figure 7. This shows how non-matching properly several parameters that influence the piece thermal history, like laser power, speed and route, may lead to poor performance, with the piece suffering under- or over melting during the deposition, resulting in pores and delamination after it. Also, chemical pollution is considered, with the negative outcomes of poor powder quality or oxygen present in the building chamber. Extensive literature has been published on the link between the process parameters and their influence on the workpiece microstructural characteristics [86, 91-93]. A powerful tool to study the relationship between process parameters and the outcome of an AM print is simulation, with consistent work being done to simulate defects originated during laser deposition [94].

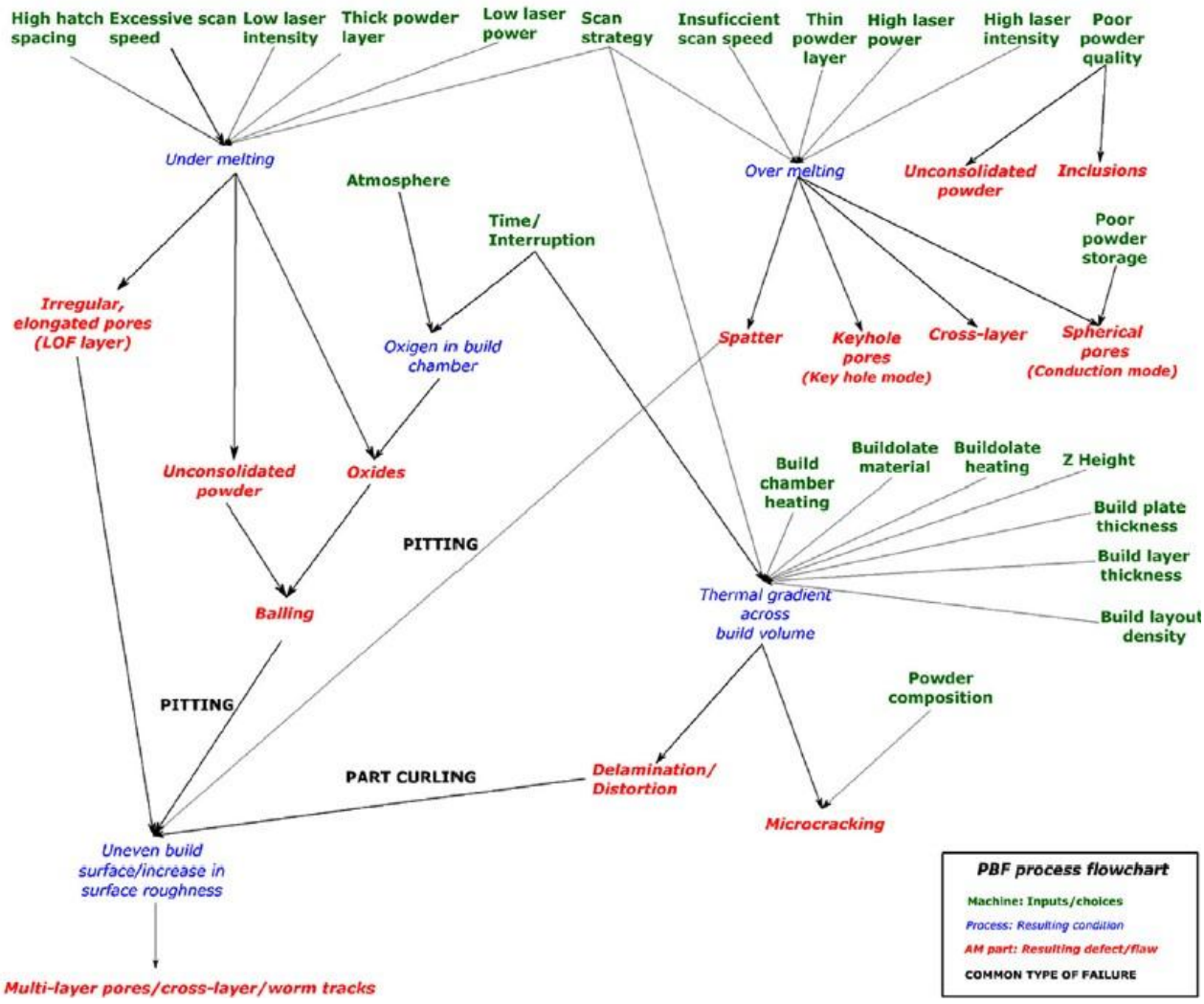


*Figure 7 - Link between incorrect process parameters and their respective faulty outcome during a PBF deposition [90].*

### 2.3.1 Microstructure defects

Any defect related to the internal microstructure of the workpiece affects its uniformity, isotropy, or density.

The thermal history of the produced component, like high heating/cooling rate, defines its morphology and grain size. Anyway, since all the involved process parameters have an influence on the thermal history of parts, the prediction of microstructural characteristics and their cause and consequences remains a key challenge for metallic materials deposited via DED [95]. Two parameters required

to explain the metal final microstructure in the presence of a solid/liquid interface are the local solidification rate (R) and temperature gradient at the solid/liquid interface (G). When printing with an alloy, the ratio G/R determines the mode of solidification, while the product GR dictates the size of the solidification structure, as summarized in Figure 8. Keeping the solid/liquid interface stable while welding or depositing is crucial if a consistent microstructure in the final piece is needed, that explains the difficulty in finding appropriate processing parameters for any specific material involved.

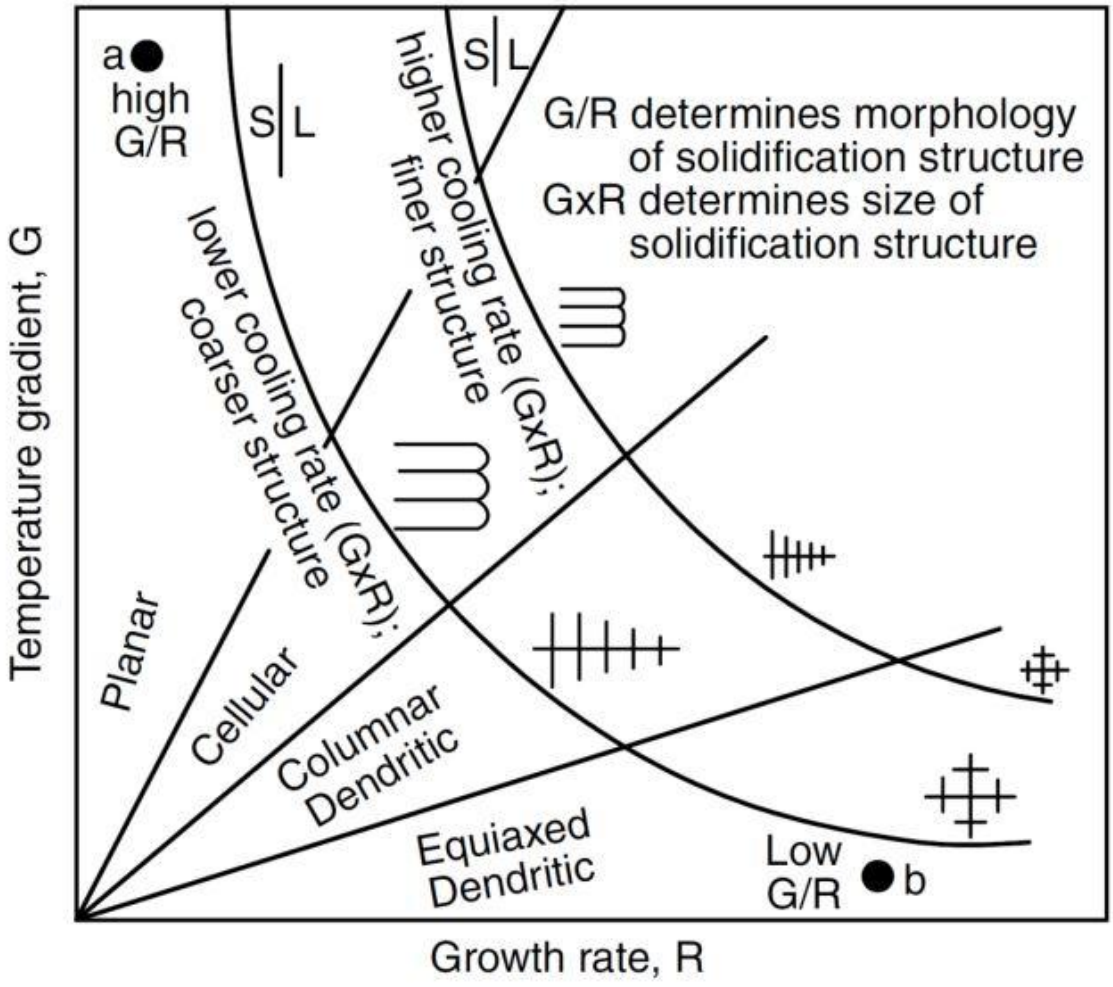


*Figure 8 – Plot of temperature gradient G versus growth rate R and their effect on the solidification microstructure [16].*

Actual testing methods able to characterize the material microstructure are often unsuitable for an industrial environment aiming to produce large quantities of products, since they require extensive sample preparation and are often destructive. In this regard, electron microscopy (SEM) and electron backscattered diffraction (EBSD) are techniques of choice for characterization of porosity, grain size, shape and orientation of anisotropies. There are also non-destructive testing methods, like x-ray-based tomography, but they pose several constraints on the material geometries and have a limited throughput.

#### 2.3.1.1 Porosity

Very common defects consist of a volume inside the printed piece filled with a gas or non-melted material. Categorized into two main classes, these are the gas porosity and lack of fusion (LOF) [92].

##### Gas Porosity

This defect may arise from different sources. The first is the shielding gas used to deliver the powder or to shield the molten pool from atmosphere, the second is the gas already entrapped into feedstock powder, last is an effect of Marangoni flow, a mass flow phenomenon happening when two surfaces with different surface tension are in contact, which trap gas bubbles into the molten pool preventing their escape [96].

Feedstock powder can be produced by two different techniques, gas atomization (GA) and Plasma Rotating Electron Process (PREP). It has been proven that powder produced with the former technique results in a printed sample with three times higher the intralayer porosity with respect to samples made of powder produced with the latter method. The porosity recorded in the sample is not the same amount of the one measured in the feedstock powder, meaning

that porosity is not simply transferred from one to another, but other factors are involved [97].

Printing at high energy density can remove some smaller pores, but can as well introduce other defects, like surface roughness and density variation [98]. The former may be the result of high molten pool temperature, which decreases the surface tension causing the spreading of melted metal on the plate surface. Additionally high energy may cause localized selective evaporation, leading to local cooling and reduction of density. On the other hand, printing at low energy density may lead to pore formation due to insufficient melting or wide scan spacing. Also the influence of the scanning speed has been evaluated, a positive correlation was found between the laser scan speed and surface fragmentation [99].

Lack of Fusion (LOF)

This type of porosity is specific of not fully melted parts and characterized by cavities present in the bulk of the workpiece within a deposited layer or across layers. This cavity can be empty or possibly contain non melted powder. It results from processes with low energy density, i.e. either at low laser power, or high laser scan speed, or improper hatch spacing [90]. It is one of the most important defects in welding and AM, due to its impact on the piece mechanical properties, density and fatigue resistance. Post-building detection of this type of defect is challenging, since it is checked via fatigue test that may in turn initiate a crack where the bond is particularly weak, with the need to then discard the piece. But if the test is not conducted, the crack may be initiated in the real life application, posing an even bigger threat [94].

Another source of LOF may be the difference in elemental composition at the boundaries with two different batches of powder, with different melting temperature, resulting in the final structure having LOF. This leads not only to internal pores but also to poor melting and mixing, which in turn promote delamination. Not only increasing the local energy density but also preheating powder feedstock and using finer powder can be helpful in this regard [100, 101]. An incorrect energy density may arise from an improper positioning of the laser head, that results in a defocusing of the laser and, hence, a lower power delivered on the base plate [96].

#### 2.3.1.2 Anisotropy and crystalline structure

It has been demonstrated how the process parameters, influencing the molten pool temperature, have an influence on the grain structure of the printed piece [93], the distribution of crystalline phases, and the likelihood of metastable phases formation [102] and may induce surface thermal gradient, which in turn brings a variation in microstructure and phase stability [103]. Also, the printing atmosphere can affect the phase stability and microstructure. In the presence of air, the oxygen can oxidizes the metal, changes the surface texture, and adds impurities that perturbate the internal microstructure, even if the deposition happens under shielding gas [104]. Internal anisotropy of the printed piece is also influenced by changing deposition parameters, like scanning patterns [105] and material used [106, 107].

### 2.3.2 Inclusions

A third type of defects affecting the workpiece internal structure is the inclusion in its bulk of unmelted or foreign material. This can be done on purpose in order to positively affect its properties [108, 109]; otherwise, it is an unwanted and possibly negative feature. The feedstock or base plate material can react with shielding gas forming particles, like oxides or sulfides, up to 1 mm in size, that may seriously damage the workpiece mechanical properties like ductility or resistance to fatigue and fracture. Clearly, the influence of these defects on the part properties are linked to their number, shape, size and distribution [110].

### 2.3.3 Dimensional anomalies

During an AM deposition, an item is built following a blueprint produced by software. The design is saved as a CAD file and then converted into another format readable by the printer. This conversion applies a discretization of the original geometry into discrete meshes, and, as every discretization does, it induces an error like a typical stair-case effect on part surfaces [111]. Also the melt pool dynamics affects the piece outer surface, through the thermal gradient, localized solidification, and particle sputtering [112].

A typical phenomenon affecting external surfaces is balling, occurring when melted material solidifies into spheres instead of solid dense layers. This results in uneven and bead-shaped surfaces with detrimental outcomes on the deposited part. The high viscosity and surface tension of the melted metal are key factors since they prevent full wetting the base material or previously printed layer by the molten metal thus favoring balling [113]. The presence of oxygen in the building chamber or in the feedstock material can lead to formation of oxides,

which in turn may reduce wetting and lead to balling [74]. Potential solutions are increasing the energy density by either increasing the laser power or decreasing the laser scan speed, decreasing the layer thickness and adding deoxidants to the powder.

## 2.4 Online optical monitoring

For AM process to produce a seamless piece, several variables must be considered. The physics of laser-metal interaction is quite complex, and there is not a single set of printing parameters that guarantee a flawless deposition. Even with several post-production monitoring techniques, either destructive or non-destructive, which are able to identify faulty pieces, the quality AM needs rely on on-line monitoring systems that allow detecting defects during the deposition or characterizing freshly printed workpieces.

Several techniques have been applied to online monitor defects formation in 3D printing. A Thermocouple is a cheap sensor which records the base plate thermal history and links it to the presence of defects [114, 115]. Displacement sensors are devices able to monitor the laser position and trace back the molten pool depth. They are used together with other sensors that monitor the molten pool geometry and temperature to feed the data into a feedback loop [116]. The geometrical displacement of the deposition can also be linked to internal residual stresses [117]. One or more transducers can be placed inside the printing chamber, mostly below the base plate, to record the noise signal produced during the print. The result can be used to study and monitor the processing conditions [118], characterize and monitor different kinds of defects [119] or monitor the feedstock powder mass flow [120]. In [121] a high-speed X-ray imaging is used to

monitor in-situ the interaction between the powder flow and the molten pool, especially the amount of powder that is back spattered from the vapor plume or fall onto the molten pool.

While these are the examples of non-optical sensors adapted to the online monitoring of the AM process, the focus of this work will be on optical monitoring systems, like point detectors, thermal cameras, and spectrophotometers.

### 2.4.1 Types of detectors

#### 2.4.1.1 Point detectors

Photodiodes are small and cheap detectors able to absorb light in different wavelength ranges and convert it into a current with intensity proportional to the light absorbed. Silicon and germanium photodiodes can record light in the UV-Visible and NIR ranges that is useful for monitoring thermal emission from a hot surface during AM. They may also detect light from Nd or Yb printing lasers, hence spectral filters are often needed. Since they are small, very sensitive and require only an output reader (a computer or oscilloscope), their use as sensors is common in different industrial scenarios.

In [122, 123], a photodiode was integrated into a bigger optoelectronic sensor to monitor continuously the accuracy of the powder flow. This information was used by a Proportional Integral Derivative (PID) algorithm to correct the powder mass flow. This research shows how crucial it is to have a stable powder mass flow that often cannot be provided by existing powder delivery devices. In other machines a photodiode is combined with other sensors to improve the monitoring capacity. In [124], an imaging system recorded the spatially resolved emission from the molten pool and was coupled to a photodiode that recorded the same emission

with no spatial resolution but at a higher acquisition frequency. In this way, the two sensors complemented each other. In [125], two photodiodes simultaneously recorded the laser beam energy and molten pool emission. This information was plugged into a feedback loop algorithm to keep the deposition quality under control.

#### 2.4.1.2 Cameras

Cameras are devices containing arrays of light sensitive detectors; with appropriate optics they can continuously record images. They are characterized by the recording frequency, wavelength range, dynamic range etc. When monitoring an AM process, the most important characteristic is the spectral range, which is usually in the visible or near infrared range. Cameras can be installed in coaxial or paraxial acquisition geometries to monitor in situ the AM process, as pictured in Figure 9.

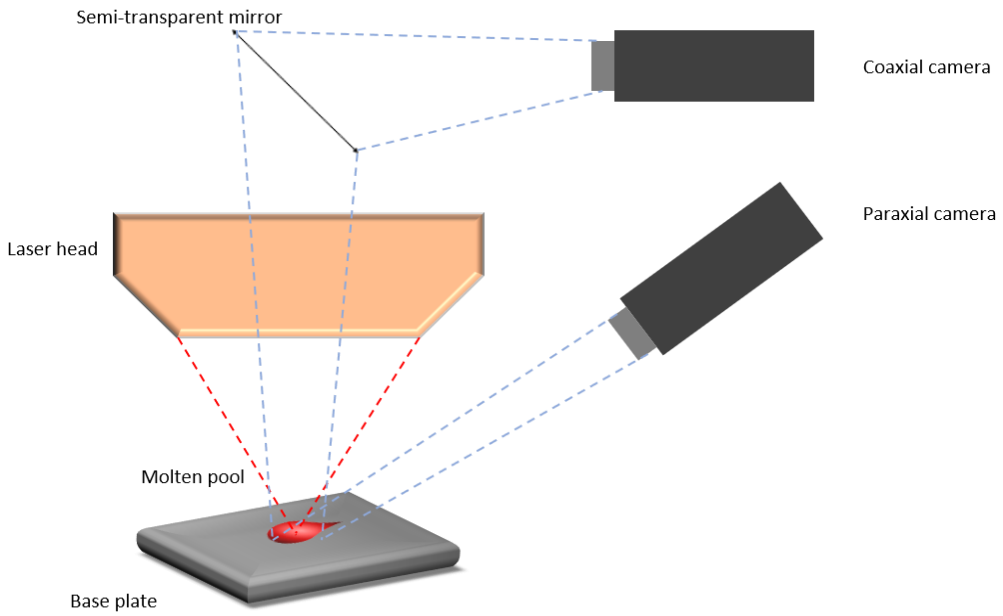


*Figure 9 -Set-up with two cameras, one in paraxial configuration, one in coaxial configuration.*

Cameras are used to monitor several key parameters that are important for a successful print, like the shape and dynamic of the molten pool, the rate of the powder flux, and others. A crucial difference between working in the optical and infrared ranges is that in the first there are several sources of ambient noise, like light sources or molten pool reflections, that can make it difficult to isolate the light source of interest. This problem can be faced in several ways, but never completely fixed. For instance, in some set-ups an external light source is used to enlighten the molten pool [126, 127], which helps increase the image contrast. Lasers are preferred for this application even though LEDs are cheaper and easier to use. Furthermore, optical filters are used in basically every set-up to filter out specific sources of noise, first of all the laser radiation, since most Nd and Yb based lasers fall in the near IR range. Cameras recording in the IR regions are more suitable to monitor process temperature, because laser-heated metal surface in AM emits in the near or middle IR range. In few selected cases it is possible to combine cameras working in the visible and IR and merge results obtained in the two ranges [128].

In order to avoid atmospheric absorption, IR cameras usually work in 3 distinct wavelength ranges, from 800 to 1.7 μm (near IR), 3 to 5 μm (middle IR), 8 to 14 μm (far IR). Considering a temperature between 800 and 2000 Celsius degrees, the peak emission for a grey body lies below 3 μm, hence the most sensitive cameras for monitoring temperature by this technique are the ones working in the near and middle IR.

Whichever the camera is, before using it for measuring a temperature, it must be calibrated with a standard light source, for the appropriate radiative response. It

must also be considered that during AM, metal goes through different physical states with different emissivity, that should be known for an accurate temperature measurement.

*Molten pool and deposition geometry*

Like other sensors, cameras are used to detect specific signals with the goal of linking them to peculiar process signatures, that can reveal in real time the deposition quality.

Coaxial geometry is a key advantage of DED with respect to other AM techniques, since it can provide information about the molten pool width, length, area, and perimeter in real time and without coordinate conversion [122, 123, 129-131]. This kind of monitoring is so useful that most companies incorporate a camera directly into the printer laser head, with built-in filter housing so the customer can choose the spectral range of interest. After the acquisition, images are processed usually with custom algorithms, mostly based on threshold values that can discern pixels detecting emission from the molten pool or from the laser, bright sparkles and so on. From the image, area and profile of the molten pool can be calculated [131]. Some developed algorithms can better isolate the molten pool from other light sources, like plasma plume and bright particulate [132], some do not use a specific threshold but gradients based on the gray scale recorded values [133]. The most common imaging devices record in the visible, but similar algorithms can be applied when recording in the IR range [123, 134], with the clear advantage that in this range information about the temperature field can be used to retrieve the true molten pool geometry [135-138].

The same imaging set-up used to monitor the molten pool geometry can be used as well to measure the deposited layer´s height if the camera is positioned

perpendicularly to the laser beam [139, 140]. With use of multiple cameras in different positions, a stereoscopic monitoring of the newly formed layer is possible [141-143]. It is possible to further increase the number of sensors used to monitor the same parameter, for instance with a trinocular set-up where two cameras monitor the layer height and a third camera improves the monitoring accuracy [144] or with a set-up with three cameras mounted in different positions in order to acquire an image from the camera with the best point of view of the molten pool [145].

*Temperature monitoring*

The AM metal deposition is a thermal process where one or more materials undergo a controlled thermal cycle; that is why the temperature is one of the most critical parameters to monitor. Thermal cameras are well suited for the task.

The most straightforward way to measure the molten pool temperature field is to use CCD [96, 130, 146] or IR cameras [135-137, 147-149] that are previously calibrated with a black body like furnace, or in some cases using the solid-liquid transition temperature as an internal standard to calculate the metal surface emissivity [137]. Most of the sensors are used comparing emitting bodies to black or grey body emitters, which is an intrinsic source of error. For working with grey bodies, it is crucial to accurately calculate emissivity. This can be achieved by coupling an imaging sensor with a pyrometer or a spectrometer [150, 151].

#### 2.4.1.3 Spectrally resolved detectors

Point detectors and cameras can record light emitted by the molten pool in several spectral ranges but provide no spectral resolution. Using a spectrometer allows for spectrally resolved information that opens up a way for a different kind

of monitoring. Optical Emission Spectroscopy (OES) of the molten pool reveals two types of emission. If the laser energy is relatively low, then the melted material emits only continuous thermal radiation, behaving like a grey body. From its emission, it is possible to estimate the material temperature using the same principle on which pyrometers and thermal cameras are based. If the laser delivers higher energy, a plasma can be created above the molten pool containing excited metal atoms and ions. They emit a discrete spectrum, from which the plasma temperature and atoms concentration can be calculated. Both types of emissions are exploited for monitoring purposes.

One way to calculate the temperature from a continuous spectrum is to use the pyrometric ratio method, where the ratio of radiant energies at two different wavelengths is compared to the ratio of theoretical emissivity according to the Plank equation. Similarly, it is possible to fit the whole spectrum to the Plank equation deriving the temperature from the best fit [152]. The raw data recorded must be corrected for a spectral response before the comparison, so the spectrometer should be calibrated with a standard black body emitter. The same procedure can be applied in the visible or in the near IR spectral range. In [39], the emission recorded by a small NIR spectrometer during a laser metal deposition is used to calculate the pool temperature. The molten pool remains at a steady temperature for a brief moment after the laser is turned off, and the emission during the phase transition is used as a correction function to correct the spectra before the Plank fitting. The temperature calculated is used as reference to calibrate the thermal images recorded by two other IR cameras.

If plasma is created, its energy is distributed between degrees of freedom of atoms, ions, and electrons. In plasma at local thermodynamic equilibrium (LTE), this distribution is of the Maxwell-Boltzmann type. This means that by studying

the plasma emission spectrum, it is possible to determine the plasma temperature and elemental composition. In AM plasma is created above the substrate as direct consequence of the laser-matter interaction. It follows that if something influences the molten pool temperature or the substrate surface and geometry, like the presence of a defect, this may be detected by plasma spectroscopy. The light recorded above the printing substrate is the sum of the plasma emission and the molten pool emission. The separate analysis of these two components may disclose information about the AM process. Plasma spectroscopy may provide information other than plasma temperature, which would not require using a calibrated spectrometer. In [153], the authors print on titanium specimens varying the process parameters and recording the combined emission from the plasma and molten pool. As a metric, they use the ratio of the intensity of a titanium atomic line to the intensity of the continuum emission measured in the vicinity of the line. They successfully link the change in this ratio to the presence of defects in this test print experiment. Both the line-to-continuum ratio and integrated intensity are used to monitor an Al composition during deposition of an Al-Ti binary league. This spectroscopy results are fed into an algorithm together with processing parameter to calculate the Al composition in the finished workpiece under different experimental conditions. The whole spectrum can be used to monitor the plasma emission, avoiding isolating single emission peaks. Sibillano et al. suggest using a covariance map to link the laser speed to the loss of alloying elements in laser welding, a technique comparable to DED [154]. Similarly, Valdiande et al. [155] suggest using the average intensity of the recorded spectra to detect defective deposition that occurs under non-optimal processing conditions.

## 2.5 Monitoring with external sources of light

The aforementioned monitoring techniques use signals (optical, acoustic, etc.) generated during the AM process (not counting imaging with an additional light source for increasing the image contrast). While this is the easiest way to monitor the process, there are several interesting methods where an additional light source is used to stimulate an analytical signal recorded by a sensor.

In [156], the authors use an OPO laser to ignite in situ a fluorescence signal from silicon atoms vaporized during a laser weld of steel. This provides an improved sensitivity in comparison to usual OES analysis; the set-up is used as a proof of concept for future application in AM. The same group expands this idea to monitor atomic copper fluorescence from fumes released during welding on aluminum; they link the results to the quality of the welded joint [157].

In [158], the authors developed a custom PBF set-up with an X-Ray imaging system using a beamline from the APS synchrotron. With such a powerful system they managed to monitor the growth of the crystalline phase during a PBF experiment and even record the formation of a keyhole pore. The same X-Ray beamline is used to monitor in situ the AM process with a custom DED set-up; this shed a new light on the behavior of the molten pool. The Investigations clarified the role of powder flux for formation of pores, the interaction of feedstock powder with the laser for keyhole perturbation, and much more [159, 160]. These experiments allowed for better understanding of physical mechanisms involved in AM and laser-matter interaction in particular. However, due to its complexity and difficulty in accessing a synchrotron, the method cannot be considered as suitable for online monitoring in industry.

Lednev et al. [161] developed a custom pulsed Nd:YAG laser with a pulse energy higher than 100 mJ, compact and light enough to be installed on the laser head of a laboratory grade AM printer (Figure 10). The laser induced a plasma on the surface of a molten pool while printing; its emission was collected into a spectrometer and analyzed. This demonstrates the application of laser induced breakdown spectroscopy (LIBS) for in-situ on-line monitoring of the AM process.

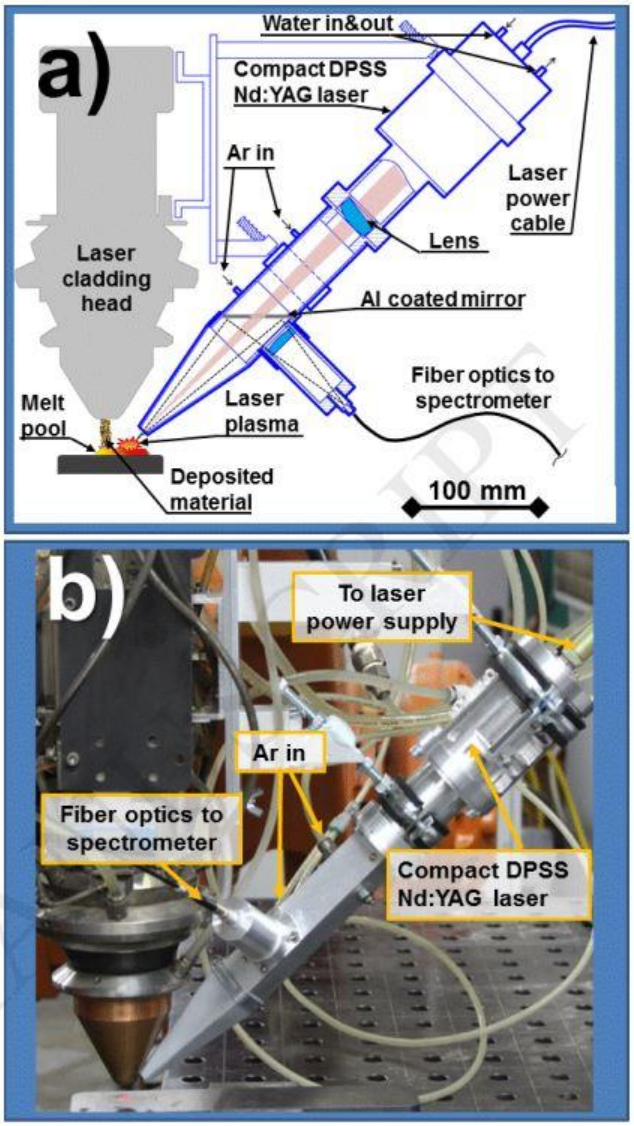


*Figure 10 – a) scheme and b) photograph of the custom LIBS probe plugged on the laser head of an AM printer [161].*

They proved that creating a plasma on the molten pool of the freshly formed workpiece does not reduce the print quality while providing useful information about the composition of the deposited material. Further investigating the same set-up, they proved its usefulness for monitoring the feedstock powder flow by analyzing its nickel and tungsten content [162]. The same LIBS set-up was also used to monitor laser welding [163], thus making it one of the most interesting and universal monitoring techniques in the field of laser metal processing.

## 2.6 Simulation

While online monitoring is crucial for assuring the print quality, it can be quite difficult to characterize monitoring sensors in terms of their response on largely varying process conditions. It would require a tedious optimization and calibration procedure that involves many intertwined parameters. One way to approach the problem is using simulation. With appropriate software it is possible to simulate a physical system and how it responds to a specific user-determined input. While the results obtained may not be universally reliable, they still provide an extremely useful insight into the system's behavior. Such a simulation can be formulated and resolved mainly in two fashions. Analytically, using physical equations that describe the process. This, however, can be an unsurmountable task because solutions to many such equations (e.g. fluid dynamic) are possible only for limited number of simple cases. And numerically, when the equations are solved with a computer on a discrete space-time grid; this provides a solution close to a real one, within a predetermined accuracy.

AM of metals is a complex process since it involves multi-physics phenomena, like phase transitions and fluid dynamic, which should be simulated on the smallest

possible time and space grids to get the best results. A simulation must always be a compromise between the computational power available and the number of variables and computational grid cells [164].

In most cases, the AM processes are reduced to laser heating processes and simulated based purely upon thermal models, where the transient temperature field is predicted solving the partial differential equations determined by energy conservation. In [165], the laser-material interaction is simulated using a model of a moving or volumetric heat fluxes, both having Gaussian spatial profiles. The biggest limitation of this model is not considering the fluid dynamic, which greatly contributes to heat transfer. This results in the overestimated values of the temperature field [166]. Despite their low fidelity, the result from a purely thermal simulation can be coupled with other simulation models, thus resulting in a thermo-metallurgical or thermo-mechanical simulation. In the former, the metal solidification cooling rate is calculated at the end of the solidification cycle, and the thermal gradient is calculated at the beginning of the same cycle. With this, the rate of crystal solidification and a morphology factor are calculated, which allows drawing some conclusion on the metal final crystalline structure [167, 168]. In thermo-mechanical simulations, the temperature fields are used as input for calculating the thermal loads for the metal in a mechanical model, by which the displacement and stress fields are determined [115, 169]. If it is necessary to simulate an AM process with physics related to the fluid dynamic, one of the so-called multi-physics models must be used. These can calculate, besides the temperature, fluid-related variables, like the flow vectors and pressure, at the cost of a greater computational time.

# 3 DED spectroscopy

An optical set-up consisting of one Vis and one NIR spectrometers is used to record light emitted during a DED deposition in order to assess the monitoring possibilities of on-line spectroscopy of the molten pool emission. At first, the reproducibility of the system has been ascertained, then the deposition has been described using the integral intensity and the temperature calculated based upon its optical emission. Further experiments show a predictable change in the light emitted while modifying the laser energy density, and how the recorded light changes when depositing a consistent volume of metal. It is concluded that, while the recorded emission is certainly linked to the printing parameters and geometries, further studies are needed to relate these results to the properties of the deposited items, allowing on-line OES to become a valuable monitoring tool used to further improve the quality in the AM techniques.

## 3.1 Printing, monitoring set-up and acquisition

The experiments are performed printing on flat metal plates and recording the light emitted by the molten pool. The AM set-up is a commercial laser metal deposition machine TruLaser Cell 3000, manufactured by the German company Trumpf (Trumpf GmbH + Co. KG, Ditzingen, Germany). The printer is coupled with a 16-kW continuous (CW) Yb:YAG TruDisk 16002 disk laser, from the same manufacturer, operated at 1030 nm. The motion of the printer has five degrees of freedom: the laser head moves in three directions and tilts in one direction by an angle of up to 135° and the sample holder (a rotatory stage) rotates around a perpendicular axis. The volume of the printing chamber is 800 mm x 600 mm x 400 mm.

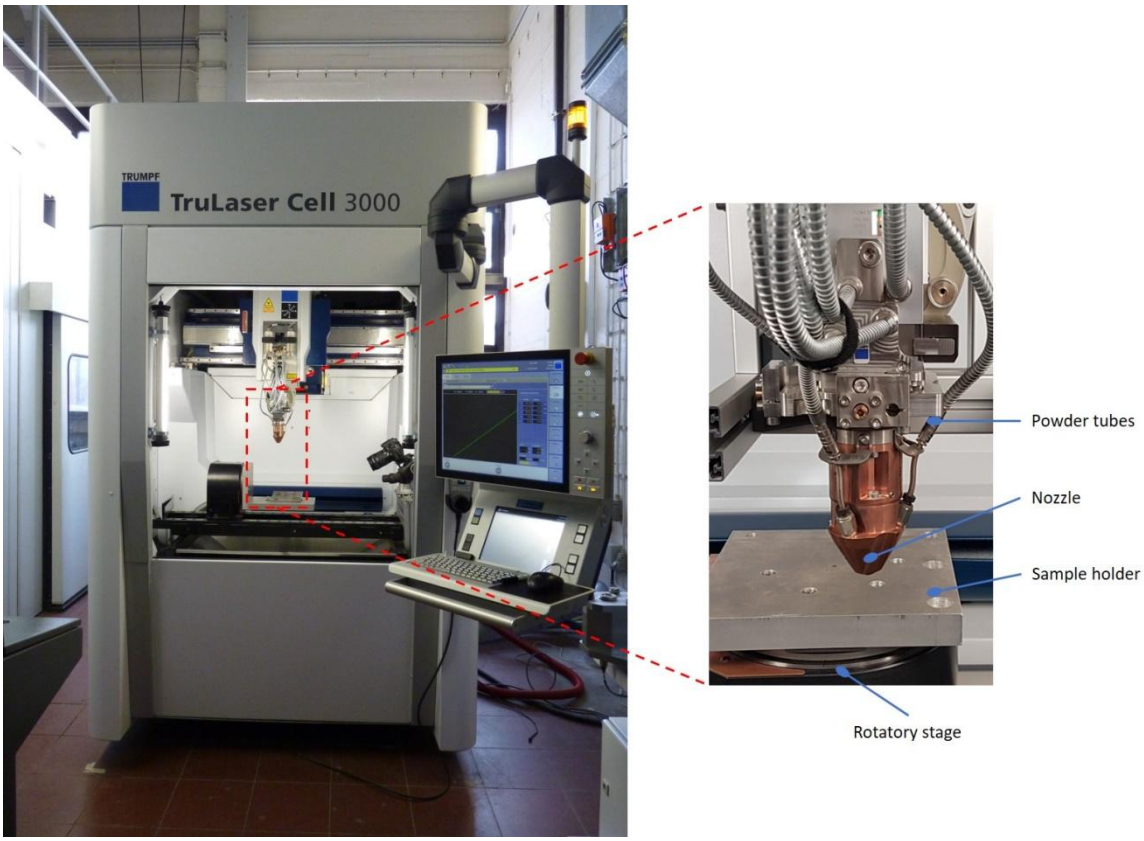


***Figure 11*** *– Photograph of the TruLaser Cell AM set-up. Right: detail of the laser head, with laser and powder nozzle integrated, hovering on the rotatory stage.*

The powder is delivered by a Medicoat Flowmotion Twin powder deliverer through three nozzles integrated into the laser head. The nozzle exits are arranged at 120° angle with respect to each other around the laser output. This laser head is set at a fixed distance of 16 mm above the substrate and is equipped with a collimation unit able to change the laser focusing distance. The powder is delivered from the nozzles and focused on a spot of approximately 3.5 mm in diameter. The printing set-up is shown in Figure 11. The substrate plate and powder used in the experiments are both made of stainless steel 316L, a common type of steel with high concentrations of Cr and Ni and low concentrations of Si and S (see Table 4). Different batches of powders have been used with different grain distributions, but the average diameter of a grain stayed always between 50

and 100 µm. The machine is operated through proprietary software loaded on an embedded computer.

***Table 4*** *– Composition of base plate and feedstock powder.*

| | Elements in wt. % | | | | | | | | | |
|---|---|---|---|---|---|---|---|---|---|---|
| | C | Si | Mn | P | S | Cr | Mo | Ni | N | Fe |
| Base plate | 0.016 | 0.46 | 1.26 | 0.032 | 0.001 | 16.9 | 2.05 | 10.1 | 0.05 | Bal. |
| Powder | 0.01 | 2.1 | 0.5 | 0.02 | - | 16.9 | 3 | 12 | 0.07 | Bal. |

The optical set-up is attached to the laser head and permanently focused onto the same spot below the laser head to record emission from the molten pool. The optical system is composed of two fused silica lenses, filters and optical fiber that sends the light from the molten pool to one of two spectrometers, connected to a laptop. The focal lengths of the lenses are 17.5 cm and 5 cm, correspondingly; they focus the light into an optical fiber with a 600 µm inner diameter and a 400 – 2100 nm transmittance window. The same assembly holding the lenses can host neutral density or long pass filters needed in experiments. The light is recorded by two portable spectrometers produced by Ocean Insight (Florida, USA), one recording in the UV-Vis from 180 nm to 890 nm with a 2048 pixels detector, and the other in the near IR range from 900 to 1650 nm with a 128 pixels detector. Light collected into the second spectrometer is always filtered through a 1060 nm long pass filter that blocks from the light the first 13 pixels on the detector in order to avoid detection of the laser line. The spectrometers are driven either by the OceanView software (Ocean Insight, USA) or a custom code written in Matlab®.

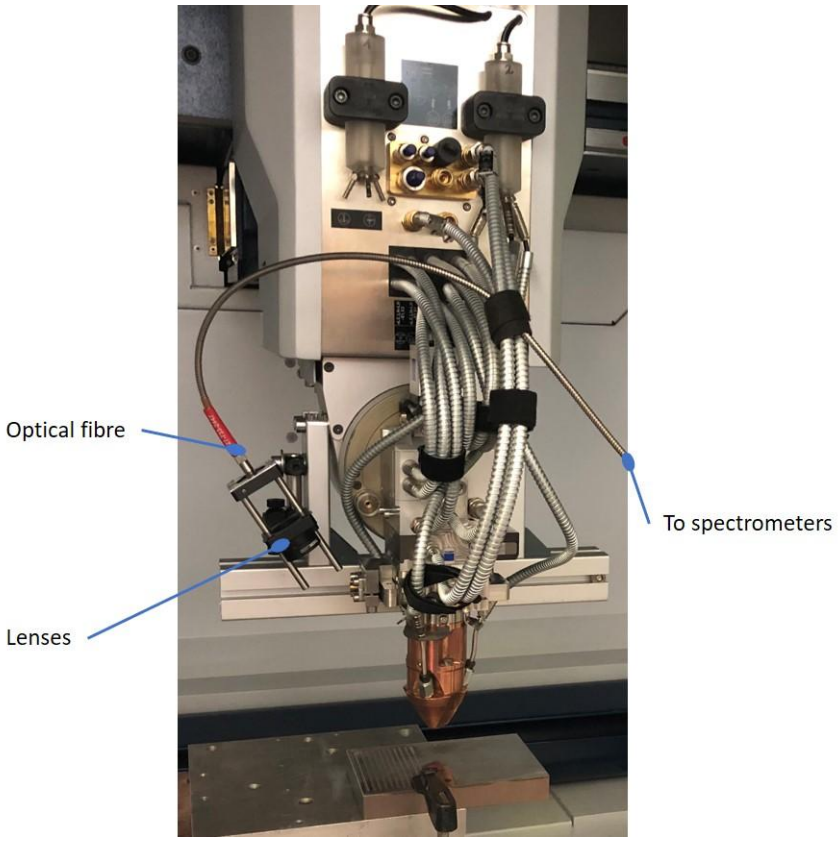


*Figure 12 – Laser head with optical set-up.*

Main deposition parameters are laser power, speed and spot diameter and powder mass flow. The goal for a DED process is to maximize rate deposition while keeping the printed item free from unwanted features, and this is made possible by an accurate selection of processing parameters. For the machine employed in this work, a parameter study is performed allowing the selection of optimal setting for a quality deposition. The requirements for this study were:

a. A low dilution, defined as ratio between the track area in contact with the base plate and the melted substrate area. This needs to be lower than 20% but nonzero.
b. An aspect ratio, ratio between track height and width, approximately of 1/3.

Also, the overlapping between consecutive scans is accounted for. The final standard parameters used to print test samples result after a compromise between these aspects. The parameters are listed in Table 5.

*Table 5 - Printing parameters of choice for the specific combination of printer settings and feedstock material.*

| | Laser power, W | Laser speed, mm/sec | Powder flow, g/min | Laser spot diameter, mm | Energy density, J/mm$^2$ |
|---|---|---|---|---|---|
| Set 1 | 1200 | 21.6 | 17 | 2.4 | 23.1 |
| Set 2 | 800 | 13.3 | 15 | 1.6 | 37.5 |

Under the chosen set of parameters, metal stripes are printed on a plate surface with a length of 6 - 8 cm. The parameters of the printer are controlled by a user via the printer-embedded computer whereas the parameters of the spectrometer such as the integration time and length of acquisition are user-controlled from the external laptop. The spectrometer starts recording slightly before the laser is turned on and ends recording slightly after the printing scan is over. Both the spectrometers can record a maximum of 300 spectra per second with the shortest integration time of 1 ms. Spectra recorded when the laser is off are discarded in further processing.

## 3.2 Molten pool emission

### 3.2.1 Plasma and continuous emission

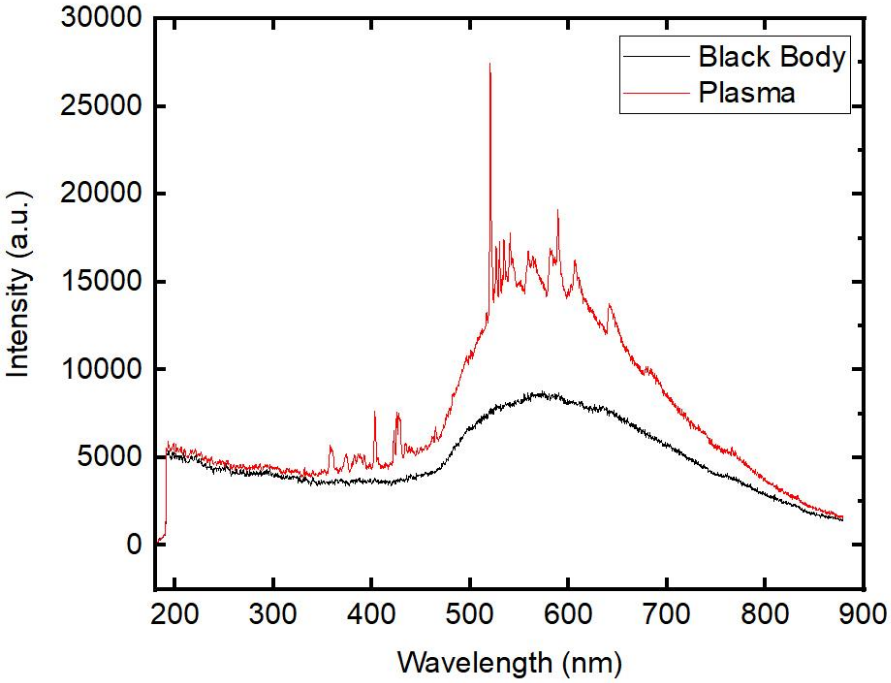


***Figure 13*** *– Two different type of emission from the molten pool, thermal and thermal + plasma.*

The emission recorded from the molten pool can be of two types. The first is a broadband thermal emission with no distinct spectral features coming from the molten steel right below the laser outlet. The intensity of this emission is related to the temperature of the molten steel. The second type of emission is a sum of thermal and discrete emission from a plasma that is occasionally created above the steel molten pool if the laser power is sufficiently high for plasma breakdown. Plasma is a state of matter formed by ground state and excited ions and atoms and electrons. It emits continuous radiation due to the Bremsstrahlung process and discrete spectrum due spontaneous relaxation of plasma species to lower energy states. The upper trace in Figure 13 shows the plasma spectrum. Peaks of chromium and iron are seen between the wavelengths of 300 and 600 nm; the

low resolution of the UV-Vis spectrometer prevents the identification of every emission peak. The lifetime of the laser induced plasma is shorter than 100 μs and the spectrometer integration time is 1 ms at its minimum. During the integration time, the spectrometer always records steel thermal emission plus a random (sporadic) plasma event. Under settings of the printer shown in Table 5, plasma ignition is a rare and unpredictable random event; therefore, for monitoring the printing process plasma spectra are discarded thus relying on only thermal emission spectra.

Thermal spectra can provide a limited amount of information regarding the ongoing process. A typical approach is to reduce the dimensionality of a spectrum to a single number that may better represent the source of light at a specific moment of time. Several metrics are used in this work to extract information from spectra; the first and most important one is the integral emitted intensity.

### 3.2.2 Set-up characterization

Optical spectroscopy allows to detect emission from the molten pool and assess its stability that is important for quality printing. For a first experiment, emission is detected in the UV-Visible range when printing with set 2 of parameters in Table 5. Three separate ridges are made by three single-layer printing scans on top of a steel plate. Spectra recorded during these scans are then processed to calculate the integral emission intensity for each spectrometer readout. Before doing that, the spectra are corrected to account for the spectrometer response function and attenuation of the neutral density filters. The spectra are integrated over the wavelength range using the trapezoidal method. The results show a stable emission, with an average integrated intensity of $2*10^{-7}$ and a standard deviation

of approximately 19 % for the three printing scans. This value is influenced by fluctuations in the energy density (see equation 2.1) and the rate of powder supply; both factors affect the molten pool behavior. When scanning the laser head across the same plate three times with the same set of parameters but without powder flow, the average integral intensity has a value of $1.47*10^{-7}$, with a mean standard deviation over the three scans of 15%. This shows that feeding powder to the molten pool increases emitted light and noise. Moreover, using a parameter like the energy density to describe a deposition may not be sufficient, since it does not include the powder mass flow, that clearly affects the molten pool emission.

The optical set-up for monitoring the printing process is not a part of the printer; it is mounted on the laser head when necessary. The optical alignment is performed anew at every mount. Since this process may introduce errors, an experiment is performed to assess its reliability. With the Set 1 of parameters in Table 5, three stripes (ridges) are printed, each made of three overlapping layers, and the light is collected and recorded with the infrared spectrometer. Between printing one stripe and the following, the machine is stopped, and the optical set-up is unmounted and mounted again. The reproducibility is established by comparing the processed emission spectra, and the results are displayed in Figure 14.

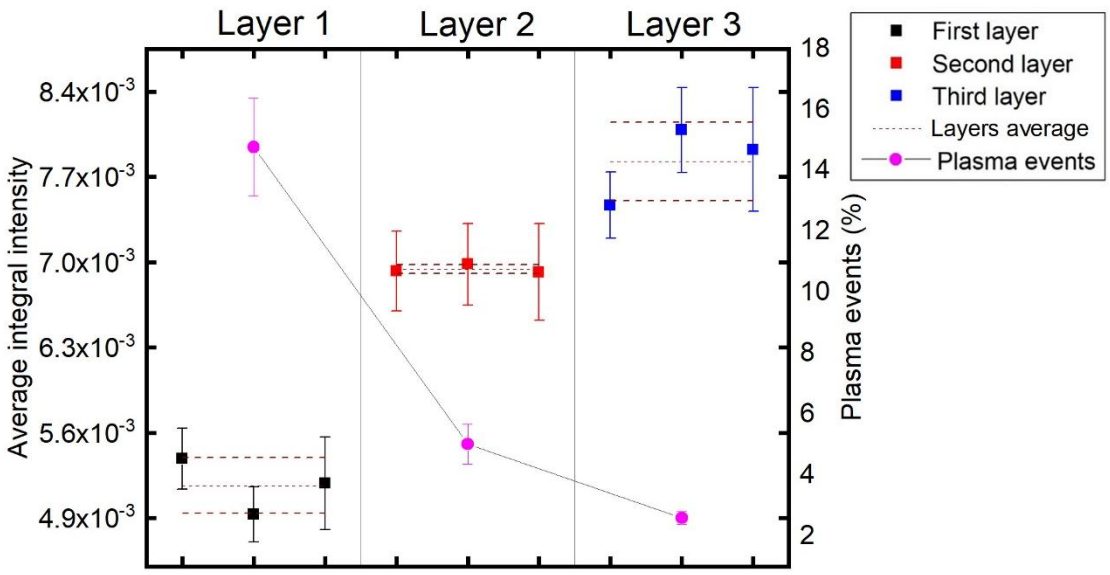


***Figure 14*** *- Comparison between metrics calculated processing the emission recorded in IR while repeating the same print three times. Black, red and blue squares: average integral intensity of the emission in different moments while printing three times a three-layer stripe, dotted lines: averaged emission on the same layer, with standard deviation of the mean (left), purple circles: plasma events randomly recorded while monitoring the molten pool (right).*

During the deposition of every layer, several hundred spectra are recorded, which are then processed in order to calculate the integral intensity. The average integral intensities for single layers and groups of three overlaid layers are plotted in Figure 14. The intensity recorded during the three repetitions of this experiment is always the same within one standard deviation interval, meaning that both the process and the optical set-up used to probe it are reliable and provide reproducible data. The exact placement of the optical assembly could change from experiment to experiment, but this was not a problem since what was important is to understand how the molten pool emission changes when changing key parameters or process features within the single experiment.

Another interesting result from the same experiment is related to how the light emitted by the molten pool changes with stacking layers while building a bulk item. The longer the printing time the hotter the printed bulk becomes, thus leading to a hotter and brighter molten pool. Also, as was mentioned, the molten

pool emission is thermal and may combine with discrete emission from rare occasional plasma. It is possible to count all the plasma spectra recorded during experiment and the result is shown in figure 14 reported as the percentage of the plasma events with respect to the total number of spectra recorded. The number of plasma events clearly decreases with the number of stacked layers.

### 3.2.3 Temperature calculation

The light recorded by the spectrometer has a slight different shape to the one emitted by the light source, due to the instrumental response, so in order to retrieve the original emission, the spectrometer is calibrated in terms of spectral dispersion and intensity response [170]. The wavelength calibration is performed with a mercury lamp. An intensity calibration can be more difficult since light sources with a stable and certified emitted intensity are expensive and require extensive maintenance across the years. This calibration can be relative or absolute. The former type considers the spectral sensitivity of the optical system across the available wavelengths, providing the response curve of the detector. The latter additionally provides a way to convert a fixed and known number of photons with certain energy travelling through a predetermined solid angle toward the detection system, into a recorded spectra that serves as a calibration and conversion curve for future acquisition. With this conversion curve the user can go back to the source real emission, measured in $W \cdot m^{-2} \cdot nm^{-1} \cdot sr^{-1}$.

When recording thermal emission from a hot body, like when monitoring molten steel during metal additive manufacturing, it is possible to compare the spectrum to the shape of the Plank blackbody function. The emission curve described by the Plank function shows that as the body temperature arises, the integral

emission intensity increases and the wavelength of the emission maximum shifts to shorter values. The real-world bodies are always grey bodies, meaning they emit only a fraction of light when compared to a black body, and this fraction is called emissivity. Emissivity $\varepsilon$ is a number between 0 and 1 (only a true blackbody has $\varepsilon$=1) and is incorporated into the Plank equation:

$$I_\lambda(\lambda, T) = \varepsilon \frac{2hc^2}{\lambda^5} \frac{1}{e^{\frac{hc}{\lambda k_B T}} - 1} \qquad [3.1]$$

Where $k_B$ is the Boltzmann constant, h is the Plank constant, c is the speed of light, $\varepsilon$ is the emissivity and $\lambda$ is the radiation wavelength. It is possible to fit a recorded spectrum with this equation and extract the temperature value that gives the best fit upon iterations. To do that, the material emissivity must be known in advance. The exact knowledge of emissivity can be a problem, since it varies with the material temperature, surface oxidation, etc.

This procedure can be applied while monitoring the emission from steel melt pool during metal additive manufacturing. Specifically in this context, a modified version of the Plank equation has been used, where instead of emissivity $\varepsilon$, a factor D has been used, called scale factor. This value is iterated during the fitting process together with the temperature. This factor includes several variables like the unknown emissivity and others that may alter the light collection efficiency. The spectrometers are intensity-calibrated in relative units, so they return the real emission profile of the light source but with intensity information lost. It is still possible to calculate the temperature fitting the spectrum with the two-parametric Plank equation.

In Figure 15 a processed spectrum and relative fit are reported, alongside with the resulting calculated temperature of 2188 K. The recorded spectrum is at first

subtracted of the instrumental noise and then multiplied with spectrometer calibration coefficient, and only then fitted with Plank equation via custom software written in Matlab. The optical set-up records emission from a finite area on the molten pool surface. This surface is not uniform, it does not have a constant temperature and it is not stable. Its upper surface is constantly in motion during the scan. This means that the light recorded is an average of the thermal emission from several points at different temperatures and in motion for the duration of the spectrometer integration cycle.

Considering this and other technical difficulties, it follows that the value resulting from the fitting can be unprecise. While this procedure is explained and shown with respect to data recorded in the near IR range, everything applies as well to the visible range.

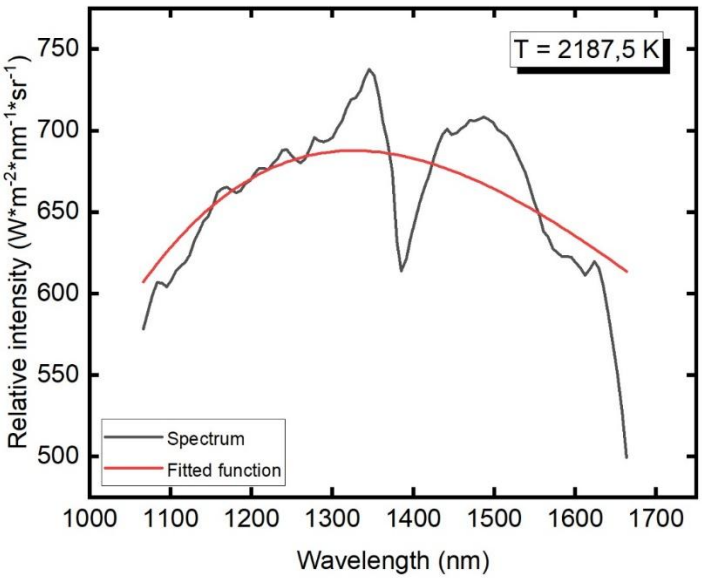


***Figure 15*** *- Spectrum recorded in the IR region, processed and fitted with the Plank function, which in this case resulted in a temperature T=2187,5 K*

This blackbody fitting procedure was applied to the data underlying those shown in Figure 14. The calculated temperatures for the three layers and respective averages are reported in Figure 16.

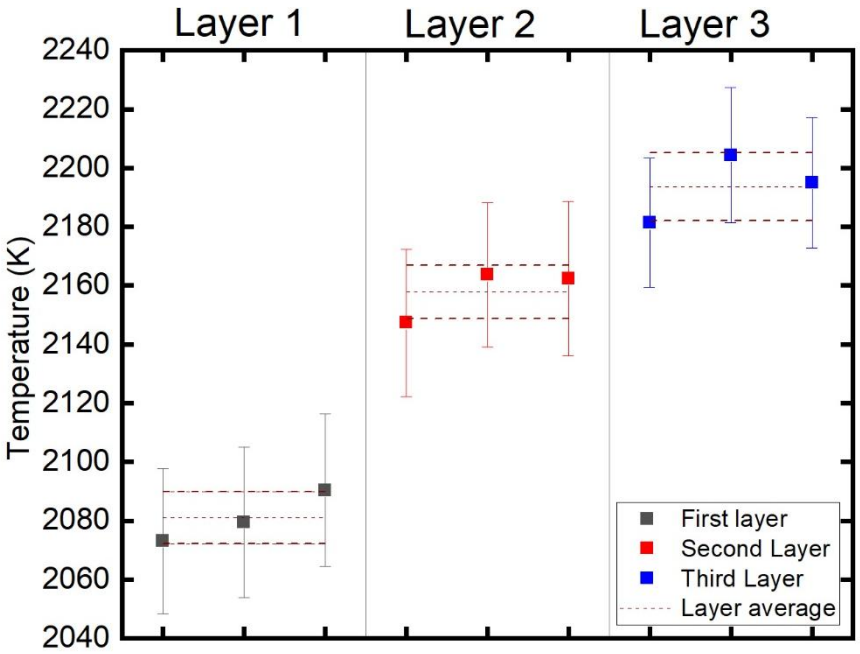


***Figure 16*** *- Temperature calculated while printing three times a three-layer wall. Dotted lines: layer averages and error ranges.*

These results validate the previous finding that the average values are reproducible within each scan group and change between the groups, exactly like the emitted intensity. This is not surprising, since emitted intensity and temperature are interrelated and it is expected that when printing a multilayer bulk item, the matrix accumulates energy, and its temperature builds up with time.

Since the optical set-up and the printing laser are not synchronized, when the laser is turned off at the end of the deposition process, the light emitted by the cooling steel is recorded. The steel immediately begins to solidify, which reflects

on the measured temperature and intensity that both reach a plateau, as seen in Figure 17.

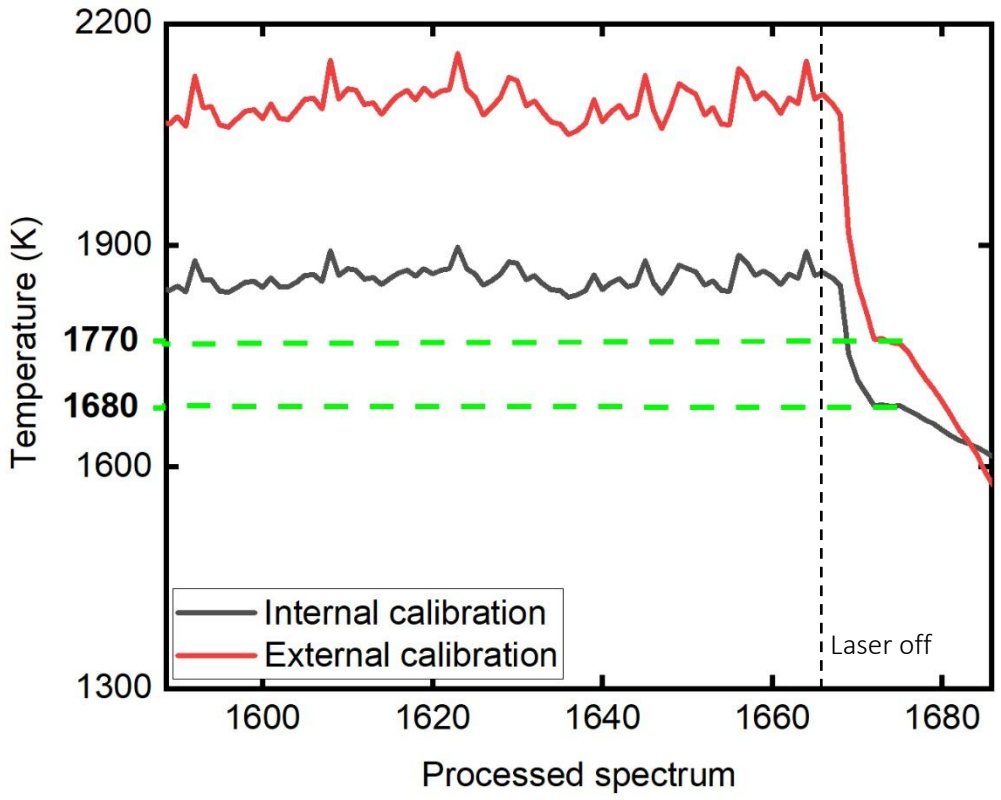


***Figure 17*** *- Temperature calculated on AM emission using spectrometer response coefficient (red) or using plateau emission as internal standard (black).*

Solid-liquid phase transition for steel 316 happens at approximately 1650 Kelvin, so the emission recorded after the laser is turned off can be used as a reference to calculate the temperature from the other recorded spectra. A ratio between the Plank function calculated at 1650 Kelvin and the emission spectrum during phase transition is used as correction coefficient for the temperature calculation process instead of the spectrometer calibration coefficients. The results for one of the test runs are displayed in Figure 18. The calculated temperatures obtained with this correction method are lower than the previous ones obtained with the

standard-lamp-calibrated spectrometer. Similar results obtained with the same set-up has been reported in the literature [39].

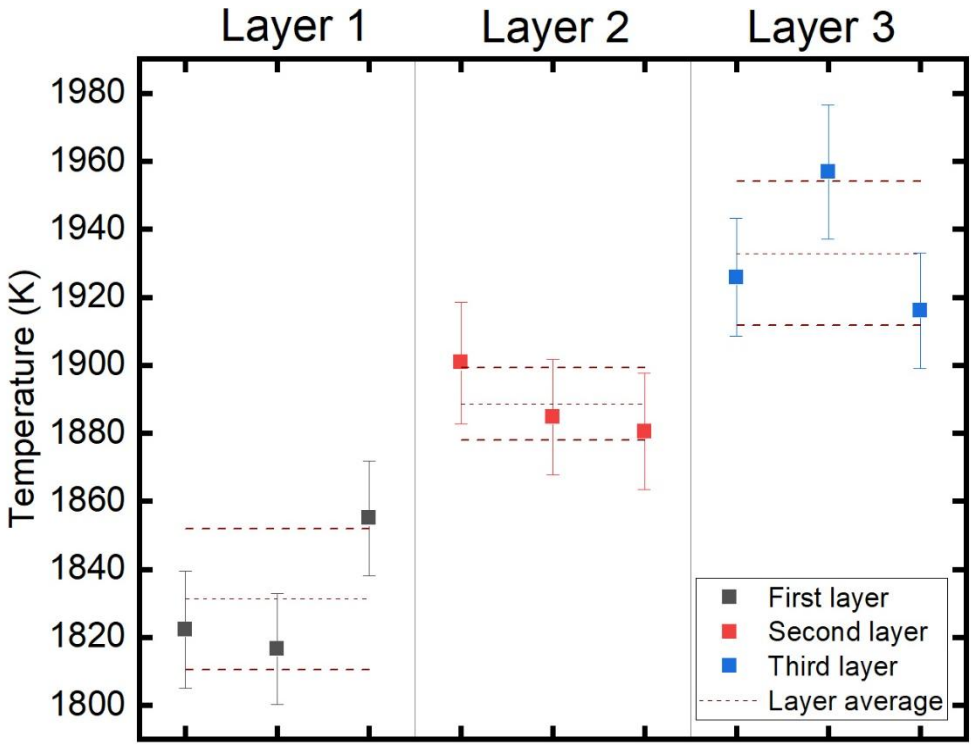


*Figure 18 - Temperature calculated using emission from a cooling down plateau as response coefficient, while printing three times a three-layer wall. Dotted lines: layer averages and error ranges.*

The lower value for the temperature obtained with one-point (external) calibration method appears closer to the real one, especially when compared with other thermometric techniques. The added value of this method is that it does not use any measurement or calibration besides the monitoring of the AM process. This correction coefficient is calculated with the very same set-up used for monitoring, meaning it automatically considers the transmittance of the optical elements, air absorption, etc. while external calibration of the spectrometer requires an additional measurement with a standard calibration lamp. The downside of it is that recording these spectra does not happen always but depends on the laser head route and sampling rate, and the selection of

specific spectra (i.e., those corresponding to the solidification plateau) must be done manually. Furthermore, recording the emission from the cooling steel is more probable in the infrared region, where sits the peak of the Plank function for the considered temperature.

Temperature calculation using the plateau emission as the calibration reference for the spectrometer is repeated with the same 3 x 3-layer piece and the results are reported in Figure 18. These values agree with the results obtained with the external calibration; the calculated average temperatures are consistently lower by approximately 250 Kelvins for all the three printed ridges (compare Fig.18 with Fig.16), while the standard deviations for single runs stay within 1% of the average SRD value regardless of what method of calibration was chosen.

The calibration with an external standard lamp is performed with a different optical set-up overall, while the one-point calibration is obtained with the same set-up, acting as internal standard. For this reason, the results achieved with the latter method are considered more precise, so it is the method of choice for following measurements, at least when applicable, even if it requires longer data processing time.

## 3.3 Process characterization

The deposition process is the result of many varying factors, like laser power and scan speed, as mentioned in the previous chapter. However, describing the deposition using a full set of process parameters can be inconvenient, especially when comparing results obtained with different printers. In order to reduce the number of variables involved, parameters ratios are used to compare different machines, for instance the energy density mentioned above. In the following

experiments the goodness of this parameter is tested by printing several test coupons with different laser power and scan speeds that resulted in different energy densities, comparing the resulting emission from the molten pool.

For a first experiment 5 test stripes are printed, a standard one with set 1 processing parameters (Table 5), two with lower and higher laser powers 1000 W and 1400 W respectively and scan speed of 21.6 mm/s, and two with the laser power of 1200 W and slower and faster scan speeds of 16.7 mm/sec and 26.7 mm/sec. The emission is recorded in the IR region and the temperature and integral intensity are calculated using one-point calibration method. The Results are displayed in Figure 19.

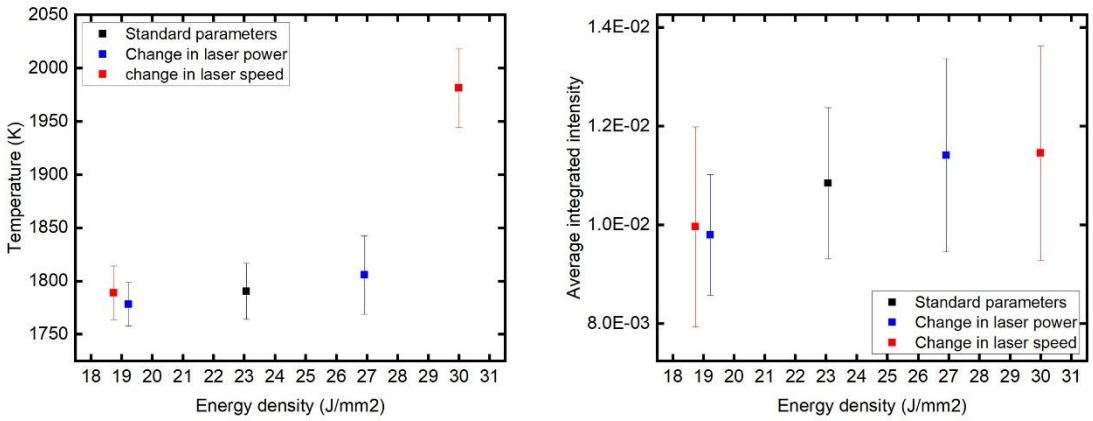


*Figure 19 - Temperature (left) and average integral intensity (right) calculated by spectra recorded in the IR range and emitted during different depositions characterized by diverse energy densities.*

The results show a limited influence of the change in energy density on the metrics analyzed. The errors associated with the average results are too high to ensure a clear trend, but they both increase in their averages in what seems to be a linear fashion. The fact that the emission does not change considerably may hint that a limited change in processing parameters produces a similarly stable molten

pool. Alternatively, this change in processing parameters may leave the molten pool temperature and emission almost unaffected, while still having an influence on the final deposition, for instance with a deeper welded track or a more efficient powder inclusion due to pre-heating the powder on the laser optical path.

These are preliminary findings, and further studies are needed to assess how optical spectroscopy can monitor the molten pool changes due to a change in processing parameters.

A further experiment aims to show how the molten pool behaves while printing a bigger structure. With set 1 parameters in Table 5, 5 walls made by 10 overlapping layers are printed with a 10 s waiting time between consecutive layers. The emission is recorded in the IR region and the temperature is calculated with one-point method. The results are shown in Figure 20.

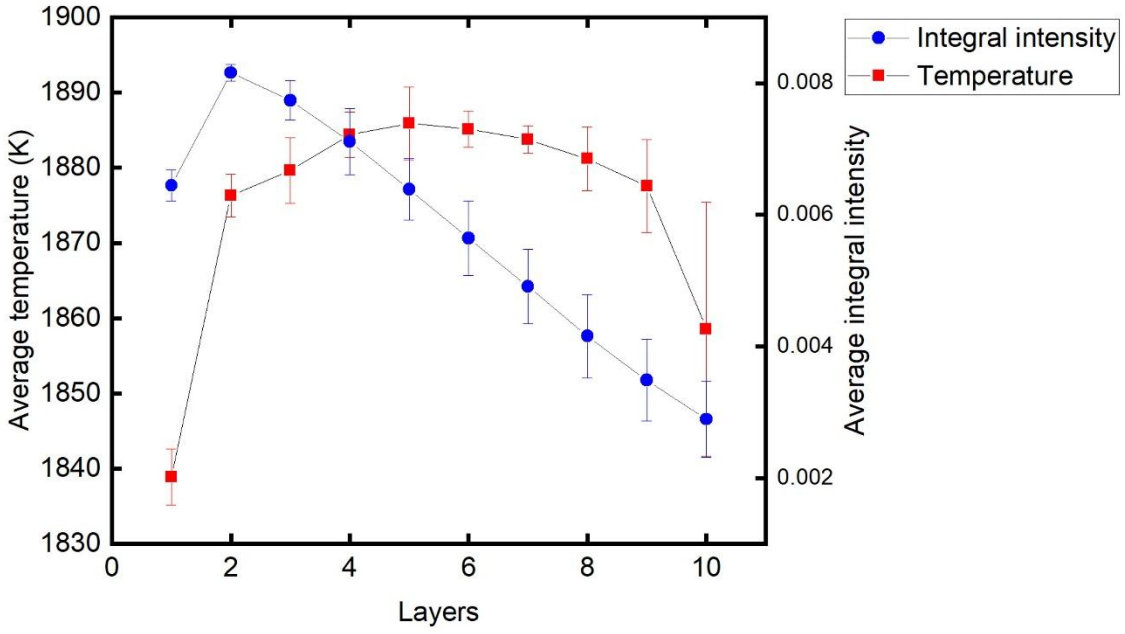


*Figure 20 - Temperature (red squares, left axis) and average integral intensity (blue dots, right axis) calculated from emission recorded in the IR region while printing 10-layer walls.*

The processing parameters remain constant throughout the whole deposition, nonetheless the temperature and emitted intensity change. The temperature initially increases, then reaches a plateau and then drops. This is probably because the surface of the printed wall becomes larger as the number of layers increases and dissipates heat at a rate first lower, then equal, and then higher than the rate of heat supply.

The emitted intensity has a decreasing trend from the third layer onward, but the reason for this is unclear. The optical assembly is rigidly mounted on the laser head, so it is reasonable to assume that the acquisition geometry does not change during the build-up. During other experiments performed under similar conditions with the same set-up, the authors recorded an increased amount of oxides and a bigger area of the molten pool [171], and since oxides have a higher emissivity than liquid steel, this should lead to higher emitted intensity. For thermocapillary effect, the oxides are pushed away from the central region of the molten pool toward its external boundaries, where they solidify [137]. Since the optical set-up is focused below the laser outlet approximately at the center of the molten pool, it is not expected for the emitted light to be influenced by the presence of oxides. On the other hand, the constant temperature due to a phase transition recorded after the laser is turned off is on average higher with every next layer (not shown), and this should be a consequence of the print being richer in oxides.

Another unclear result regards the plasma events, which are not reproducible. Out of the five deposited samples, for three of them the number of plasma events increases with the printed layers, while for the other two, this number decreases and approaches zero starting from the fifth layer onward.

It follows from these results that the emission from the molten pool is influenced by several printer parameters; some, like the laser power are considered in literature, others, like the printing path and increase in deposited volume, are overlooked. The emission does not provide much information about limited change of energy in input, but can be used to monitor the growth of the printed item. Overall, the goal of metal additive manufacturing is to create items with reliable thermomechanical properties. If and how this relates to the molten pool optical emission is a subject of further investigation that can be accomplished with a portable optical sensor that can be installed on different types of metal printers. Once the connection between the optical emission and the deposition properties is established, monitoring online can provide a useful resource to improve the process through a closed-feedback loop control, a system that uses a signal from a sensor to adapt the device properties on the fly with no input from an external user. Such systems are already studied [123, 172] and can be the future of metal additive manufacturing online control.

# 4 Fault monitoring

Up to now optical spectroscopy has been used to link the emission from the molten pool with the deposition parameters. But one of the greatest needs of additive manufacturing is in the development of a sensor able to detect the formation of a defect within the printed item on-line and in real time. A great obstacle in defect monitoring is a stochastic nature of the defect formation and impossibility to create a prescribed defect for calibrating a sensor. In this chapter, a test print is performed on a substrate that is previously modified by carving on its surface grooves and holes. This sample acts as a standard with a series of

reproducible defects for testing the optical sensor. Several metrics are calculated from the emitted spectra to evaluate the sensor performance. A simplified thermal model has been created to simulate this experiment, and since simulation and experiment are in agreement, it is possible to foresee which optical signals arise from different defect geometries.

## 4.1 Metrics

The optical set-up shown in Figure 12 has been used to record light from a surface with artificial defects during the printing. The goal is to evaluate if and to which extent optical emission spectroscopy (OES) can be used as an online monitoring technique. A print on a defect-free surface provides a smooth optical signal whereas the presence of a defect makes the signal deviate from its average value. This can be sensitively detected by appropriate metrics. The metrics are the temperature, spectrum-integrated emission intensity, and the correlation coefficient between the spectrum recorded online and a reference spectrum stored in a library. The reference spectrum is the averaged emission spectrum from a deposition with no known defects that is compared to the on-line recorded spectra using the formula:

$$r = \frac{\sum(x_i - \bar{x})\,(y_i - \bar{y})}{\sqrt{\sum(x_i - \bar{x})^2 \sum(y_i - \bar{y})^2}} \qquad [4.1]$$

where $x_i$ and $y_i$ are the intensities of sample and reference spectra respectively and $\bar{x}$ and $\bar{y}$ are their averages. The correlation coefficient is a general measure of the linear relation between two distributions [173], its values span the range -1,+1. The values close to 1 or -1 correspond to strong positive or negative

correlations between datasets whereas values close to zero correspond to uncorrelated datasets.

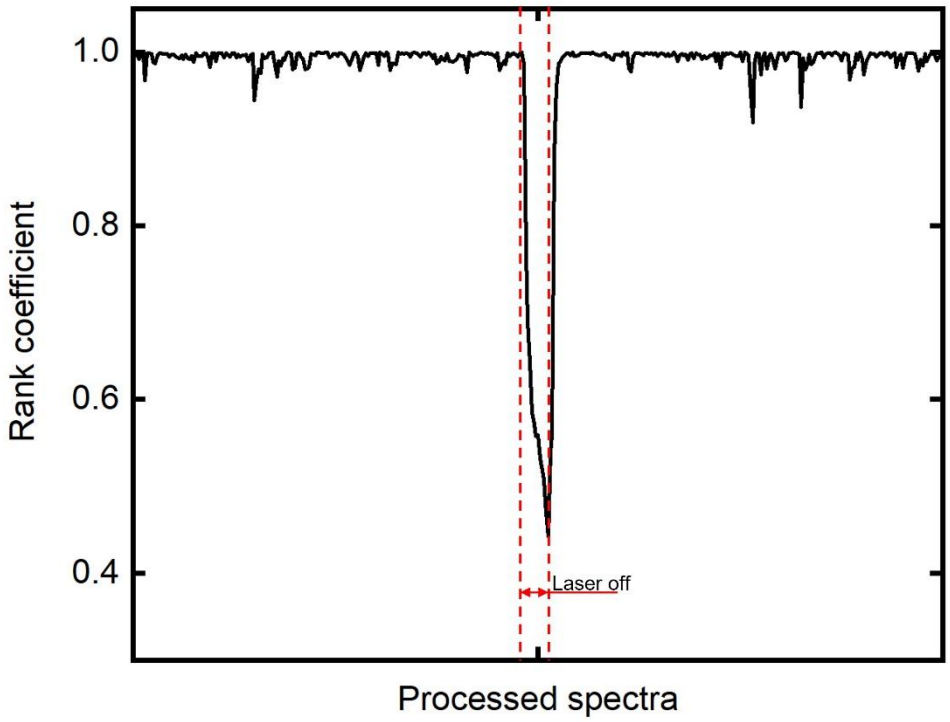


***Figure 21*** *- Detail of the rank correlation coefficient calculated from emitted spectra recorded while introducing an artificial defect into a deposition.*

With this general formulation two coefficients have been calculated; the Pearson correlation coefficient, when the formula was applied directly to the raw spectrum, and the rank correlation coefficient, when the spectral intensities were priorly ranked. When applied to spectra obtained during printing on a defect-free surface, both coefficients are equal to 0.97 ± 0.03 meaning the shape of emission spectra is highly consistent.

This metric was tested experimentally. Three lines are printed with Set 1 experimental parameters shown in Table 2 in chapter 3 and light is recorded in the IR region. An error is introduced by shutting down the laser for 5 millimeter in the middle of a 8 cm deposition line. This event could be easily detected by

processing the spectral data; it caused a deep depression in the value of the rank coefficient displayed in Figure 21. The other two metrics tested integral intensity and temperature, exhibited different behavior; the signals corresponding to the depression minima are comparatively shown in Table 6.

***Table 6*** *- Signal linked to an artificial defect introduced during a deposition, expressed as a minimum in the metrics normalized intensity, temperature and Pearson and rank correlation coefficient. SBR: Signal to background ratio.*

| | Integral intensity (normalized) | SBR | Temperature (K) | SBR | Pearson coefficient | SBR | Rank coefficient | SBR |
|---|---|---|---|---|---|---|---|---|
| Laser off | 0.246±0.017 | 15.141 | 1720±1 | 9.7 | 0.559±0.001 | 57.644 | 0.455±0.003 | 61.876 |

All the metrics show a drop in correspondence of the known error, the signal is then considered to be the magnitude of this drop, calculated as the difference between the lowest point in the closest vicinity of the area of interest and the mean value of the background. These numbers are averaged for the three runs to have a mean value and a standard deviation. The background value is calculated by averaging three arbitrary datapoints obtained from the smooth part of the print. A defect is considered detected if the signal peculiarity is at least three times the standard deviation of the background. The signal-to-background ratio (SBR) is the average signal minus the standard deviation divided by the background standard deviation. As follows from Table 6, all three metrics could detect the interruption event with the correlation coefficients showing the best signal to noise ratio. This suggests that the correlation coefficient is, perhaps, the

most sensitive metric for monitoring any form of variations in the recorded emission signal caused by a faulty deposition.

## 4.2 Modified steel plate

The technique in use is clearly able to detect whether the optical signal is off an average, thus tracing a defect during the deposition. In the next step, we study the reliability of the defect detection and determine a minimal size of the detectable defect. There are many defects typical of metal laser deposition that can alter the molten pool emission. They happen randomly during the printing and there is no way to control their size and shape or choose a certain type of defect as a standard one. It is, therefore, reasonable to artificially modify the printing environment and introduce reproducible defects with known shapes [96]. This idea is exploited in an experiment aimed at determining the minimal defect size that can be discerned by the optical set-up used as a monitoring sensor. To do that, a steel plate is carved with two types of geometrical shapes, trenches and holes, all 1 mm deep but with different width, as reported in Table 7.

***Table 7*** *- Dimensions and order of grooves (G) and holes (H) carved on substrate surface.*

| Defect type | T1 | T2 | T3 | T4 | H1 | H2 | H3 | H4 |
|---|---|---|---|---|---|---|---|---|
| Width/diameter, mm | 2.0 | 1.0 | 0.6 | 0.3 | 1.2 | 1.0 | 0.6 | 0.3 |
| Depth, mm | 1.0 | 1.0 | 1.0 | 1.0 | 1.0 | 1.0 | 1.0 | 1.0 |

The four grooves are carved across the whole plate width, while the four holes are repeated in six parallel rows. To study the effect of this artificial non uniformity, three walls of ten consecutive deposition layers are printed on the top

of the defective plate, crossing first the grooves and then the holes, always in the direction from biggest to smallest. The laser head returns to a starting point at the end of every deposited layer and immediately starts printing the next one. The walls are 145 mm long and the printing lasts 220 seconds per single wall. The machine uses Set 1 as the processing parameters from table 2 and the light is recorded in the visible range slightly attenuated by two neutral density filters with OD 0.5 and 0.6 to prevent detector saturation. The spectrometer runs independently of the processing laser; to include spatial information into the data, the spectrometer is handled by custom software written in Matlab® that couples every dataset with a timestamp. The recording starts before the deposition begins and ends after the deposition finishes; the first spectrum showing the presence of the emission light is taken as a starting point. Since the laser speed is known, it is possible to link every spectrum to a position on the substrate.

### 4.1.1 Results and discussion

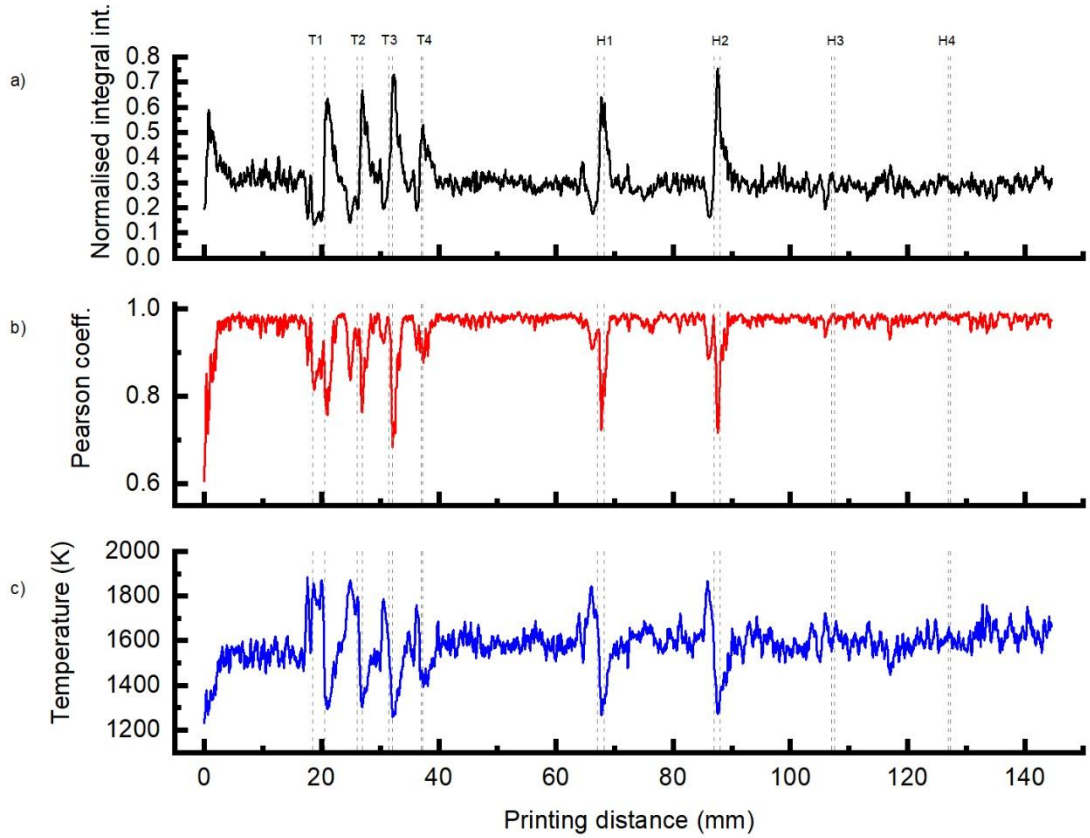


***Figure 22*** *– a) Normalized integral intensity, b) Pearson and c) temperature as calculated from emitted spectra coming from depositing a layer on top of a steel substrate, modified with trenches and holes, with dimensions specified in Table 2. The defects are shown with the dotted lines and labelled on top of the figure, while data lines are smoothed with a 3-points moving average.*

Figure 22 shows the metrics calculated from the emission spectrum obtained during the deposition of the first layer of the first wall; the dashed lines show the position of the defects. All the metrics exhibit strong deviation relative to the average values when the laser scans across the four grooves and the first two holes with diameters of 1.2 and 1 mm respectively. There is no visible variation when the laser head goes over the two smallest holes with diameters of 0.6 and 0.3 mm.

The molten pool emission spectrum depends on several competing factors, like the pool temperature and composition and geometry of the substrate. Also, it depends on the energy input from the laser, thermal dissipation, rate of powder supply etc. The emission spectrum collected while printing over a smooth surface is stable; the standard deviation is below 10%, for all considered metrics. When printing over an artificial defect the temperature of the molten pool changes, affecting its emission. In this regard, these artificial defects may resemble spontaneous ones, like gas inclusions, surface contaminations, and fractional vaporization which affect the molten pool internal energy. The artificial trenches and holes carved on the substrate surface can be seen as exaggerated versions of surface defects, like pores, cracks, and lack of fusion. The resulting signals are typically wider than the correspondent defects (Fig. 22). The change in the emission signal coming from the defective surface is caused by a change in the rate of heat diffusion and possible geometrical effects [174].

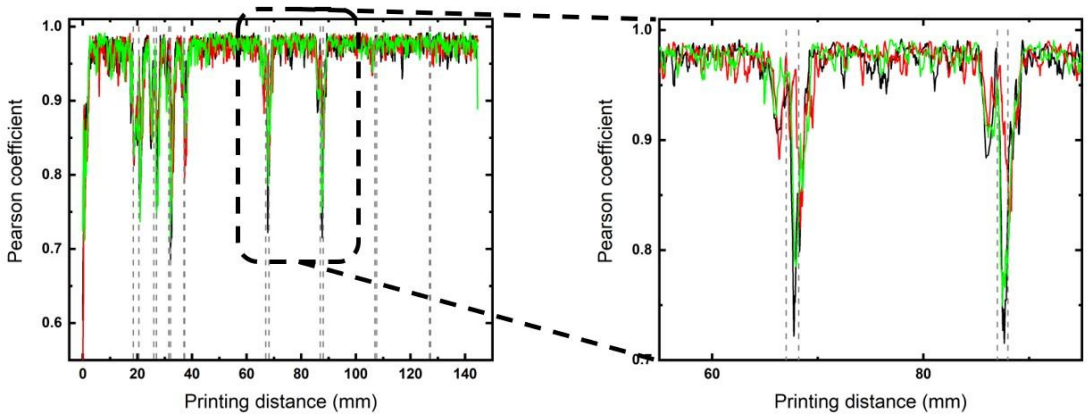


***Figure 23*** *- Pearson correlation coefficient calculated after printing on modified steel substrate, three traces corresponding to first layers of the three printed walls. Right: zoom on signals from two largest holes.*

To ensure the repeatability of the experiment, three ten-layer walls are deposited on top of the same substrate. The Pearson correlation coefficient related to the first deposited layer of the three walls is displayed in Figure 23.

It is evident from the figure that the three runs produce reproducible spectra. A signal from a defect is processed considering the highest integral intensity or peak temperature, or the lowest correlation coefficient in the vicinity of a defect, all subtracted of their respective background values and averaged for the three runs. The background is calculated using three random values taken from a smooth part of the substrate.

The signal-to-background ratio (SBR) is then calculated averaging these signals, subtracting their standard deviation and dividing them by the standard deviation of the background. The results for all the metrics are provided in Table 8. The signals from the defects are constantly above the three-sigma level. The relative errors are mostly below 20% with the temperature metric being the least sensitive in this regard. The correlation coefficient has the highest signal-to-background values, which are two-three times higher than other metrics. This implies that the correlation coefficient is the most sensitive metric for the detection of surface defects.

A spatial resolution of the defect detection with the help of the optical set-up is determined by the size of the smallest defect detectable. The results show that it is possible to detect holes of 1 mm in diameter using any of the three metrics, while no metric seems to provide information on smaller defects. Therefore, the smallest defect detectable by the given technique is about 1 mm. Grooves are not used for establishing a minimum defect size since their size is limited only in one, transversal direction.

*Table 8 - Signal from the metrics temperature, normalized integral intensity and Pearson coefficients collected in correspondence of the artificial defects. Bottom row: same but calculated from a smooth print. SBR: signal to background ratio.*

| | Diameter/width (mm) | Normalized integral intensity | % Error | SBR | Temperature (K) | % Error | SBR | Pearson coefficient | % Error | SBR |
|---|---|---|---|---|---|---|---|---|---|---|
| Holes | 1.2 | 0.69±0.07 | 9.5 | 9.84 | 1930±987 | 5.06 | 5.97 | 0.67±0.03 | 4.5 | 21.3 |
| | 1 | 0.71±0.16 | 23.2 | 10.03 | 1951±38 | 1.96 | 6.18 | 0.64±0.09 | 14.1 | 18.3 |
| Grooves | 2 | 0.73±0.06 | 7.7 | 8.52 | 2056±47 | 2.27 | 7.3 | 0.63±0.08 | 12.7 | 18.3 |
| | 1 | 0.65±0.23 | 36 | 9.95 | 1927±38 | 1.97 | 7.25 | 0.66±0.08 | 12.1 | 19.3 |
| | 0.6 | 0.75±0.07 | 10 | 8.19 | 1906±104 | 5.47 | 6.18 | 0.61±0.09 | 14.7 | 17.3 |
| | 0.3 | 0.69±0.07 | 24 | 7.5 | 1841±38 | 2.06 | 5.06 | 0.72±0.06 | 8.3 | 22 |
| None | | 0.36 ± 0.06 | 16.6 | | 1820.82±69.71 | 3.83 | | 0.97±0.03 | 3 | |

The evolution of the signals related to artificial defects is monitored throughout the deposition of the full walls. The first layer produces the maximum signals from the trenches and holes, and the signals gradually decrease when printing the following layers. Figure 24 shows the Pearson coefficient calculated while depositing the first two layers of the first wall, over the 1 mm hole. The response for the first layer is asymmetric with respect to the defect, and the response from the second layer shows a different size and position of the signal. This means that the second deposited layer is influenced by the defect in the first layer.

The signal magnitude decreases with the increasing number of layers until it disappears. To quantify the evolution of the signal, signal areas are calculated for

the two biggest holes considering signal shifts from consecutive layers. The areas are plotted in Figure 25 as a function of the layer number.

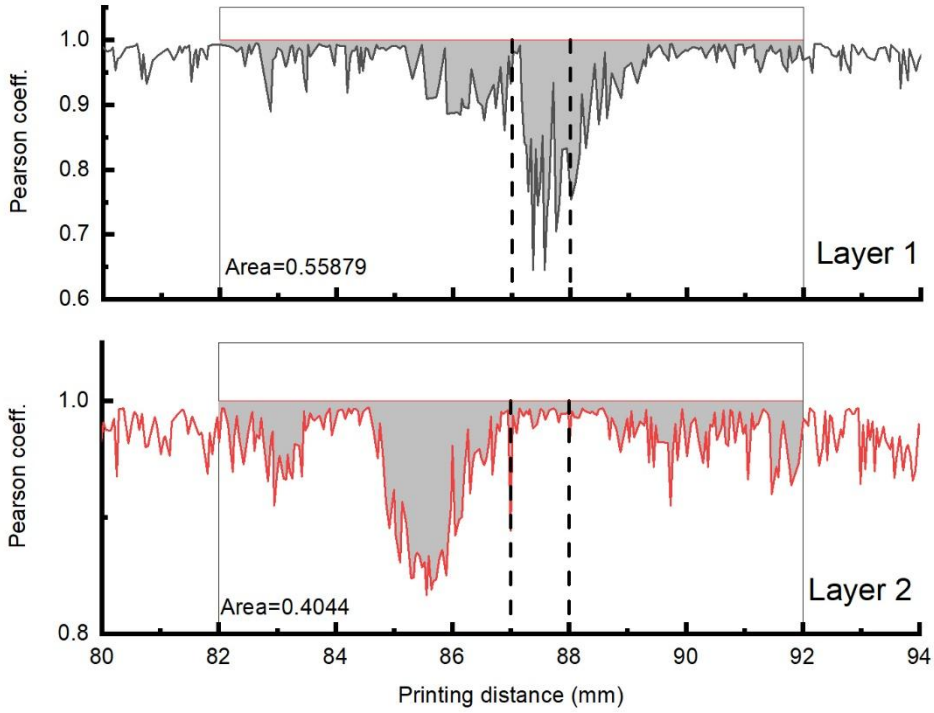


*Figure 24 - Pearson correlation coefficient for first (top) and second (bottom) layer deposited on top of a steel plate with artificial defects, zoom on area with hole with 1mm in diameter. The shaded area is considered affected by the defect, baseline is fixed at 1, hole position in vertical dashed lines.*

A metric changes its behavior when crossing a defect, so the smaller the signal area, the closer the tested surface is to a smooth one.

As expected, the area of the signals from 1.2- and 1-mm holes decreases with the increasing number of layers until the signal disappears after the fourth and third layer, respectively. This occurs when the defects level up with the smooth deposition surface. This, however, does not imply the printed item is flawless.

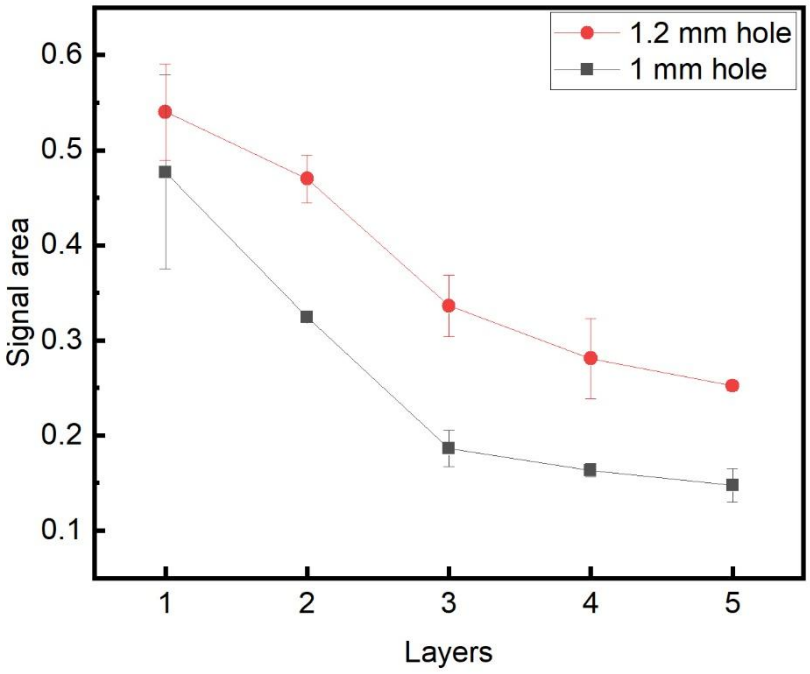


***Figure 25*** *- Area calculated from correlation coefficient signal triggered by depositing on two holes, 1.2- and 1-mm diameter, first five layers from three printed walls. Errors are calculated averaging results from the three walls.*

### 4.1.2 Post-building analysis

After the deposition, the substrate plate was cut along the printed walls to perform a metallographic analysis, which reveals sample characteristics such as crystalline phase, grain size, boundary's structure and position. The interface is exposed, polished, chemically etched with Beraha solution and finally analyzed by an optical microscope with magnification of 2.5 or higher. The results are shown in Figure 26.

Melting and filling the defects with the molten metal occur differently for defects with different geometries. For instance, the grooves leave voids in the final piece

(Figure 26b), while the holes are filled, levelled, and become unnoticeable after several runs (Figure 26a).

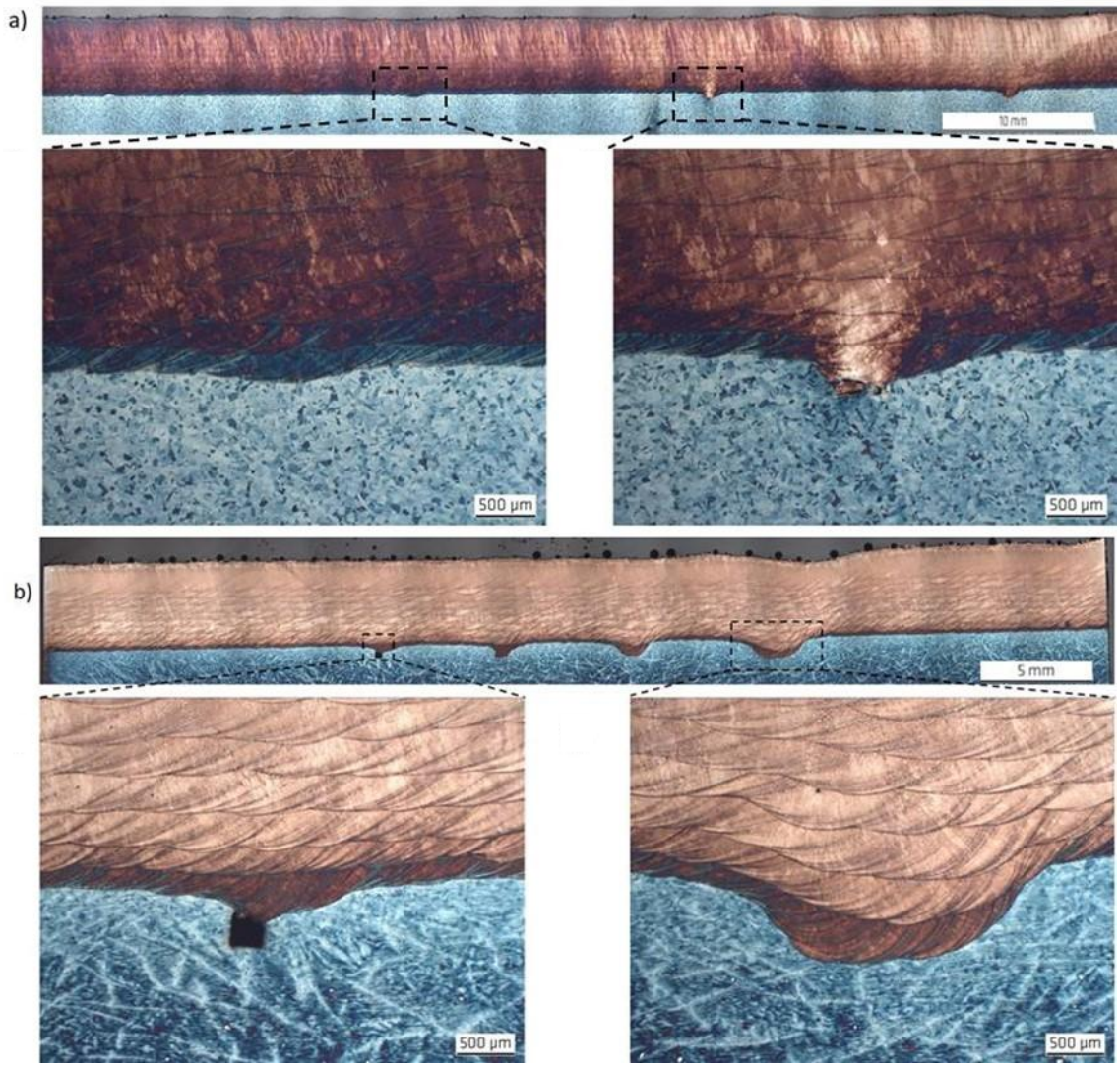


*Figure 26 - Metallographic analysis of the first wall printed on top of artificial defects, performed after a longitudinal cut (printing direction from right to left). a) deposition over holes with zoom on the ones with 0.6 (left) and 1 (right) mm in diameter. b) deposition over trenches with a zoom in the ones with 0.3 (left) and 2 (right) mm width.*

Some defects may remain unfilled and persist through the final item, thus potentially compromising the final product quality (Figure 26b, first zoom).

In this analysis, the colored patterns are linked to the microcrystalline structure in the bulk steel. In Fig. 26a, the change in the pattern inside the layers reveals the presence of the two biggest holes whereas no noticeable difference is

observed for the two smallest ones. This result agrees with the spectroscopic observations.

## 4.2 Thermal diffusion simulation

Establishing a link between process parameters, molten pool emission, piece properties and flaws detectable via OES, is a mandatory step toward the creation of new on-line sensors for the deposition control. Doing this empirically is time and material consuming. Fortunately, there is a possibility to study the relation between process variables and optical signal theoretically, via modelling and simulation. For this reason, a simplified thermal model is developed, based on the time-dependent diffusion-conduction heat equation and a light collection system that accounts for geometrical effects. The model describes the laser heating of a steel plate that contains defects of various geometry and size. It allows the calculation of radiation intensity emitted by a molten pool when the thermal field is either flat or perturbed by surface defects. The simulated emission is processed using the aforementioned metrics of integral intensity, temperature, and correlation coefficient, and the results are supposed to show how the presence of artificial defects influences the emission. The results of simulations are compared to experiments.

### 4.2.1 Theoretical background

In 3D metal printing, a focused laser beam is scanned across the surface of a metal substrate to make the surface melt. Heat dissipates from a first superficial layer into the material bulk and surroundings driven by thermal conduction, thermal

convection, and thermal radiation. This process is modelled by the time-dependent diffusion-conduction heat equation [175]:

$$\rho C_p \frac{\partial \mathrm{T(t,x)}}{\partial \mathrm{t}} + \rho C_p \mathrm{v} \cdot \nabla \mathrm{T(t,x)} + \nabla \cdot \left(-\mathrm{k} \nabla \mathrm{T(t,x)}\right) = \mathrm{q(t,x)} \qquad (4.1)$$

where t and x(x, y, z) are the time and coordinates; ρ [k g $m^{-3}$], $C_p$ [J $kg^{-1}K^{-1}$], T [K], and k(x, T)[W $m^{-1}$ $K^{-1}$] are the mass density, specific heat, temperature, and thermal conductivity, respectively; v [m $s^{-1}$] is the flow velocity, and q(t,x)[W $m^{-3}$] is the internal heat source, if present. Second term in Eq. 4.1 is the convection term that describes internal heat convection; it can be neglected if the surface temperature is below the melting point. If not, the moving boundaries between solid-liquid and liquid-vapor interfaces should be accounted for.

The solid-liquid moving boundary problem, often referred to as Stefan problem, is solved numerically by a variety of methods. Here, the heat capacity method [176, 177] is employed in its modified version, the nominal heat capacity method [178]. The heat equation has the same form but the product $\rho C_p$ in the second term is modified to account for the phase transition [176]

$$C_{app} = \begin{cases} \rho_s C_{p,s}, T < T_s \\ \rho_s C_{p,s} \dfrac{T_s}{T} + \left( \dfrac{\rho_s C_{p,s} + \rho_l C_{p,l}}{2} + \dfrac{\Delta h_f}{\Delta T} \right), T_s < T < T_l \\ \dfrac{1}{T} \left[ \rho_s C_{p,s} T_m + \rho_l C_{p,l} (T - T_m) + \Delta h_f \right], T_l < T \end{cases} \qquad (4.2)$$

Here, $\rho_s$, $C_{p,s}$ and $\rho_l$, $C_{p,l}$ are the densities and specific heats of the solid and liquid material respectively, $\Delta h_f$ is the specific heat of fusion per unit volume, and $T_m$ is the melting temperature. A small temperature interval $\Delta T \sim 0.1$ K is introduced such that $T_s = T_m - \Delta T/2$ and $T_l = T_m + \Delta T/2$, within which the phase transition occurs. It is needed to smooth the discontinuity between $C_{p,s}$ and $C_{p,l}$ that may

cause a numerical problem. The liquid-vapor phase transition is described by the convection term in Eq. 4.1. The convection in the liquid bulk is neglected, assuming this mechanism is less efficient than heat diffusion; so, the convection term describes only the liquid-vapor interface. It is further assumed that vaporization occurs only from a liquid surface when the temperature reaches the boiling point $T_b$ (which rarely happens in 3D printing), no bubble nucleation in the bulk is considered and liquid can reach a superheated ($> T_b$) state. A state of equilibrium between the solid and vapor phase is also assumed; this allows the calculation of the surface recession velocity via the Hertz- Knudsen and Clausius-Clapeyron equations [179, 180]. The former describes the rate of the surface evaporation

$$\frac{1}{A}\frac{\mathrm{d}N}{\mathrm{d}t} = \frac{\alpha p}{(2\pi m k_B T)^{1/2}} \tag{4.3}$$

Where A is the surface area, N is the number of particles evaporated, p is the vapor pressure, m is the particle mass, $K_B$ is the Boltzmann constant, and $\alpha$ is the sticking coefficient ($\alpha \sim 1$) [181].

The atoms inside a single monolayer are dN = $A/\lambda^2$, and time needed for vaporization of one monolayer is dt = $\lambda/v$, where $\lambda$ and v are the average distance between atoms and surface recession velocity, correspondingly. Substituting these into Eq. 4.3 and recalling that $\lambda^3 \sim m/\rho$ the recession velocity is found to be

$$v = \frac{\alpha p}{\rho(2\pi k_B T/m)^{1/2}} \tag{4.4}$$

The equation linking the vapor pressure at the equilibrium and the temperature is computed from the Clausius-Clapeyron equation

$$\mathrm{p} = \mathrm{p}_b \exp\left\{\frac{\Delta \mathrm{H}_v(\mathrm{T}_b)\mathrm{m}}{k_B}\left(\frac{1}{T_b} - \frac{1}{T}\right)\right\} \tag{4.5}$$

where $p_b$ is the reference pressure at the boiling point (1 atm) and $\Delta H_v$ [J $kg^{-1}$]is the latent heat of vaporization. Combining these last two equations

$$v = \frac{\alpha \mathrm{pb}}{\rho(2\pi k_B \mathrm{T}/\mathrm{m})1/2} \exp \frac{\Delta \mathrm{Hv(Tb)m}}{k_B}\left(\frac{1}{T_b} - \frac{1}{T}\right) \tag{4.6}$$

The recession occurs in the direction normal to the surface, normally labelled $z$-direction when the [x,y] plane is parallel to the surface. Then, in a frame of reference attached to the receding surface [179, 182] and without a volumetric heat source q, the heat equation takes the form

$$\mathrm{C_{app}} \frac{\partial \mathrm{T(t,x)}}{\partial \mathrm{t}} + \rho_l \mathrm{C}_{p,l} \mathrm{v}_z \cdot \frac{\partial \mathrm{T(t,x)}}{\partial \mathrm{z}} + \nabla \cdot \left(-\mathrm{k} \nabla \mathrm{T(t,x)}\right) = 0 \tag{4.7}$$

Where $C_{app}$ is the apparent heat capacity given by Eq. 4.2 and subscript z in $v_z$ signifies the only possible direction of the recession velocity. The latter is a simplification; it is exploited not only for defect-free targets but also for targets that have cracks, thuds, and other defects. While in theory there should be evaporation from vertical surfaces like the defect's walls, this effect is neglected, considering that those surfaces are not exposed to laser light.

### 4.2.2 Surface simulation

The studied samples are flat plates with several types of defects: a groove, a hole, a step, a pillar, groove-ripples, lacuna-ripples, a sequence of grooves, and a sequence of holes (Figure 27).

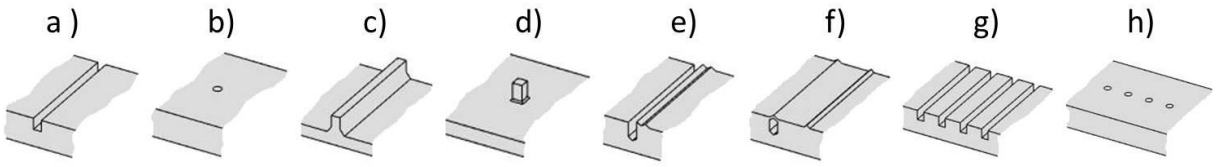


***Figure 27*** *- Sample shapes used in numeric simulations: a) groove; b) hole; c) step; d) pillar; e) groove and ripples; f) lacuna and ripples; g) multiple grooves; h) multiple holes*

To build the shapes and create 3D meshes, the standard Matlab® functions $alphaShape$ and $geometryFromMesh$ are used. After solving the model and obtaining the temperature field, the values of the temperatures are interpolated on a rectangular grid to provide the known uniform areas with known normal vectors to surface elements. This is necessary to calculate the emitted light intensity according to the Stefan-Boltzmann law and the average surface temperature via the blackbody function without further calculation that considers mesh with different sizes.

For calculations, a substrate with a size of $10 \times 4 \times 1$ mm$^3$ (length × width × height along $x$, $y$, and $z$-coordinates, correspondingly) is used. The dimensions of the defects are $0.3 \times 4 \times 0.5$ mm$^3$ for the groove; 0.3 mm× 0.5 mm (diameter × depth) for the hole; $0.3 \times 4 \times 0.5$ mm$^3$ for the step; $0.3 \times 0.3 \times 0.5$ mm$^3$ for the pillar; $0.3 \times 4 \times 0.5$ mm$^3$ for the groove with 2 equilateral triangular ripples next to it and 0.1 mm tall; $0.3 \times 4 \times 0.5$ mm$^3$ for the lacuna covered by the 0.1 mm thick ripple plus another 0.1 mm tall ripple 2.4 mm apart from lacuna center; four $0.3 \times 4 \times 0.5$ mm$^3$ grooves separated by 1 mm, and four 0.3 mm × 0.5 mm (diameter × depth) holes also separated by 1 mm.

### 4.2.3 Light collection geometry

Along with the emission from a defective surface, the light acquisition is simulated for monitoring purposes, assuming an optical set-up with a lens and a

spectrometer. In experiments, only an angular light collection is possible due to the printer geometry. A typical distance of the optical head from the printing spot is 20-30 cm and the diameter of normal projection of the collection aperture on a sample surface is 1.2 mm, close to a 1.6 mm diameter of the laser beam that is used in both simulations and experiments.

The emission is modelled as a parallel beam of light emitted by a hot sample surface and collected into an optical element (a lens). The beam makes an angle $\theta$ with the surface normal and an angle $(\pi/2 - \theta)$ with normal to vertical faces of the defects. The emission is assumed to have an ellipse profile on both the top and vertical faces, meaning it is constrained to have coordinates $(x - x_0)^2/(r/\cos(\theta))^2 + (y - y_0)^2/(r)^2 \leq 1$ and $(z - z_0)^2/(r/\cos(\pi/2 - \theta))^2 + (y - y_0)^2/(r)^2 \leq 1$, correspondingly. Here, (x, y, z) are the coordinates of the points on sample faces, $(x_0, y_0)$, and $(z_0, y_0)$ are the centers of ellipses on the horizontal and vertical faces, and $r$ is the radius of the light beam cylinder (collection aperture). The coordinates of the beam center $(x_0, y_0)$ are known by design while $z_0$ is calculated via $z_0 = z_2 + (x_1 - x_0)/\tan(\theta)$ for the front wall of the groove and the hole vertical slices at coordinates $x1$ (see Figure 28) and via $z_0 = z_1 + (x_2 - x_0)/\tan(\theta)$ for the back walls of the step and pillar.

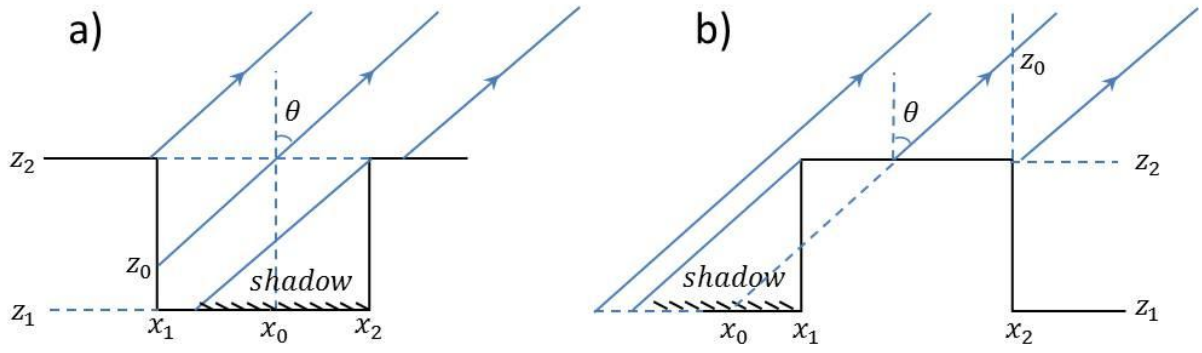


*Figure 28- Light collection geometry; a) for groove and hole; b) for step and pillar*

The shadows cast by the vertical surfaces of the defects should be accounted for. The corresponding constraints are: $z \geq z_2 - (x_2 - x_1)/\tan(\theta)$ (groove wall); $x \leq x_2 - (z_2 - z_1) \cdot \tan(\theta)$ (groove bottom); $x \leq x_1 - (z_2 - z_1) \cdot \tan(\theta)$ (surface behind step); and all x's and y's except ( $x > x_1 - (z_2 - z_1) \cdot \tan(\theta)$ & $x < x_1$ & $y > y_1$ & $y < y_1$) (surface behind pillar). When calculating the radiation intensity, the radiation emitted by each surface element is multiplied by the corresponding directional cosine to account for the element orientation with respect to the line of observation.

### 4.2.4 Boundary conditions

A crucial point when solving the heat equation is to specify the initial and boundary conditions. The simplest initial condition is

$$T(t,x)|_{t=0} = T_{amb} \tag{4.8}$$

Where $T_{amb}$ is the ambient temperature ($T_{amb}$ = 298 K). The Neumann boundary conditions are applied to the top surface of the plate, step and pillar, and bottom faces of the hole and groove. The plate is heated by the laser scanning across its surface and cooled, apart from bulk thermal diffusion, by spontaneous radiation, vaporization, and air convection:

$$J(t,x)|_{z=0} = 0 = J_{Las} - J_{rad} - J_{vap} - J_{con} \tag{4.9}$$

Side faces of defects dissipate heat by convection and radiation. The fluxes in Eq. 4.9 are

$$\begin{cases} J_{Las} = (1-R)\frac{2P_L}{\pi r_L^2} exp\left\{-\frac{2[(x-x_c)^2+(y-y_c)^2]}{r_L^2}\right\}, (x-x_c)^2+(y-y_c)^2 \leq r_L^2 \\ J_{rad} = \varepsilon\sigma_S(T^4-T_{amb}^4) \\ J_{vap} = \rho_l \Delta H_v v_z, T > T_m \\ J_{con} = h_{con}(T-T_{amb}) \end{cases} \quad (4.9a)$$

Where R is the surface reflectivity, $P_L$ [W] is the laser power, $r_L$ is the radius of the focused laser beam, $\varepsilon$ and $\sigma_S$ [W cm$^{-2}$ K$^{-4}$] are the surface emissivity and Stefan-Boltzmann constant respectively, $h_{con}$ [W cm$^{-2}$ K$^{-1}$] is the convection coefficient in air, and ($x_c$, $y_c$) are the coordinates of the laser spot center such that $x_c = x_0 + v_L t$ and $y_c = y_0$ where ($x_0$, $y_0$) is the starting laser spot position and $v_L$ is the velocity of the laser head. The laser power has the Gaussian distribution over the spot. The other faces of the block except the bottom are insulated that implies the zero-flux Neumann boundary condition $\boldsymbol{n} \cdot k\boldsymbol{\Delta T} = 0$, where $\boldsymbol{n}$ is the surface normal. The bottom is kept at a constant temperature $T_{amb}$ behaving as infinite heat sink and a Dirichlet boundary condition at its face. Heat equation (4.7) is solved using the standard Matlab®@2020a PDE toolbox.

### 4.2.5 Experimental

The experiment is performed with following process parameters: a laser spot diameter of 1.6 mm, a scanning speed is 13.3 mm s$^{-1}$ and a powder mass flow of 0.25 g s$^{-1}$. The print is performed in two different modes, the first with low laser power of 450 W and no blown powder, the second with 800 W laser power, with the laser scanning across the defects on the substrate. The whole set-up with a highlight on the defected substrate is reported in Figure 29.

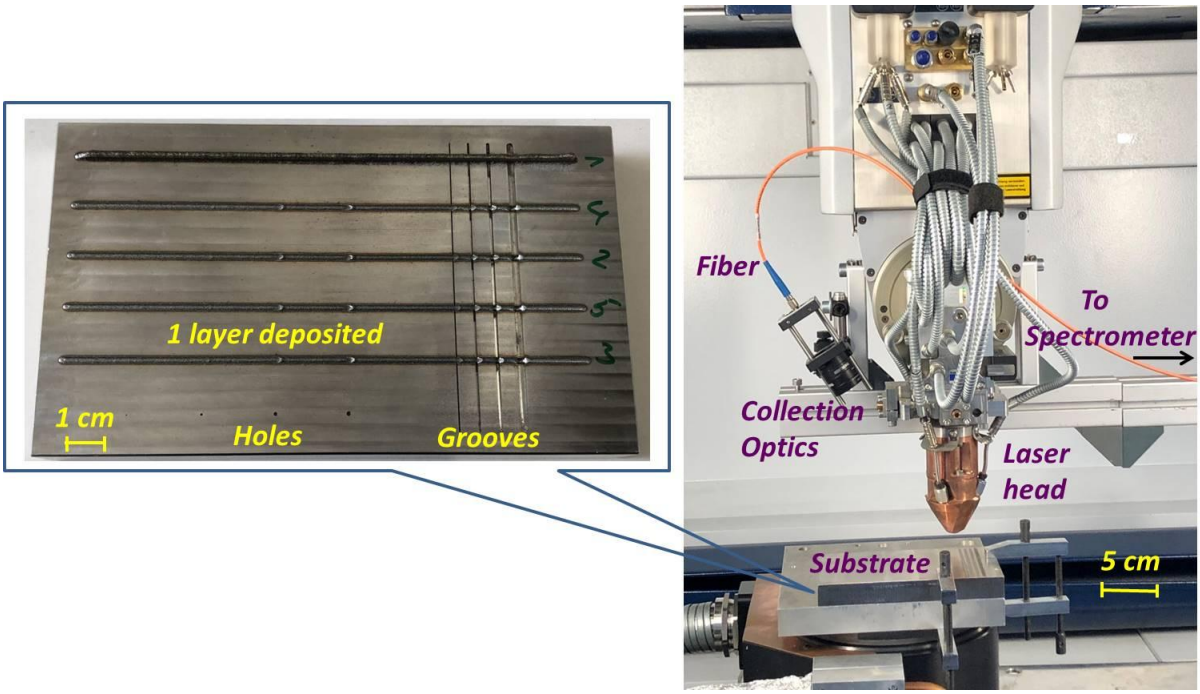


***Figure 29*** *- Laser head of the printer, with attached the collection optics. In inset: steel plate with four grooves and six rows of four holes carved on the surface, with five single layers deposited across the defects.*

### 4.2.6 Results and discussion

#### 4.2.6.1 Simulation

This simulation aims to represent the influence of surface defects on the sample temperature field, and finally on its emission. The sample composition is assumed to have low influence, so a plate made only of iron is simulated, since it has well known and established thermal properties, listed in Table 9. In Table 10 there are the other parameters needed to solve the model.

The emission spectra are processed to calculate the monitoring metrics. To calculate the temperature, emission from surface elements $S_i(\lambda)=(2hc^2/\lambda^5)\cdot[\exp(hc/\lambda kT_i) - 1]^{-1}$ are simulated within a spectral range of 0.2 – 10 µm and summed up to obtain resulting spectrum $S(\lambda) = \Sigma_i S_i(\lambda)$.

*Table 9 - Physical and thermal characteristics of iron: $M$ is the atomic mass; $\rho_S$ and $\rho_L$ are the density of solid and liquid iron; $T_{fus}$, $T_{vap}$, $H_{fus}$, and $H_{vap}$ are the temperatures and heats of fusion and vaporization; $C_p^S, C_p^L$, $k_S$ and $k_L$ are the specific heat capacities and thermal conductivity coefficients of solid and liquid iron; $\varepsilon$, $\alpha$, and $R$ are the surface emissivity, sticking coefficient, and reflectivity at 1030 nm.*

| $M$ | $\rho_S$ | $\rho_L$ | $T_{fus}$ | $T_{vap}$ | $H_{fus}$ | $H_{vap}$ | $C_p^S$ | $C_p^L$ | $k^S$ | $k^L$ | $\varepsilon$ | $\alpha$ | $R$ |
|---|---|---|---|---|---|---|---|---|---|---|---|---|---|
| kg | kg/m$^3$ | kg/m$^3$ | K | K | kJ/kg | kJ/kg | J/kg K | J/kg K | W/m K | W/m K | -- | -- | -- |
| 9.3e-26 | 7874 | 7874 | 1811 | 3140 | 247 | 6250 | 444 | 825 | 80.2 | 38.0 | 0.9 | 1 | 0.6 |

*Table 10 - Laser and light collection parameters: $P_L$ is the laser power; $v_L$ is the velocity of the laser head; $r_L$ is the radius of the laser focal spot on the surface; $r_D$ is the radius of the light collection spot on the surface; $\theta$ is the angle between the line of observation and surface normal; $h_{con}$ is the heat transfer coefficient due to air convection.*

| $P_L$ | $v_L$ | $r_L$ | $r_D$ | $\theta$ | $h_{con}$ |
|---|---|---|---|---|---|
| kW | mm/s | mm | mm | deg | W/m$^2$ K |
| 0.1-2.0 | 13.3 | 0.8 | 0.6 | 30 | 10 |

This spectrum is again fitted by the Planck function which gives back the temperature $T_{av}$. Apparently, this fitting is not exact owing to inhomogeneity of the temperature field; the surface spots with higher temperature dominate the final sum ($\lambda$). In Figure 30 are reported examples of thermal fields distorted by six different surface defects and an average spectrum fitted with the blackbody function.

The second metric, spectrally-integrated intensity, is more sensitive toward small variations in the temperature field as it varies with 4th power of the temperature according to the Stefan- Boltzmann law $I = \varepsilon\sigma \sum_i T_i^4 \cdot \cos\theta_i$, where $\varepsilon$ is the surface emissivity, $\sigma$ is the Stefan-Boltzmann constant, and summation is taken over all surface elements that fall within the observation spot; $\theta_i$ is the angle between the surface element normal and the observation direction.

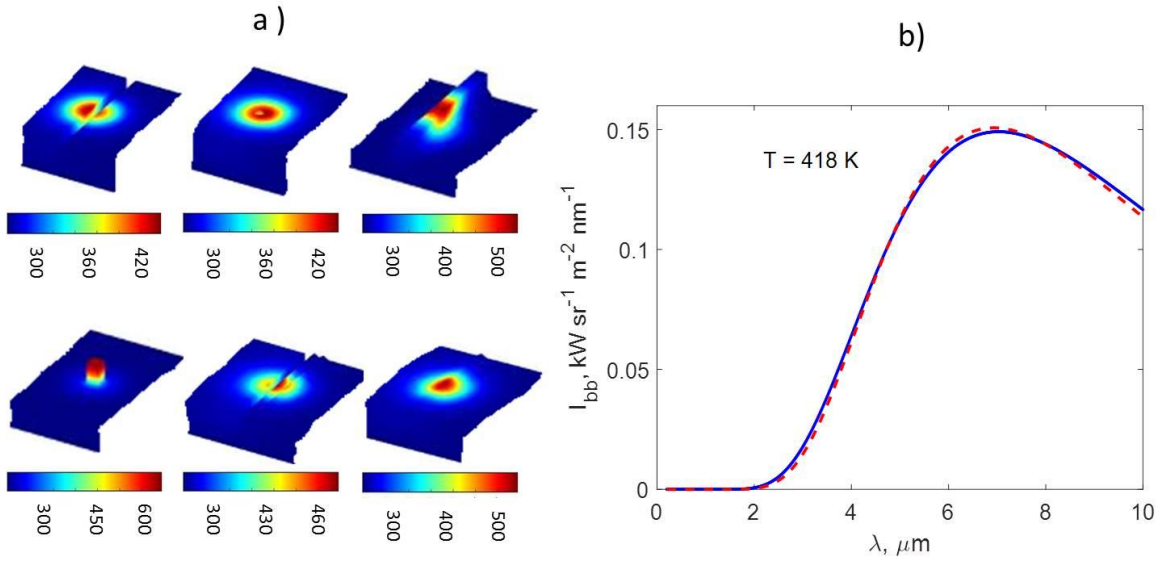


*Figure 30 - a) Temperature field (in K) around different defect types; b) average temperature of the step (third image in upper row) determined from blackbody emission spectra. Blue and red lines are the sum of spectra from surface elements and blackbody fit function, correspondingly.*

The third metric is the correlation coefficient, as already introduced.

Convergence of simulations is tested first; it is achieved with a maximal spatial step of 0.5 mm and a time step of 0.01 s. Next, the effect of phase transitions like melting and vaporization on the temperature field are checked by varying the laser power from 100's W to 2 kW; the results are shown in Figure 31. Vaporization can be either included or excluded in calculations by including or not the convection term in Eq. 4.1. When included, it contributes to lowering the temperature surface for high laser powers of up to 2 kW and does not let the temperature rise above the boiling point $T_{vap}$ = 3140 K. When excluded, that

corresponds to no vaporization condition, other cooling mechanisms like thermal radiation and air convection cannot prevent the surface temperature from rising above the boiling point. At lower laser powers, the convection term does not affect the surface temperature unless the temperature approaches $T_{vap}$, at which intense vaporization starts.

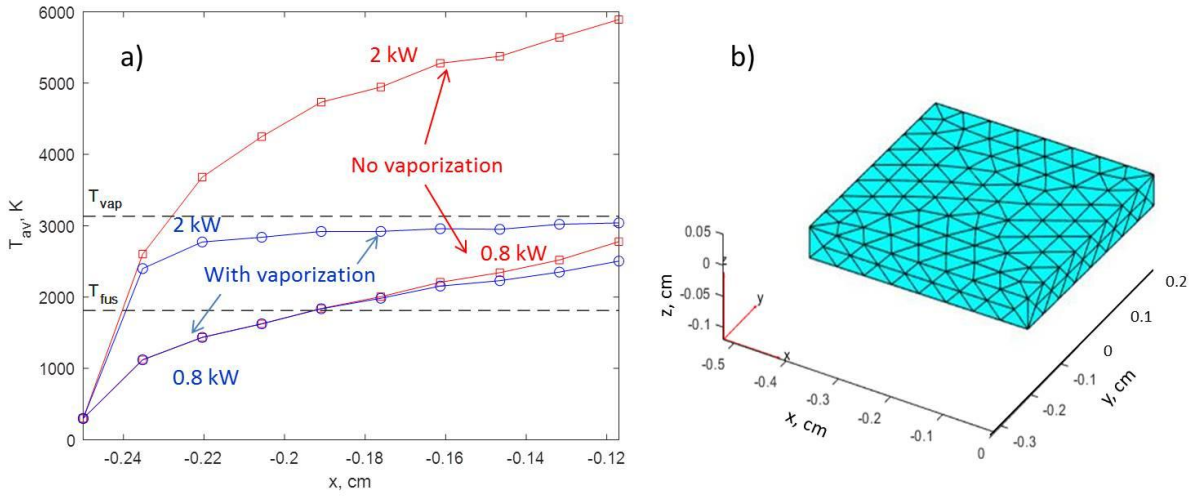


***Figure 31*** *- a) Effect of convection term (2nd term in Eq. 4.1) on the temperature field at two laser powers of 0.8 kW and 2 kW; circles and squares mark the vaporization on and off conditions, correspondingly; b) flat plate with a triangular grid used in these simulations.*

Computations that consider vaporization are time and resources consuming, requiring many hours with a medium- performance PC, since they involve numerous volumetric grid cells and run through many iterations until the result converges. In many instances, the PC with a 16 Gb RAM (random access memory) runs out of memory. For these reasons, further simulations are run for the low laser power of 80 W. With that power the target is heated to moderate temperatures of 400 – 600 K and a limited number of grid cells is involved in calculations, thus avoiding reaching boiling temperature, or even melting temperature. While this does not represent the printing in the real world, the influence of surface defects on thermal field would be still valid, since it does not depend on a specific value of the temperature. This is true only until the flow

motion changes the shape of a defect; however, that is not a part of the model anyway. The model includes only surface recession by vaporization, which has no significant effect on defects geometry, even at high laser powers.

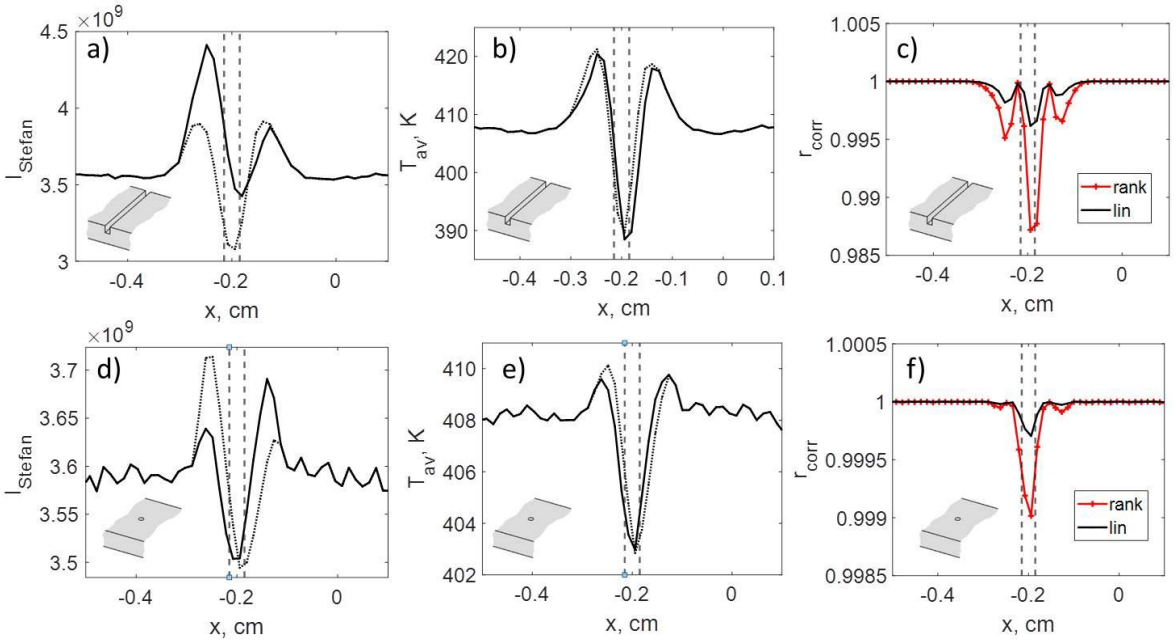


*Figure 32 - Response of the three metrics to a presence of inner surface defects: groove (a-c) and hole (d-f): (a, d) integral intensities; (b, e) average temperatures; (c, f) correlation coefficients. Scan direction is from left to right; solid and dotted lines represent the rear and front positions of optics relative to the scan direction. Dashed vertical lines mark the positions of the front and rear edges of defects.*

In experiments, test scans are performed with low laser power and no metal powder to approximately reproduce the conditions in simulations. Regular printing scans at elevated laser power and metal powder supply are run too and compared to simulations as well. It is noticed experimentally that scanning with low laser power does not alter the defects shape, making the comparison of experiments with simulations possible.

In simulations, the possible printing flaws are mimicked by generating geometrical shapes that contain inner and protruding defects. The characteristic dimensions of the defects (~0.3 mm) are intentionally made smaller than the laser spot (1.6 mm) and collection beam (1.2 mm) diameters and, consequently, much

smaller than the heat-affected area on the sample surface. Defects this small are realistic during 3D printing. The behavior of the metrics due to inner defects, groove and hole, is shown in Figure 32.

The metrics response is evident, and changes according to the type of defect simulated, showing different signals for different defect shapes, meaning that different surfaces affect differently the thermal field. For the groove, the temperature (Fig.32, b) and integral intensity (Fig.32, a) are higher on the sides and decrease toward the bottom. For the hole, these characteristics (Fig.32, d and e) are similar but have lower amplitudes. The correlation coefficient (Fig.32, c and f) varies insignificantly as it is sensitive to only the shift between the current and reference spectra. The change is very small for a small variation in the temperature, e.g. within a range of 10-30 K like the one shown in Fig.32, b and e. The asymmetry in the signals originates from the non-uniform heating of the surface near the defects, angular collection geometry (Fig.28), and position of the optics relative to the molten pool; i.e., on a rear or a front side of the scanning laser head. The difference between these two positions of the detection optics is shown in Figure 32 and due to a varying collection angle in Figure 33.

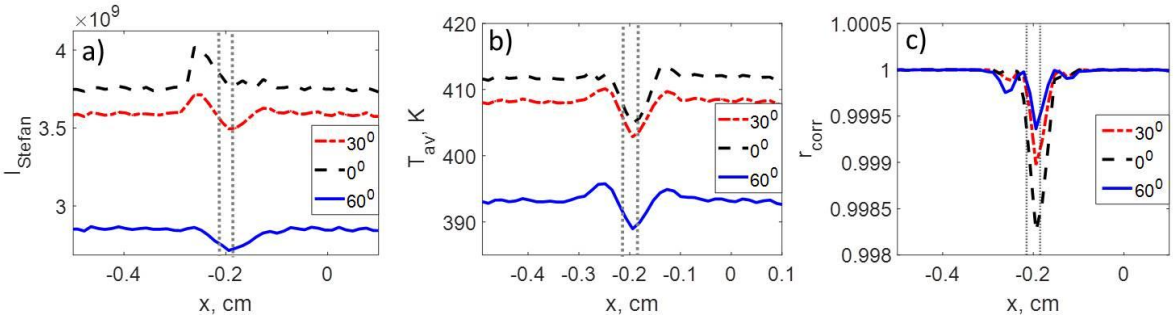


***Figure 33*** *- Dependence of a) integral intensity; b) surface temperature; and c) rank correlation coefficient upon angle of observation; scan direction is from left to right*

The recorded signal is more intense along the surface normal and decreases with the increase of the collection angle since the collection efficiency changes with

$cos\theta$. This suggests that sensitivity can be improved by collecting emitted light from multiple directions. As evidenced in Fig.32, the most sensitive metric is the integral intensity because of its 4$^{th}$ power temperature dependence. It varies by 14 % and 3 % relative to the baseline when scanning across the groove and the hole, correspondingly. The average temperature and correlation coefficient show the smaller variations of 5 % and 1 % and 1 % and 0.1 %, respectively. The small variations in $T_{av}$ and $r_{corr}$ may result in losing these signals in noise when scanning across small defects. In this respect, the integral intensity presents the most robust metric. The rank correlation shows a stronger response than the linear correlation and it is in general more robust [9]. The geometry of the correlation coefficient signal well reproduces the true dimensions of the defects; their FWHM's (full widths at half maxima) almost coincide with the defect widths while FWHM's of the downward features of the integral intensity and average temperature are significantly wider.

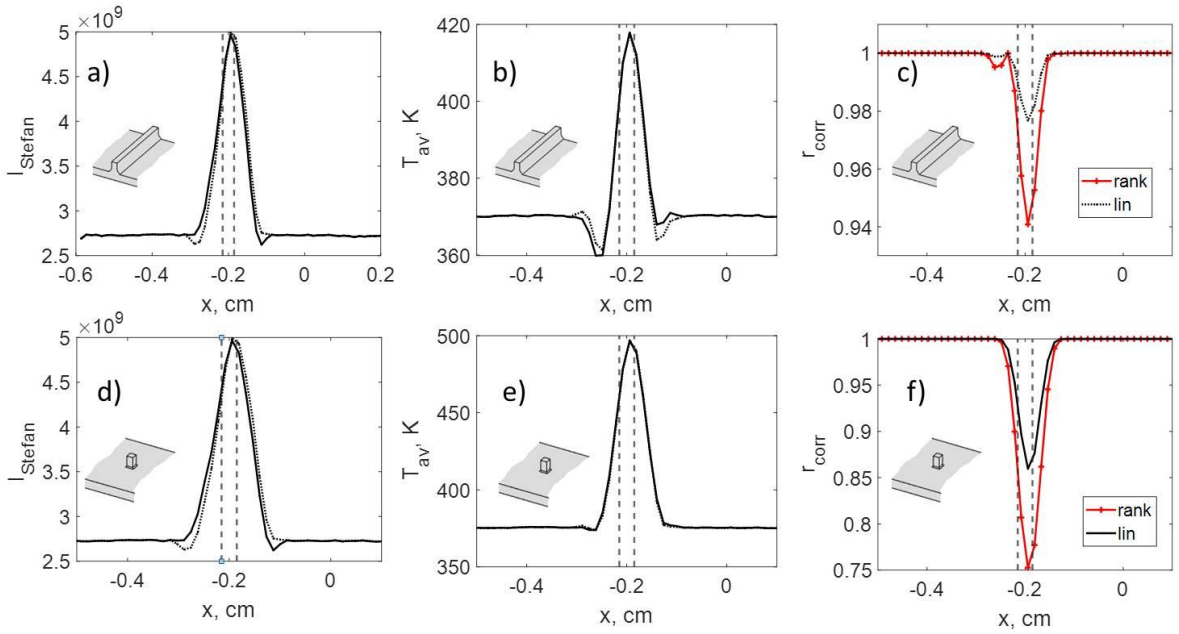


*Figure 34 - Response of the three metrics to the presence of protruding surface defects: step (a-c) and pillar (d-f): (a, d) integral intensities; (b, e) average temperatures; (c, f) correlation coefficients. The scan direction is from left to right; the solid and dotted lines represent rear and front positions of optics with respect to the scan direction. Dashed vertical lines show the positions of front and rear edges of the defects.*

Outward defects step and pillar (Figure 34) result in very different shapes and higher signals as compared to inward defects, due to the final average temperature being higher. For the step, an increase in the integral intensity, average temperature, and correlation coefficient is 1.9-, 1.1-, and 0.06-folds and for the pillar is 1.9-, 1.3-, and 0.25- folds, correspondingly. A significant variation occurs at the pillar for the correlation coefficient; it drops by 25% from its maximum (undisturbed) value. This happens because of a significant shift between the blackbody curves corresponding to the surface (370 K) and pillars (500 K) temperatures. Thus, the correlation coefficient works well with defects that create large disturbance in the temperature field. Like with inward defects, FWHM's of the signals are larger than defect size meaning that their original dimensions cannot be determined from signal shapes. But the character of the defect, inward or outward, still can be deduced from the signal shape as follows from Fig.32 and 34. Opposite to wavy shapes of the signals induced by inner defects, signals from protruding defects are smoother and bell-shaped or inversed bell-shaped. Two other defect types are simulated, groove-ripples and lacuna-ripples, and the generated signals are shown in Figure 35.

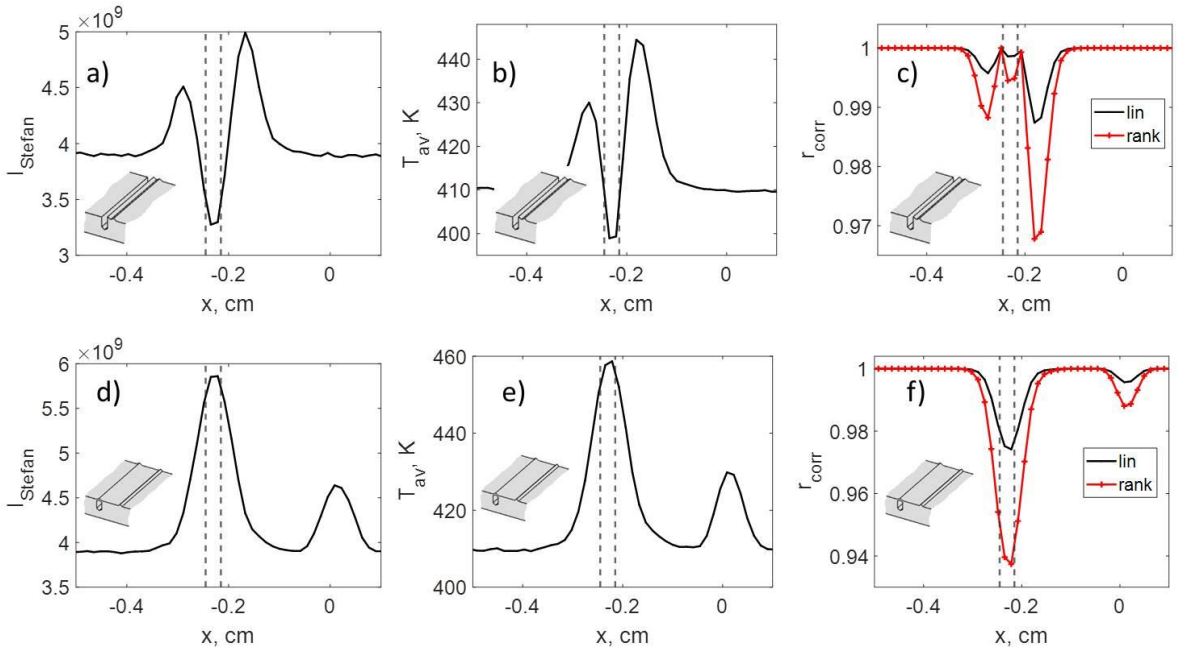


***Figure 35*** *- Response of the three metrics to the presence of combined surface defects: groove-ripples (a-c) and lacuna-ripples (d-f): (a, d) integral intensities; (b, e) average temperatures; (c, f) correlation coefficients. The scan direction is from left to right, rear position of optics with respect to the scan direction. The dashed vertical lines show the positions of front and rear edges of the groove (a-c) and lacuna (d-f).*

Signals from the groove-ripples (Fig.35, a-c) are similar to those from the groove but their asymmetry is increased. This asymmetry is produced by protruding ripples. The lacuna-ripples act as protruding defects as well; they generate a positive response for the integral intensity and temperature and strong negative response for the correlation coefficient. The presence of lacunas under the surface increases the surface temperature above. As deduced from experiment, groove-ripples are characteristic to deposits on surfaces with inner defects (cracks, holes, crevasses etc.). The deposition powder is distributed unevenly around defects that result from fast unidirectional motion of printer nozzle. Small asymmetric bumps build up on one side of inner defects that produce signal asymmetry like the one shown in Fig.35, a-c.

Next simulations are performed considering a deposition on defected substrate that is also been tested empirically.

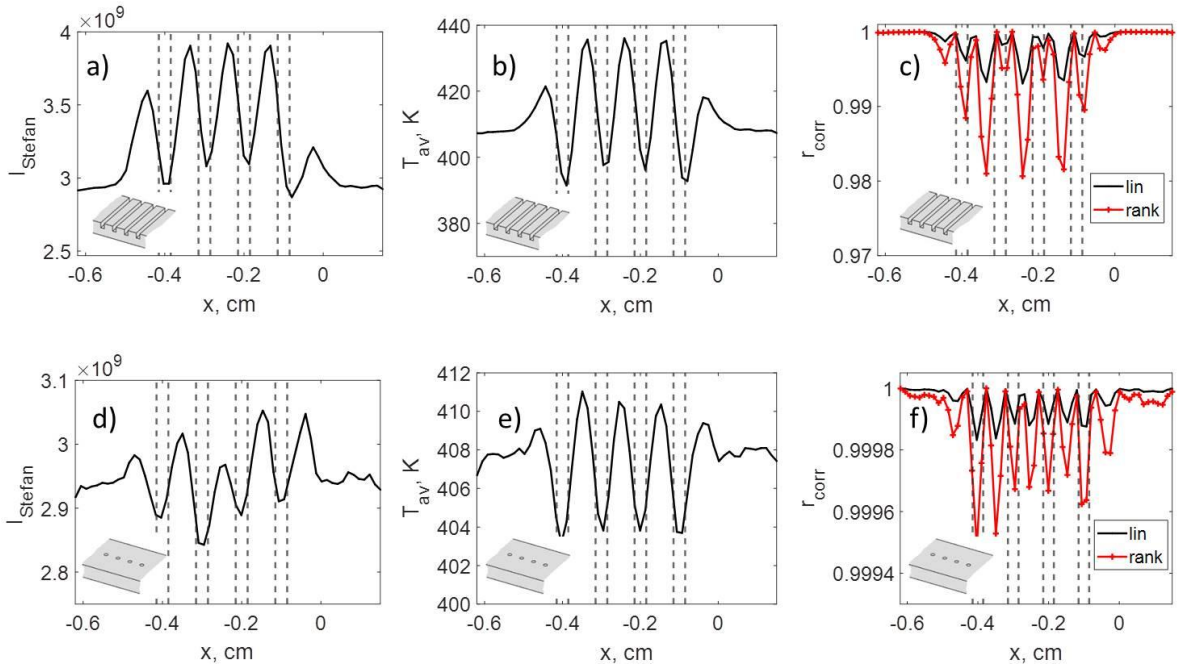


***Figure 36*** *- Response of three metrics to the presence of sequence of surface defects: four grooves of the same size (a-c) and four holes of the same diameters (d-f): integral intensities (a, d); average temperatures (b, e); and correlation coefficients (c, f). The scan direction is from left to right, rear position of optics with respect to the scan direction. The dashed vertical lines show the positions of front and rear boundaries of grooves (a-c) and holes (d-f).*

Figure 36 shows the responses of the three metrics to a sequence of 4 grooves and 4 holes, the same pattern of artificial defects already used. Here, limited spacing between the defects and inertia of heat conduction blurs the signal boundaries; the surface between the defects is heated to a higher temperature, as with the protruding defect. The temperature varies in ranges of 50 K and 10 K for the grooves and holes, respectively, thus responses from the holes are shallower than those from the grooves, especially correlation coefficients. As with the former simulations, the signals show specificity toward the defect type. It can be speculated that simulating a large array of defects may provide enough insight to identify the type of defect based on solely the optical signals. Thus, the simulations demonstrate that small printing defects can be monitored with the help of optical spectroscopy. The most sensitive metric in this regard is the integral intensity as it exhibits the strongest dependence upon the temperature. Detecting the temperature yields similar results, although with less sensitivity.

The third metric, correlation coefficient, is not very sensitive for detection of inner defects but gives signals closer in size to the real defects. It also becomes very sensitive for identification and detection of defects of a protruding type but in this case information about the defect dimensions is lost. The reported results show how inward (cracks, crevasses, voids) and outward (steps, bumps, ripples) defects generate markedly different signals.

#### 4.2.6.1 Experiment

Another empirical experiment is repeated scanning the laser on a plate with artificial defects in order to compare its results with the ones obtained from the simulation. To this goal, the same experiment is performed with both standard parameters and parameters closer to the simulated ones, to check for potential discrepancies. A first scan, recorded in the IR region, is made with a low laser power of 450 W and no powder, and a second scan, recorded in the UV-Vis, with a laser power of 800 W and powder flux as per a standard procedure. The emission is evaluated by calculating the usual metrics. In the IR spectra, the water absorption band peaked around 1450 nm has been bypassed to improve the black body fitting. It is worth emphasizing that the conditions in experiment and simulations are not the same, since the simulation involves a laser power so low that it does not ignite bulk phase transition, and also does not include incoming powder. These two simplifications imply no change of the substrate surface in simulations. Still, since the impact from the defects is not dependent on the temperature, the simulation remains valid, and the following results support this.

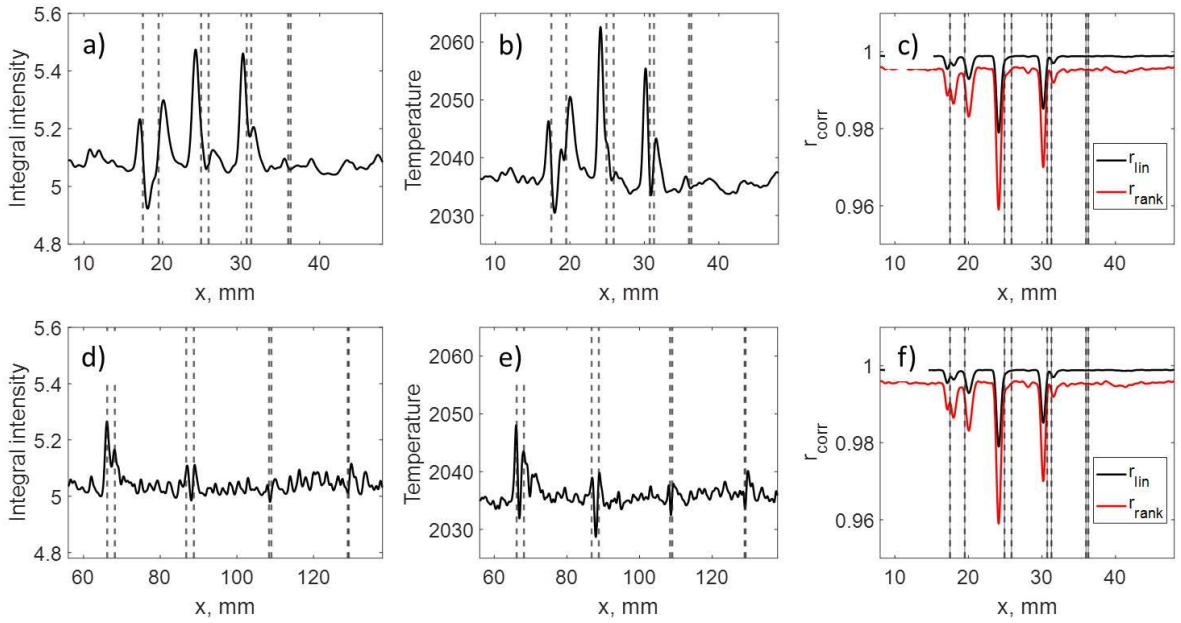


*Figure 37 - Response of the three chosen metrics while scanning (from left to right) across the series of four grooves (a-c) and holes (d-f) at low laser power of 450 W without powder; (a, d) integral intensities; (b, e) average temperatures; (c, f) correlation coefficients. Optics are in the rear position relative to the scan direction. The dashed vertical lines show the positions of front and rear edges of defects.*

Figure 37 shows the integral intensity, average temperature, and correlation coefficients obtained while printing across the defective surface at low laser power of 450 W without powder. From the comparison with Fig.36, which shows signals from a simulation with the sample having similar artificial defects, it is evident the presence of a similar pattern for both series of trenches (rows a-c in Fig.30 and 32) and holes (rows d-f in Fig.30 and 32). Figure 38 shows the same metrics obtained during printing of one metal layer across the same series of grooves and holes. Here again there is a strong response from grooves with different widths and the two largest holes and no response from two smallest holes with diameters of 0.6 mm and 0.3 mm, similarly to what has already been recorded in the previous experiment involving a steel plate with artificial defects. It is likely that the defects are filled with the incident powder and quickly smoothed without causing any significant distortion in the temperature field.

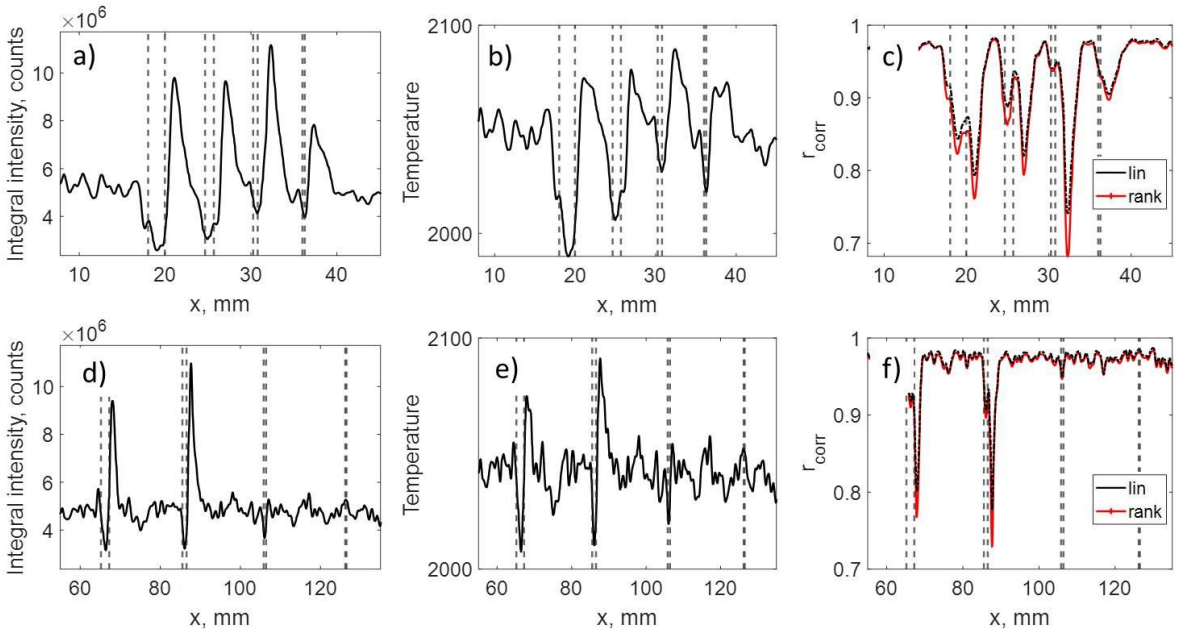


***Figure 38*** *- Response of the three chosen metrics while scanning (from left to right) across the series of grooves (a-c) and holes (d-f) at elevated laser power of 800 W with powder; (a, d) integral intensities; (b, e) average temperatures; (c, f) correlation coefficients. Optics are in the rear position relative to the scan direction. The dashed vertical lines show the positions of front and rear edges of the defects.*

All signals have their minimum near centers of the defects and exhibit spikes at right sides of them relative to the direction of the laser scan (from left to right), opposite to the optical acquisition system. These shapes are similar to the ones reported from the simulations about the groove-ripples defect type (Fig.35, a-c); they point to the presence of surface reduction followed by a bump. Such geometry is confirmed by analyzing the surface after layered printing, as already reported in Fig. 26. Here, the wave-like structure around the grooves propagates from the first to the upper layers. Also, the grooves appear to be not completely filled after the deposition, probably due to the inertia of the powder supply that is not well matched to the welding velocity.

# 5 Conclusions

1. An optical set-up has been integrated on a metal additive manufacturing machine in order to study the possibility of using it as on-line monitoring device. Systematic experiments have been performed recording the molten pool emission while depositing with different processing parameters, generally involving low power laser.
2. Due to the low energy input, during the deposition there is not the formation of a stable plasma, rather the emission of thermal radiation, which is used as the sole source of analytical information.
3. The temperature of the molten pool is calculated from its emission after calibration of light detectors. Due to instrumental factors and the pool surface dynamic, it is not possible to calculate the melted steel average temperature, nonetheless it is a relevant parameter when monitoring the deposition process.
4. The molten pool emission is the result of different machining variables acting together, that are sometimes in literature grouped together in bigger experimental parameters. In experiments we show that several metrics extracted from the molten pool emission seem to be in linear relation to the parameter energy density, but clearly further studies are needed.
5. The same set-up has been tested to monitor on-line abrupt change in the emission trend that may link to a defect in the ongoing deposition. Surface defects with known position and geometry have been carved on top of a substrate plate in order to test the spatial resolution of the optical sensor, which has been established in being 1 mm.

6. A simulation of a laser-metal interaction phenomenon has been performed via a simplified thermal model, that models the emission from a metal plate heated by a laser. The surface of this plate is not flat but has several geometries carved on top of it, some resembling the ones present in the empirical experiment and some new. The simulated emission is processed in the same way as in the real experiment, providing similar results. This shows that such a system can be modelled and reliable results are obtainable without having to resolve to physical experiments.

# 6 Statement of independent work

All the results and the overall investigation here reported are obtained directly by the author or with his close participation. The author participated in experimental conceptualization, implementation, and data processing, as well as writing this text.

# 7 Scientific output

N. Scheuschner, S. Altenburg, G. Pignatelli, C. Maierhofer, A. Straße, I. B. Gornushkin, A. Gumenyuk. Vergleich der Messungen der Schmelzbadtemperatur bei der Additiven Fertigung von Metallen mittels IR-Spektroskopie und Thermografie. *Technische Messen*. 2021. Doi: 10.1515/teme-2021-0056

G. Pignatelli, A. Strasse, A. Gumenyuk, I. Gornushkin. Online monitoring of 3D printing of steel via optical emission spectroscopy. *Materials Testing*. 2022. Doi: 10.1515/mt-2021-2082.

I.B. Gornushkin, G. Pignatelli, A. Straße. Optical detection of defects during laser metal deposition: Simulations and experiment. *Applied Surface Science*. 2022. Doi: 10.1016/j.apsusc.2021.151214.

# 8 Abbreviations

AM Additive Manufacturing

BPP Beam Parameter Product

CAD Computer Aided Design

CW Continuous Wave

DED Direct Energy Deposition

EBSD Electron Back Scattered Diffraction

FGM Functionally Graded Materials

FWHM Full Width at Half Maxima

GA Gas Atomization

IR InfraRed

ISO International Organization for Standardization

LENS Laser Engineered Net Shaping

LIBS Laser Induced Breakdown Spectroscopy

LOF Lack of Fusion

LTE Local Thermodynamic Equilibrium

OD Optical Density

OES Optical Emission Spectroscopy

PBF Powder Bed Fusion

PID Proportional Integral Derivative

PREP Plasma Rotating Electron Process

RAM Random Access Memory

SBR Signal to Background Ratio

SEM Scanning Electron Microscopy

SLM Selective Laser Melting

UV Ultraviolet

Vis Visible

YAG Yttrium Aluminum Garnet

# 9 List of figures

**Figure 1** – Schematic of a three-level (a) and four-level (b) laser. 2

**Figure 2** – Yb:YAG energy levels available for pumping and lasing. 4

**Figure 3** – Beam profile for a gaussian beam. 6

**Figure 4 –** Copper optical properties as a function of incoming frequency. 12

**Figure 5** – Laser material processing techniques with respective parameters. 14

**Figure 6** – Normalized depth plotted against normalized enthalpy. 20

**Figure 7** – Defects during a deposition and respective causes. 24

**Figure 8** – Temperature gradient G vs growth rate R. 25

**Figure 9** - Two cameras, in paraxial and in coaxial configuration. 32

**Figure 10** – Custom LIBS probe on AM laser head. 39

**Figure 11** – TruLaser Cell AM set-up. 43

**Figure 12** – Laser head with optical set-up. 45

**Figure 13** – Comparison of thermal and plasma emission. 47

**Figure 14** – Emission recorded from a three layer deposition. 50

**Figure 15** – Spectrum recorded in IR and respective black body fitting. 53

**Figure 16** - Temperature calculated while printing a three-layer wall. 54

**Figure 17** - Temperature with interla or external calibration. 55

**Figure 18** – Temp. with internal calibration from a three layer deposition. 56

**Figure 19** - Temperature and intensity while changing energy density. 58

**Figure 20** - Temperature and intensity for a 10 layers deposition. 59

**Figure 21** – Rank coefficient while laser is turned off. 63

**Figure 22** – Monitoring metrics for deposition on artificial defects. 67

**Figure 23** – Correlation coefficient repeated for reproducibility. 68

**Figure 24** - Correlation coefficient evaluated on following layers. 71

**Figure 25** – Signal area on 1.2 and 1 mm holes. 72

**Figure 26** – Metallographic analysis of wall deposited on artificial defects. 73

**Figure 27** – Sample shapes used in numeric simulations. 78

**Figure 28** – Light collection geometry. 79

**Figure 29** - Laser head of the printer, with attached the collection optics. 82

**Figure 30** – Temperature field calculated during the simulation. 84

**Figure 31** – Simulation grid and effect ov vaporization on temperature. 85

**Figure 32** – Simulation of the three metrics with inner defects. 86

**Figure 33** - Dependence of the three metrics on angle of observation. 87

**Figure 34** - Simulation of the three metrics with protruding defects. 88

**Figure 35** - Simulation of the three metrics with combined defects. 90

**Figure 36** - Simulation of the three metrics with sequence of defects. 91

**Figure 37** – Low power laser on a modified surface similar to simulation. 93

**Figure 38** – High power laser on a modified surface similar to simulation. 94

# 10 List of tables

**Table 1** – Comparison of Nd and Yb as host in YAG active medium. 3

**Table 2** - Absorptivity of various materials for $CO_2$ and Nd:YAG lasers. 13

**Table 3** -Parameters involved in the DED deposition. 18

**Table 4** – Composition of base plate and feedstock powder. 44

**Table 5** - Printing parameters of choice for the presented experiment. 46

**Table 6** - Signal linked to an artificial defect introduced during a deposition. 64

**Table 7** - Dimensions of grooves (G) and holes (H) carved on sample. 65

**Table 8** – Three metrics in correspondance of artificial defects. 70

**Table 9** - Physical and thermal characteristics of iron. 83

**Table 10** - Laser and light collection parameters. 83

# 11 Acknowledgment

This thesis is the result of my employment in the public research Federal Institute for Materials Research and Testing BAM, in Berlin. Specifically, I worked within the frame of the internal project ProMoAM, a project focused on deepening our understanding of the metal additive manufacturing processes.

I would like to express my sincere gratitude to the research institution as a whole, a place where scientific research is conducted in an excellent way thanks to the relentless work of amazing scientists, students and technicians altogether.

# 12 References


1. R. K. Freeman, James A.; Lafyatis, Gregory P, *Electromagnetic radiation*. 2019: Oxford University Press.

2. H. Lee, et al., Lasers in additive manufacturing: A review. *International Journal of Precision Engineering and Manufacturing-Green Technology*, 2017. **4**(3): p. 307-322.^10.1007/s40684-017-0037-7

3. A. Kar, et al., Optothermal effects of laser modes in laser materials processing. *Optical and Quantum Electronics*, 1995. **27**(12): p. 1165-1180.^10.1007/BF00326473

4. J. O. Milewsky, *Additive Manufacturing of Metals*. Springer Series in Materials Science. 2017.

5. I. Gibson, et al., *Additive Manufacturing Technologies*. 2 ed. 2015: Springer, New York, NY.

6. S. S. Dimov, Rapid Manufacturing: The Technologies and Applications of Rapid Prototyping and Rapid Tooling. 2001: Springer London.

7. L. Pera, et al., The Role of the Laser in Rapid Prototyping. 1993.

8. D. F. O. Braga, et al., Advanced design for lightweight structures: Review and prospects. *Progress in Aerospace Sciences*, 2014. **69**: p. 29-39.^10.1016/j.paerosci.2014.03.003

9. https://www.nasa.gov/marshall/news/nasa-3-D-prints-first-full-scale-copper-rocket-engine-part.html.

10. C. W. J. Lim, et al., An Overview of 3-D Printing in Manufacturing, Aerospace, and Automotive Industries. *IEEE Potentials*, 2016. **35**(4): p. 18-22.^10.1109/mpot.2016.2540098

11. J. C. Vasco, Additive manufacturing for the automotive industry, in Additive Manufacturing. 2021. p. 505-530.

12. M. S. Korium, et al., Direct Metal Laser Sintering of Precious Metals for Jewelry Applications: Process Parameter Selection and Microstructure Analysis. *IEEE Access*, 2021. **9**: p. 126530-126540.^10.1109/ACCESS.2021.3112479

13. D. Svetlizky, et al., Directed energy deposition (DED) additive manufacturing: Physical characteristics, defects, challenges and applications. *Materials Today*, 2021. **49**: p. 271-295.^https://doi.org/10.1016/j.mattod.2021.03.020

14. Z.-j. Tang, et al., A review on in situ monitoring technology for directed energy deposition of metals. *The International Journal of Advanced Manufacturing Technology*, 2020. **108**(11-12): p. 3437-3463.^10.1007/s00170-020-05569-3

15. G. E. Totten, Handbook of Residual Stress and Deformation of Steel. 2002: ASM International.

16. T. DebRoy, et al., Additive manufacturing of metallic components – Process, structure and properties. *Progress in Materials Science*, 2018. **92**: p. 112-224.^10.1016/j.pmatsci.2017.10.001

17. M. Alimardani, et al., On the delamination and crack formation in a thin wall fabricated using laser solid freeform fabrication process: An experimental–numerical investigation. *Optics and Lasers in Engineering*, 2009. **47**(11): p. 1160-1168.^https://doi.org/10.1016/j.optlaseng.2009.06.010

18. N. Eliaz, et al., Comparative Quality Control of Titanium Alloy Ti–6Al–4V, 17–4 PH Stainless Steel, and Aluminum Alloy 4047 Either Manufactured or Repaired by Laser Engineered Net Shaping (LENS). *Materials*, 2020. **13**(18): p. 4171

19. C. Zhao, et al., Critical instability at moving keyhole tip generates porosity in laser melting. *Science*, 2020. **370**(6520): p. 1080-1086.^10.1126/science.abd1587

20. D. Herzog, et al., Additive manufacturing of metals. *Acta Materialia*, 2016. **117**: p. 371-392.^https://doi.org/10.1016/j.actamat.2016.07.019

21. M. N. Ahsan, et al., Microcomputed tomography analysis of intralayer porosity generation in laser direct metal deposition and its causes. *Journal of Laser Applications*, 2011. **23**(2): p. 022009.^10.2351/1.3582311

22. W. J. Sames, et al., The metallurgy and processing science of metal additive manufacturing. *International Materials Reviews*, 2016: p. Medium: ED; Size: 76 p.

23. F. Brückner, et al., *3 - Hybrid laser manufacturing*, in *Laser Additive Manufacturing*, M. Brandt, Editor. 2017, Woodhead Publishing. p. 79-97.

24. J. O. Milewski, *Additive Manufacturing of Metals*. Springer Series in Materials Science. 2017: Springer Cham.

25. S. J. Altenburg, et al., Towards the determination of real process temperatures in the LMD process by multispectral thermography. in Thermosense: Thermal Infrared Applications XLIII. 2021. SPIE

26. H. Ehlers, et al., Heterodyne Eddy Current Testing Using Magnetoresistive Sensors for Additive Manufacturing Purposes. *IEEE Sensors Journal*, 2020. **20**(11): p. 5793-5800.^10.1109/JSEN.2020.2973547

27. A. Einstein, Zur Quantentheorie der Strahlung. *Physikalische Zeitschrift*, 1917. **18**: p. 121

28. P. W. Milonni, et al., *Laser Physics*. 2010: Wiley.

29. H. Hügel, New solid-state lasers and their application potentials. *Optics and Lasers in Engineering*, 2000. **34**(4-6): p. 213-229.^10.1016/s0143-8166(00)00065-8

30. H. E. P. R.H. Pantell, *Fundamentals of Quantum Electronics*. 1964: Wiley.

31. P. Lacovara, et al., Room-temperature diode-pumped Yb:YAG laser. *Opt Lett*, 1991. **16**(14): p. 1089-91.^10.1364/ol.16.001089

32. M. Li, et al., High Power Continuous Wave Yb:YAG Composite Crystal Zigzag Slab Amplifier at Room Temperature. *IEEE Photonics Journal*, 2017. **9**(6): p. 1-9.^10.1109/jphot.2017.2768408

33. D. Brown, et al., *Innovative high-power CW Yb:YAG cryogenic laser*. Defense and Security Symposium. Vol. 6552. 2007: SPIE.

34. I. Tomashchuk, et al., Dissimilar laser welding of AISI 316L stainless steel to Ti6–Al4–6V alloy via pure vanadium interlayer. *Materials Science and Engineering: A*, 2015. **622**: p. 37-45.^10.1016/j.msea.2014.10.084

35. R. Indhu, et al., Yb: YAG laser welding of dual phase steel to aluminium alloy. *Journal of Materials Processing Technology*, 2018. **262**: p. 411-421.^10.1016/j.jmatprotec.2018.05.022

36. S. Guarino, et al., Laser milling of yttria-stabilized zirconia by using a Q-switched Yb:YAG fiber laser: experimental analysis. *The International Journal of Advanced Manufacturing Technology*, 2017. **94**(1-4): p. 1373-1385.^10.1007/s00170-017-1020-8

37. F. Caiazzo, et al., Mechanical properties of Inconel 718 in additive manufacturing via selective laser melting: An investigation on possible anisotropy of tensile strength. in 2017 IEEE 3rd International Forum on Research and Technologies for Society and Industry (RTSI). 2017.^10.1109/RTSI.2017.8065941

38. E. Uhlmann, et al., Effects on the distortion of Inconel 718 components along a hybrid laser-based additive manufacturing process chain using laser

powder bed fusion and laser metal deposition. *Progress in Additive Manufacturing*, 2021. **6**(3): p. 385-394.^10.1007/s40964-021-00171-9

39. N. Scheuschner, et al., Vergleich der Messungen der Schmelzbadtemperatur bei der Additiven Fertigung von Metallen mittels IR-Spektroskopie und Thermografie. *tm - Technisches Messen*, 2021. **88**(10): p. 626-632.^doi:10.1515/teme-2021-0056

40. L. Tonks, Oscillations in ionized gases, in Plasma and Oscillations. 1961, Elsevier. p. 122-139.

41. G. Chryssolouris, *Laser Machining Applications*, in *Laser Machining: Theory and Practice*. 1991, Springer New York: New York, NY. p. 209-274.

42. H. B. Cary, *Modern Welding Technology*. 1998: Prentice Hall.

43. ISO/ASTM, Additive manufacturing — General principles — Terminology. 2015. p. 19

44. C. W. Hull (1986). Apparatus for production of three-dimensional objects by stereolithography, USA 4,575,330.

45. J. P. Kruth, et al., Progress in Additive Manufacturing and Rapid Prototyping. *CIRP Annals*, 1998. **47**(2): p. 525-540.^10.1016/s0007-8506(07)63240-5

46. C. R. Deckard (1989). Method and apparatus for producing parts by selective sintering US4863538A.

47. A. T. Gaynor, et al., Topology Optimization for Additive Manufacturing: Considering Maximum Overhang Constraint, in 15th AIAA/ISSMO Multidisciplinary Analysis and Optimization Conference.

48. C. Y. Yap, et al., Review of selective laser melting: Materials and applications. *Applied Physics Reviews*, 2015. **2**(4): p. 041101.^10.1063/1.4935926

49. S. L. Sing, et al., Laser and electron-beam powder-bed additive manufacturing of metallic implants: A review on processes, materials and designs. *J Orthop Res*, 2016. **34**(3): p. 369-85.^10.1002/jor.23075

50. W. E. Frazier, Metal Additive Manufacturing: A Review. *Journal of Materials Engineering and Performance*, 2014. **23**(6): p. 1917-1928.^10.1007/s11665-014-0958-z

51. B. K. Foster, et al., A brief survey of sensing for metal-based powder bed fusion additive manufacturing. in Dimensional Optical Metrology and Inspection for Practical Applications IV. 2015. Bellingham, WA: SPIE.^10.1117/12.2180654

52. K. Urabe, et al., Flaw Inspection of Aluminum Pipes by Non-Contact Visualization of Circumferential Guided Waves using Laser Ultrasound Generation and an Air-Coupled Sensor. *Journal of Physics: Conference Series*, 2014. **520**: p. 012009.^10.1088/1742-6596/520/1/012009

53. NIST, Report on Measurement Science Roadmap for Metal Based Additive Manufacturing. 2013

54. L. E. Criales, et al., Sensitivity analysis of material and process parameters in finite element modeling of selective laser melting of Inconel 625. *The International Journal of Advanced Manufacturing Technology*, 2016. **86**(9): p. 2653-2666.^10.1007/s00170-015-8329-y

55. L. Koester, et al., Additive manufacturing metrology: State of the art and needs assessment. *AIP Conference Proceedings*, 2016. **1706**(1): p. 130001.^10.1063/1.4940604

56. X. Tan, et al., Graded microstructure and mechanical properties of additive manufactured Ti–6Al–4V via electron beam melting. *Acta Materialia*, 2015. **97**: p. 1-16.^https://doi.org/10.1016/j.actamat.2015.06.036

57. J. L. Koch, et al., *Rapid prototyping by laser cladding*. in *International Congress on Applications of Lasers & Electro-Optics*. 1993. Orlando, Florida, USA: Laser Institute of America.^10.2351/1.5058617

58. D.-G. Ahn, Correction to: Directed Energy Deposition (DED) Process: State of the Art. *International Journal of Precision Engineering and Manufacturing-Green Technology*, 2021.^10.1007/s40684-021-00401-z

59. R. Glardon, et al., Influence of Nd:YAG Parameters on the Selective Laser Sintering of Metallic Powders. *CIRP Annals*, 2001. **50**(1): p. 133-136.^https://doi.org/10.1016/S0007-8506(07)62088-5

60. S. M. Yusuf, et al., Influence of energy density on metallurgy and properties in metal additive manufacturing. *Materials Science and Technology*, 2017. **33**(11): p. 1269-1289.^10.1080/02670836.2017.1289444

61. J. W. Sears, The Effects of Processing Parameters on Microstructure and Properties of Laser Deposited PM Alloy 690N{sub 2} Powder. 2002: United States. p. Medium: ED; Size: 6250 Kilobytes pages.10.2172/821700

62. A. S. Wu, et al., An Experimental Investigation into Additive Manufacturing-Induced Residual Stresses in 316L Stainless Steel. *Metallurgical and Materials Transactions A*, 2014. **45**(13): p. 6260-6270.^10.1007/s11661-014-2549-x

63. D. Hann, et al., A simple methodology for predicting laser-weld properties from material and laser parameters. *Journal of Physics D: Applied Physics*, 2011. **44**(44): p. 445401

64. D. B. Hann, et al., *Keyholing or Conduction – Prediction of Laser Penetration Depth*. 2010. London: Springer London.^10.1007/978-1-84996-432-6_63

65. R. Rai, et al., Heat transfer and fluid flow during keyhole mode laser welding of tantalum, Ti–6Al–4V, 304L stainless steel and vanadium. *Journal of Physics D: Applied Physics*, 2007. **40**(18): p. 5753-5766.^10.1088/0022-3727/40/18/037

66. P. C. Collins, et al., Microstructural Control of Additively Manufactured Metallic Materials. *Annual Review of Materials Research*, 2016. **46**(1): p. 63-91.^10.1146/annurev-matsci-070115-031816

67. S. Clijsters, et al., A priori process parameter adjustment for SLM process optimization. in Innovative Developments in Virtual and Physical Prototyping - Proceedings of the 5th International Conference on Advanced Research and Rapid Prototyping. 2012. Leiria, Portugal: CRC Press

68. H. Kim, et al., Effects of Deposition Strategy and Preheating Temperature on Thermo-Mechanical Characteristics of Inconel 718 Super-Alloy Deposited on AISI 1045 Substrate Using a DED Process. *Materials (Basel)*, 2021. **14**(7).^10.3390/ma14071794

69. X. Lu, et al., Substrate design to minimize residual stresses in Directed Energy Deposition AM processes. *Materials & Design*, 2021. **202**.^10.1016/j.matdes.2021.109525

70. R. Wauthle, et al., Revival of pure titanium for dynamically loaded porous implants using additive manufacturing. *Materials Science and Engineering: C*, 2015. **54**: p. 94-100.^https://doi.org/10.1016/j.msec.2015.05.001

71. D. Gu, et al., Densification behavior, microstructure evolution, and wear performance of selective laser melting processed commercially pure titanium. *Acta Materialia*, 2012. **60**(9): p. 3849-3860.^10.1016/j.actamat.2012.04.006

72. K. Bartkowiak, et al., New Developments of Laser Processing Aluminium Alloys via Additive Manufacturing Technique. *Physics Procedia*, 2011. **12**: p. 393-401.^https://doi.org/10.1016/j.phpro.2011.03.050

73. D. Buchbinder, et al., High Power Selective Laser Melting (HP SLM) of Aluminum Parts. *Physics Procedia*, 2011. **12**: p. 271-278.^https://doi.org/10.1016/j.phpro.2011.03.035

74. E. Louvis, et al., Selective laser melting of aluminium components. *Journal of Materials Processing Technology*, 2011. **211**(2): p. 275-284.^https://doi.org/10.1016/j.jmatprotec.2010.09.019

75. A. Singh, et al., Laser Metal Deposition of Al-7050/Al50Mg50 Gradient Material. *Metallurgical and Materials Transactions A*, 2019. **50**(8): p. 3949-3958.^10.1007/s11661-019-05308-8

76. R. Santos-Ortiz, et al., Effect of deposition energy on the microstructure and phase purity of pulsed laser deposited iron fluoride thin films. *Applied Physics A*, 2015. **120**(3): p. 863-868.^10.1007/s00339-015-9334-6

77. G. P. Dinda, et al., Fabrication of Ti-6Al-4V Scaffolds by Direct Metal Deposition. *Metallurgical and Materials Transactions A*, 2008. **39**(12): p. 2914-2922.^10.1007/s11661-008-9634-y

78. P. Li, et al., On the Fatigue Performance of Additively Manufactured Ti-6Al-4V to Enable Rapid Qualification for Aerospace Applications. in 57th AIAA/ASCE/AHS/ASC Structures, Structural Dynamics, and Materials Conference. 2016. San Diego, California, USA: American Institute of Aeronautics and Astronautics Inc, AIAA.^10.2514/6.2016-1656

79. B. V. Krishna, et al., Low stiffness porous Ti structures for load-bearing implants. *Acta Biomater*, 2007. **3**(6): p. 997-1006.^10.1016/j.actbio.2007.03.008

80. Y. Liu, et al., Enhancement of entangled porous titanium by BisGMA for load-bearing biomedical applications. *Materials Science and Engineering: C*, 2016. **61**: p. 37-41.^https://doi.org/10.1016/j.msec.2015.12.018

81. A. D. DobrzaDska-Danikiewicz, et al., Ti 6 Al 4 V titanium alloy used as a modern biomimetic material. 2016.

82. R. Brånemark, et al., Bone response to laser-induced micro- and nano-size titanium surface features. *Nanomedicine: Nanotechnology, Biology and Medicine*, 2011. **7**(2): p. 220-227.^https://doi.org/10.1016/j.nano.2010.10.006

83. R. Banerjee, et al., A novel combinatorial approach to the development of beta titanium alloys for orthopaedic implants. *Materials Science and Engineering: C*, 2005. **25**(3): p. 282-289.^https://doi.org/10.1016/j.msec.2004.12.010

84. A. Jinoop, et al., Laser-assisted directed energy deposition of nickel super alloys: A review. *Proceedings of the Institution of Mechanical Engineers, Part L: Journal of Materials: Design and Applications*, 2019. **233**(11): p. 2376-2400.^10.1177/1464420719852658

85. L. Bond, et al., *NDE in-process for metal parts fabricated using powder based additive manufacturing*. SPIE Smart Structures + Nondestructive Evaluation. Vol. 10973. 2019: SPIE.

86. J. A. Slotwinski, et al., Characterization of Metal Powders Used for Additive Manufacturing. *Journal of research of the National Institute of Standards and Technology*, 2014. **119**: p. 460-493.^10.6028/jres.119.018

87. *Laser additive manufacturing : materials, design, technologies, and applications / edited by Milan Brandt*. Woodhead Publishing series in electronic and optical materials ; no. 88., ed. M. Brandt. 2017, Duxford ; Cambridge, MA ; Kidlington: Woodhead Publishing is an Imprint of Elsevier.

88. L. Yan, et al., Additive manufacturing of functionally graded metallic materials using laser metal deposition. *Additive Manufacturing*, 2020. **31**: p. 100901.^https://doi.org/10.1016/j.addma.2019.100901

89. M. Yu, et al., Microstructure and corrosion behaviour of 316 L-IN625 functionally graded materials via laser metal deposition. *Corrosion Science*, 2021. **193**: p. 109876.^https://doi.org/10.1016/j.corsci.2021.109876

90. B. Dutton, et al., Metal Additive Manufacturing Defect Formation and Nondestructive Evaluation Detectability, in Structural Integrity of Additive Manufactured Parts. 2020. p. 1-50.

91. M. Rombouts, et al., Fundamentals of Selective Laser Melting of alloyed steel powders. *CIRP Annals*, 2006. **55**(1): p. 187-192.^https://doi.org/10.1016/S0007-8506(07)60395-3

92. G. K. L. Ng, et al., Porosity formation and gas bubble retention in laser metal deposition. *Applied Physics A*, 2009. **97**(3): p. 641.^10.1007/s00339-009-5266-3

93. H. Gong, et al., Analysis of defect generation in Ti–6Al–4V parts made using powder bed fusion additive manufacturing processes. *Additive Manufacturing*, 2014. **1-4**: p. 87-98.^https://doi.org/10.1016/j.addma.2014.08.002

94. C. Teng, et al., A review of defect modeling in laser material processing. *Additive Manufacturing*, 2017. **14**: p. 137-147.^10.1016/j.addma.2016.10.009

95. A. Saboori, et al., Microstructure and Mechanical Properties of AISI 316L Produced by Directed Energy Deposition-Based Additive Manufacturing: A Review. *Applied Sciences*, 2020. 10(9): p. 3310

96. S. Barua, et al., Vision-based defect detection in laser metal deposition process. *Rapid Prototyping Journal*, 2014. 20(1): p. 77-85.^10.1108/RPJ-04-2012-0036

97. M. N. Ahsan, et al., Microcomputed tomography analysis of intralayer porosity generation in laser direct metal deposition and its causes. *Journal of Laser Applications*, 2011. 23(2).^10.2351/1.3582311

98. A. Bauereiß, et al., Defect generation and propagation mechanism during additive manufacturing by selective beam melting. *Journal of Materials Processing Technology*, 2014. 214(11): p. 2522-2528.^https://doi.org/10.1016/j.jmatprotec.2014.05.002

99. H. Meier, et al., Experimental studies on selective laser melting of metallic parts. *Materialwissenschaft und Werkstofftechnik*, 2008. 39(9): p. 665-670.^10.1002/mawe.200800327

100. H. Attar, et al., Comparative study of commercially pure titanium produced by laser engineered net shaping, selective laser melting and casting processes. *Materials Science and Engineering: A*, 2017. 705: p. 385-393

101. M. Liu, et al., A Review of the Anomalies in Directed Energy Deposition (DED) Processes & Potential Solutions - Part Quality & Defects. *Procedia Manufacturing*, 2021. 53: p. 507-518.^https://doi.org/10.1016/j.promfg.2021.06.093

102. C. Zhong, et al., Experimental study of effects of main process parameters on porosity, track geometry, deposition rate, and powder efficiency for high deposition rate laser metal deposition. *Journal of Laser Applications*, 2015. 27(4): p. 042003.^10.2351/1.4923335

103. M. Marya, et al., Microstructural development and technical challenges in laser additive manufacturing: case study with a 316L industrial part. *Metallurgical and Materials Transactions B*, 2015. 46(4): p. 1654-1665

104. C. C. Murgau, Microstructure model for Ti-6Al-4V used in simulation of additive manufacturing, PhD thesis in Department of Engineering Sciences and Mathematics 2016, Luleå tekniska universitet

105. N. Shamsaei, et al., An overview of Direct Laser Deposition for additive manufacturing; Part II: Mechanical behavior, process parameter optimization and

control. *Additive Manufacturing*, 2015. **8**: p. 12-35.^10.1016/j.addma.2015.07.002

106. Y. Zhu, et al., The anisotropy of laser melting deposition additive manufacturing Ti–6.5Al–3.5Mo–1.5Zr–0.3Si titanium alloy. *Materials & Design*, 2015. **67**: p. 538-542.^https://doi.org/10.1016/j.matdes.2014.11.001

107. B. E. Carroll, et al., Anisotropic tensile behavior of Ti–6Al–4V components fabricated with directed energy deposition additive manufacturing. *Acta Materialia*, 2015. **87**: p. 309-320.^https://doi.org/10.1016/j.actamat.2014.12.054

108. I. Shishkovsky, et al., Metal matrix composites with ternary intermetallic inclusions fabricated by laser direct energy deposition. *Composite Structures*, 2018. **183**: p. 663-670.^https://doi.org/10.1016/j.compstruct.2017.09.004

109. R. Banerjee, et al., Nanoscale TiB precipitates in laser deposited Ti-matrix composites. *Scripta Materialia*, 2005. **53**(12): p. 1433-1437.^https://doi.org/10.1016/j.scriptamat.2005.08.014

110. A. Wilby, et al., Defects introduced into Metals during Fabrication and Service. *Materials science and engineering*, 2009. **3**: p. 48-75

111. G. Moroni, et al., Towards Early Estimation of Part Accuracy in Additive Manufacturing. *Procedia CIRP*, 2014. **21**: p. 300-305.^https://doi.org/10.1016/j.procir.2014.03.194

112. Y. S. Lee, et al., Surface tension-powered build dimension control in laser additive manufacturing process. *The International Journal of Advanced Manufacturing Technology*, 2015. **85**(5-8): p. 1035-1044.^10.1007/s00170-015-7974-5

113. Y. F. Shen, et al., Balling Process in Selective Laser Sintering 316 Stainless Steel Powder. *Key Engineering Materials*, 2006. **315-316**: p. 357-360.^10.4028/www.scientific.net/KEM.315-316.357

114. P. Peyre, et al., Simplified numerical model for the laser metal deposition additive manufacturing process. *Journal of Laser Applications*, 2017. **29**(2): p. 022304.^10.2351/1.4983251

115. P. Farahmand, et al., An experimental–numerical investigation of heat distribution and stress field in single- and multi-track laser cladding by a high-power direct diode laser. *Optics & Laser Technology*, 2014. **63**: p. 154-168.^https://doi.org/10.1016/j.optlastec.2014.04.016

116. L. Tang, et al., Melt Pool Temperature Control for Laser Metal Deposition Processes—Part II: Layer-to-Layer Temperature Control. *Journal of Manufacturing Science and Engineering*, 2010. 132(1).^10.1115/1.4000883

117. X. Lu, et al., In situ measurements and thermo-mechanical simulation of Ti–6Al–4V laser solid forming processes. *International Journal of Mechanical Sciences*, 2019. 153-154: p. 119-130.^https://doi.org/10.1016/j.ijmecsci.2019.01.043

118. L. W. Koester, et al., In-situ acoustic signature monitoring in additive manufacturing processes. *AIP Conference Proceedings*, 2018. 1949(1): p. 020006.^10.1063/1.5031503

119. H. Gaja, et al., Defects monitoring of laser metal deposition using acoustic emission sensor. *The International Journal of Advanced Manufacturing Technology*, 2017. 90(1-4): p. 561-574

120. J. Whiting, et al., Real-time acoustic emission monitoring of powder mass flow rate for directed energy deposition. *Additive Manufacturing*, 2018. 23: p. 312-318.^https://doi.org/10.1016/j.addma.2018.08.015

121. S. J. Wolff, et al., In-situ high-speed X-ray imaging of piezo-driven directed energy deposition additive manufacturing. *Scientific Reports*, 2019. 9(1): p. 962.^10.1038/s41598-018-36678-5

122. Y. Ding, et al., Development of sensing and control system for robotized laser-based direct metal addition system. *Additive Manufacturing*, 2016. 10: p. 24-35.^https://doi.org/10.1016/j.addma.2016.01.002

123. D. Hu, et al., Sensing, modeling and control for laser-based additive manufacturing. *International Journal of Machine Tools and Manufacture*, 2003. 43(1): p. 51-60.^https://doi.org/10.1016/S0890-6955(02)00163-3

124. S. Berumen, et al., Quality control of laser- and powder bed-based Additive Manufacturing (AM) technologies. *Physics Procedia*, 2010. 5: p. 617-622.^https://doi.org/10.1016/j.phpro.2010.08.089

125. M. Miyagi, et al., Adaptive shape control of laser-deposited metal structures by adjusting weld pool size. *Journal of Laser Applications*, 2014. 26(3): p. 032003.^10.2351/1.4869499

126. U. Thombansen, et al., Illumination for Process Observation in Laser Material Processing. *Physics Procedia*, 2014. 56: p. 1286-1296.^https://doi.org/10.1016/j.phpro.2014.08.053

127. S. Barua, et al., Development of low-cost imaging system for laser metal deposition processes. *Rapid Prototyping Journal*, 2011. **17**(3): p. 203-210.^10.1108/13552541111124789

128. M. Akbari, et al., An investigation on mechanical and microstructural properties of 316LSi parts fabricated by a robotized laser/wire direct metal deposition system. *Additive Manufacturing*, 2018. **23**: p. 487-497.^https://doi.org/10.1016/j.addma.2018.08.031

129. G. Bi, et al., Identification and qualification of temperature signal for monitoring and control in laser cladding. *Optics and Lasers in Engineering*, 2006. **44**(12): p. 1348-1359.^https://doi.org/10.1016/j.optlaseng.2006.01.009

130. J. B. Lei, et al., Design of Forming Shape Measurement System for Laser Molten Pool in Laser Fabricating. *Applied Mechanics and Materials*, 2010. **37-38**: p. 327-330.^10.4028/www.scientific.net/AMM.37-38.327

131. S. Moralejo, et al., A feedforward controller for tuning laser cladding melt pool geometry in real time. *The International Journal of Advanced Manufacturing Technology*, 2017. **89**(1): p. 821-831.^10.1007/s00170-016-9138-7

132. L. Song, et al., Phase congruency melt pool edge extraction for laser additive manufacturing. *Journal of Materials Processing Technology*, 2017. **250**: p. 261-269.^https://doi.org/10.1016/j.jmatprotec.2017.07.013

133. D. Qilin, et al., Measurement of the Molten Pool Image during Laser Cladding Process. in Proceedings of the 2014 International Conference on Mechatronics, Electronic, Industrial and Control Engineering. 2014. Atlantis Press.^https://doi.org/10.2991/meic-14.2014.141

134. K. Lei, et al., Analysis and modeling of melt pool morphology for high power diode laser cladding with a rectangle beam spot. *Optics and Lasers in Engineering*, 2018. **110**: p. 89-99.^https://doi.org/10.1016/j.optlaseng.2018.05.022

135. M. Lison, et al., Hyperspectral and thermal temperature estimation during laser cladding. *Journal of Laser Applications*, 2019. **31**(2): p. 022313.^10.2351/1.5096129

136. S. Liu, et al., Optical monitoring of high power direct diode laser cladding. *Optics & Laser Technology*, 2014. **64**: p. 363-376.^https://doi.org/10.1016/j.optlastec.2014.06.002

137. M. Doubenskaia, et al., Definition of brightness temperature and restoration of true temperature in laser cladding using infrared camera. *Surface*

*and Coatings Technology*, 2013. **220**: p. 244-247.^https://doi.org/10.1016/j.surfcoat.2012.10.044

138. P. Farahmand, et al., Laser cladding assisted with an induction heater (LCAIH) of Ni–60%WC coating. *Journal of Materials Processing Technology*, 2015. **222**: p. 244-258.^https://doi.org/10.1016/j.jmatprotec.2015.02.026

139. A. Mozaffari, et al., Optimal design of laser solid freeform fabrication system and real-time prediction of melt pool geometry using intelligent evolutionary algorithms. *Applied Soft Computing*, 2013. **13**(3): p. 1505-1519.^https://doi.org/10.1016/j.asoc.2012.05.031

140. A. Fathi, et al., Geometry Control of the Deposited Layer in a Nonplanar Laser Cladding Process Using a Variable Structure Controller. *Journal of Manufacturing Science and Engineering*, 2008. **130**(3).^10.1115/1.2823085

141. R. Liu, et al., Stereo vision-based repair of metallic components. *Rapid Prototyping Journal*, 2017. **23**(1): p. 65-73.^10.1108/RPJ-09-2015-0118

142. Z. Wang, et al., Stereo vision based hybrid manufacturing process for precision metal parts. *Precision Engineering*, 2015. **42**: p. 1-5.^https://doi.org/10.1016/j.precisioneng.2014.11.012

143. Y.-M. Kwak, et al., Geometry Regulation of Material Deposition in Near-Net Shape Manufacturing by Thermally Scanned Welding. *Journal of Manufacturing Processes*, 2002. **4**(1): p. 28-41.^https://doi.org/10.1016/S1526-6125(02)70131-X

144. L. Song, et al., Control of melt pool temperature and deposition height during direct metal deposition process. *The International Journal of Advanced Manufacturing Technology*, 2011. **58**(1-4): p. 247-256.^10.1007/s00170-011-3395-2

145. M. Iravani-Tabrizipour, et al., An image-based feature tracking algorithm for real-time measurement of clad height. *Machine Vision and Applications*, 2007. **18**(6): p. 343-354.^10.1007/s00138-006-0066-7

146. Y. S. Wang, et al., Study on Measurement of Melting Process of Molten Pool Formed by Laser Scanning Mirror. *Key Engineering Materials*, 2009. **392-394**: p. 141-145.^10.4028/www.scientific.net/KEM.392-394.141

147. I. Smurov, et al., Comprehensive analysis of laser cladding by means of optical diagnostics and numerical simulation. *Surface and Coatings Technology*, 2013. **220**: p. 112-121.^https://doi.org/10.1016/j.surfcoat.2012.10.053

148. M. L. Griffith, et al., Understanding thermal behavior in the LENS process. *Materials & Design*, 1999. **20**(2): p. 107-113.^https://doi.org/10.1016/S0261-3069(99)00016-3

149. Z. Liu, et al., Effects of deposition variables on molten pool temperature during laser engineered net shaping of Inconel 718 superalloy. *The International Journal of Advanced Manufacturing Technology*, 2019. **102**(1): p. 969-976.^10.1007/s00170-018-03245-1

150. M. Gharbi, et al., Influence of a pulsed laser regime on surface finish induced by the direct metal deposition process on a Ti64 alloy. *Journal of Materials Processing Technology*, 2014. **214**(2): p. 485-495.^https://doi.org/10.1016/j.jmatprotec.2013.10.004

151. M. Muller, et al., Temperature measurement of laser heated metals in highly oxidizing environment using 2D single-band and spectral pyrometry. *Journal of Laser Applications*, 2012. **24**(2): p. 022006.^10.2351/1.3701400

152. D. D. Baere, et al., Spectroscopic monitoring and melt pool temperature estimation during the laser metal deposition process. *Journal of Laser Applications*, 2016. **28**(2): p. 022303.^10.2351/1.4943995

153. C. B. Stutzman, et al., Multi-sensor investigations of optical emissions and their relations to directed energy deposition processes and quality. *Additive Manufacturing*, 2018. **21**: p. 333-339.^https://doi.org/10.1016/j.addma.2018.03.017

154. T. Sibillano, et al., Correlation spectroscopy as a tool for detecting losses of ligand elements in laser welding of aluminium alloys. *Optics and Lasers in Engineering*, 2006. **44**(12): p. 1324-1335.^https://doi.org/10.1016/j.optlaseng.2005.12.002

155. J. J. Valdiande, et al., Laser Metal Deposition On-Line Monitoring via Plasma Emission Spectroscopy and Spectral Correlation Techniques. *IEEE Journal of Selected Topics in Quantum Electronics*, 2021. **27**(6): p. 1-8.^10.1109/JSTQE.2021.3075489

156. B. J. Simonds, et al., Laser-induced fluorescence applied to laser welding of austenitic stainless steel for dilute alloying element detection. *Journal of Physics D: Applied Physics*, 2017. **50**(32): p. 325602.^10.1088/1361-6463/aa7836

157. B. J. Simonds, et al., In situ monitoring of Cu/Al laser welding using Laser Induced Fluorescence. *Procedia CIRP*, 2020. **94**: p. 605-609.^https://doi.org/10.1016/j.procir.2020.09.088

158. C. Zhao, et al., Real-time monitoring of laser powder bed fusion process using high-speed X-ray imaging and diffraction. *Scientific Reports*, 2017. **7**(1): p. 3602.^10.1038/s41598-017-03761-2

159. S. J. Wolff, et al., In situ X-ray imaging of pore formation mechanisms and dynamics in laser powder-blown directed energy deposition additive manufacturing. *International Journal of Machine Tools and Manufacture*, 2021. **166**: p. 103743.^https://doi.org/10.1016/j.ijmachtools.2021.103743

160. S. J. Wolff, et al., In-situ Observations of Directed Energy Deposition Additive Manufacturing Using High-Speed X-ray Imaging. *JOM*, 2021. **73**(1): p. 189-200.^10.1007/s11837-020-04469-x

161. V. N. Lednev, et al., In situ multi-elemental analysis by laser induced breakdown spectroscopy in additive manufacturing. *Additive Manufacturing*, 2019. **25**: p. 64-70.^https://doi.org/10.1016/j.addma.2018.10.043

162. P. A. Sdvizhenskii, et al., Online laser-induced breakdown spectroscopy for metal-particle powder flow analysis during additive manufacturing. *Journal of Analytical Atomic Spectrometry*, 2020. **35**(2): p. 246-253.^10.1039/C9JA00343F

163. V. N. Lednev, et al., Online and in situ laser-induced breakdown spectroscopy for laser welding monitoring. *Spectrochimica Acta Part B: Atomic Spectroscopy*, 2021. **175**.^10.1016/j.sab.2020.106032

164. M. Bayat, et al., A review of multi-scale and multi-physics simulations of metal additive manufacturing processes with focus on modeling strategies. *Additive Manufacturing*, 2021. **47**: p. 102278.^https://doi.org/10.1016/j.addma.2021.102278

165. Y. Li, et al., Thermal behavior during selective laser melting of commercially pure titanium powder: Numerical simulation and experimental study. *Additive Manufacturing*, 2014. **1-4**: p. 99-109.^https://doi.org/10.1016/j.addma.2014.09.001

166. A. M. Kamara, et al., Modelling of the Melt Pool Geometry in the Laser Deposition of Nickel Alloys Using the Anisotropic Enhanced Thermal Conductivity Approach. *Proceedings of the Institution of Mechanical Engineers, Part B: Journal of Engineering Manufacture*, 2011. **225**(1): p. 87-99.^10.1177/09544054jem2129

167. S. Bontha, et al., Effects of process variables and size-scale on solidification microstructure in beam-based fabrication of bulky 3D structures. *Materials Science and Engineering: A*, 2009. **513-514**: p. 311-318.^https://doi.org/10.1016/j.msea.2009.02.019

168. A. Plotkowski, et al., Verification and validation of a rapid heat transfer calculation methodology for transient melt pool solidification conditions in powder bed metal additive manufacturing. *Additive Manufacturing*, 2017. **18**: p. 256-268.^https://doi.org/10.1016/j.addma.2017.10.017

169. A. Hussein, et al., Finite element simulation of the temperature and stress fields in single layers built without-support in selective laser melting. *Materials & Design (1980-2015)*, 2013. **52**: p. 638-647.^https://doi.org/10.1016/j.matdes.2013.05.070

170. U. Fantz, Basics of plasma spectroscopy. *Plasma Sources Science and Technology*, 2006. **15**(4): p. S137-S147.^10.1088/0963-0252/15/4/s01

171. N. Scheuschner, et al., In-situ thermographic monitoring of the laser metal deposition process. in Sim-AM 2019: II International Conference on Simulation for Additive Manufacturing. 2019. CIMNE

172. S. Clijsters, et al., In situ quality control of the selective laser melting process using a high-speed, real-time melt pool monitoring system. *The International Journal of Advanced Manufacturing Technology*, 2014. **75**(5-8): p. 1089-1101.^10.1007/s00170-014-6214-8

173. J. R. Taylor, An Introduction to Error Analysis: The Study of Uncertainties in Physical Measurements. 1997: University Science Books.

174. I. B. Gornushkin, et al., Optical detection of defects during laser metal deposition: Simulations and experiment. *Applied Surface Science*, 2021. **570**.^10.1016/j.apsusc.2021.151214

175. S. Bilbao, et al., Directional source modeling in wave-based room acoustics simulation. in 2017 IEEE Workshop on Applications of Signal Processing to Audio and Acoustics (WASPAA). 2017.^10.1109/WASPAA.2017.8170007

176. M. Muhieddine, et al., Various Approaches for Solving Problems in Heat Conduction with Phase Change. *International Journal on Finite Volumes*, 2009: p. 19

177. Y. Khattari, et al., Apparent heat capacity method to investigate heat transfer in a composite phase change material. *Journal of Energy Storage*, 2020. **28**: p. 101239.^https://doi.org/10.1016/j.est.2020.101239

178. M. Yao, et al., An alternative formulation of the apparent heat capacity method for phase-change problems. *Numerical Heat Transfer, Part B: Fundamentals*, 1993. **24**(3): p. 279-300.^10.1080/10407799308955894

179. A. Peterlongo, et al., Laser-pulse sputtering of aluminum: Vaporization, boiling, superheating, and gas-dynamic effects. *Physical Review E*, 1994. 50(6): p. 4716-4727.^10.1103/PhysRevE.50.4716

180. R. Kelly, et al., Comments on explosive mechanisms of laser sputtering. *Applied Surface Science*, 1996. 96-98: p. 205-215.^https://doi.org/10.1016/0169-4332(95)00481-5

181. G. M. Pound, Selected Values of Evaporation and Condensation Coefficients for Simple Substances. *Journal of Physical and Chemical Reference Data*, 1972. 1(1): p. 135-146.^10.1063/1.3253096

182. A. V. Gusarov, et al., Thermal model of nanosecond pulsed laser ablation: Analysis of energy and mass transfer. *Journal of Applied Physics*, 2005. 97(1): p. 014307.^10.1063/1.1827321